Scattering, Adsorption, and Langmuir-Hinshelwood Desorption Models for Physisorptive and Chemisorptive Gas-Surface Systems

DISSERTATION

Brook I. Bentley, Captain, USAF

AFIT-ENY-DS-13-S-01

DEPARTMENT OF THE AIR FORCE
AIR UNIVERSITY

AIR FORCE INSTITUTE OF TECHNOLOGY

Wright-Patterson Air Force Base, Ohio

AFIT-ENY-DS-13-S-01

Scattering, Adsorption, and Langmuir-Hinshelwood Desorption Models for Physisorptive and Chemisorptive Gas-Surface Systems

DISSERTATION

Presented to the Faculty
Graduate School of Engineering and Management
Air Force Institute of Technology
Air University
Air Education and Training Command
in Partial Fulfillment of the Requirements for the
Degree of Doctor of Philosophy

Brook I. Bentley, BS, MS
Captain, USAF

September 2013

AFIT-ENY-DS-13-S-01

Scattering, Adsorption, and Langmuir-Hinshelwood Desorption Models for Physisorptive and Chemisorptive Gas-Surface Systems

Brook I. Bentley, BS, MS
Captain, USAF

Approved:

//signed//	August 7, 2013
Robert B. Greendyke, PhD (Chairman)	Date
//signed//	August 7, 2013
William F. Bailey, PhD (Member)	Date
//signed//	July 22, 2013
Nathaniel P. Lockwood, PhD (Member)	Date
//signed//	July 22, 2013
Captain Christopher L. Martin, PhD (Member)	Date

Accepted:

//signed//	August 26, 2013
Heidi R. Ries Interim Dean, Graduate School of Engineering and Management	Date

Abstract

Surface effects limit the performance of hypersonic vehicles, micro-electro-mechanical devices, and directed energy systems. This research develops methods to predict adsorption, scattering, and thermal desorption of molecules on a surface. These methods apply to physisorptive (adsorption and scattering) and chemisorptive (thermal desorption) gas-surface systems. Engineering and design applications will benefit from these methods, hence they are developed under the Direct Simulation Monte Carlo construct.

The novel adsorption and scattering contribution, the Modified Kisliuk with Scattering method, predicts angular and energy distributions, and adsorption probabilities. These results agree more closely with experiment than the state-of-the-art Cercignani-Lampis-Lord scattering kernel. Super-elastic scattering is predicted. Gas-adlayer interactions are included for the first time. Accommodation coefficents can be determined by fitting simulations to experimental data.

The new thermal desorption model accurately calculates angular, translational, rotational, and vibrational distributions, and the rotational alignment parameter. The model is validated by comparing with experiments. Multiple transition states are considered in a set of non-dimensionalized equations of motion, linked with temporally-accurate event timing. Initial conditions are chosen from a new truncated Maxwell-Boltzmann distribution. Run times are improved by eliminating the Gaussian Weighting of desorbing products. The absorption energy barrier is shown to significantly contribute only to the translational energy of desorbing molecules by contributing energy to each adatom in a similar manner.

To my wife,

my partner and equal in all things.

To my daughters,

who brighten my life with their

innocence and purity.

Acknowledgements

I am thankful for the kind and helpful mentoring of my research advisor, Dr. Robert Greendyke. He has provided for me an example of scholarship and professionalism that I want to emulate in my future pursuits. I am also grateful for the generous financial support of Dr. Nathaniel Lockwood from the Air Force Research Laboratory, without whom my research would not have been possible. In addition, I appreciate the time that Dr. William Bailey and Capt Christopher Martin have devoted to my research, as well as their advice on how to proceed.

Brook I. Bentley

Table of Contents

Page

List of Figures

Scattering, Adsorption, and Langmuir-Hinshelwood Desorption Models for Physisorptive and Chemisorptive Gas-Surface Systems

I. Introduction

Pulse shortening, a negative effect which limits the energy output of High-Power Microwave (HPM)[1] devices, has been identified as the most important problem in the HPM field [16]. Pulse shortening occurs when the pulse generated by the HPM device is shorter than the design allows, effectively limiting the amount of energy that can be produced at the same power level. The main contributors to pulse shortening are plasma effects, one of which is gap closure. Gap closure is the process by which the surface plasma migrates into the cavity, thereby changing the diode impedance. This change in turn reduces wave coupling in the Slow Wave Structure (SWS), a critical step in creating microwaves. The plasma created at the anode surface is a result of gas desorption [both thermal desorption and Electron-Stimulated Desorption (ESD)], field emission, and Secondary Electron Emission (SEE). Being able to predict, minimize, or prevent gas desorption altogether thus becomes an important aspect in advancing the state-of-the-art in HPM technology.

Gas desorption is also an important process in other fields where surface effects dominate, such as catalysis, thin-film processing, space environments, and hypersonics. Unfortunately, desorption is complex and difficult to study experimentally, theoretically, and computationally. The many-body problem of desorption has no

[1]For a full listing of all the acronyms used in this document, please refer to Appendix B.

straightforward analytical solution. Experimentalists continue to seek methods of measuring surface kinetics (e.g. orientations, internal and kinetic energies, and electronic states). Even quantum-based calculations, such as Density Functional Theory (DFT), must truncate the number of molecular interactions to achieve reasonable results.[2]

Researchers at the Air Force Research Laboratory (AFRL) develop state-of-the-art HPM systems and technologies through experimentation and simulation. A successful tool, the Improved Concurrent Electromagnetic Particle-In-Cell (ICEPIC) code, allows researchers to both understand more explicitly what is occurring within the entire system, and quickly assess new HPM system-level designs, saving valuable resources.

In order to properly simulate the performance of an HPM system, it is important to model the phenomena occuring within the magnetron. For HPM systems, EM waves are generated by a source, guided by a waveguide, and then broadcast (or directed) with an antenna. A magnetron is a typical microwave source. Microwaves are generated in a magnetron from the interaction of moving electrons with both an applied magnetic field and side cavities.

AFRL is seeking to employ Direct Simulation Monte Carlo (DSMC) techniques in ICEPIC to model both gas-surface effects and gas-gas collisions, including pulse shortening due to surface contaminants. DSMC is a popular engineering method that approximates the solution to the Boltzmann equation. The Boltzmann equation describes the position and velocity probability distributions of gas molecules in both space and time. Typically, the Boltzmann equation is applied to flows with low densities to keep computational costs low. Thus, DSMC is useful in the fields of hypersonics, Micro-Electro-Mechanical Systems (MEMS), and vacuum devices (e.g. mag-

[2]Please note that here and in the remainder of this paper the term molecule refers to an atom or to a molecule.

netrons), to name a few. DSMC approximates the solution to the Boltzmann equation by simulating molecule-molecule interactions on a coarse level. A number of simulated molecules are followed as they interact, and through well-established DSMC techniques, excellent solutions can be obtained. These collisions are between *simulated* molecules, each of which represent many *real* molecules. Since system-level simulations are performed by ICEPIC, an engineering method such as DSMC is required simply due to limited resources. It is currently not possible to calculate the dynamics of each molecule for a large system using, for example, Molecular Dynamics (MD). The length scales in MD studies involve only hundreds of molecules. On the other hand, the number of molecules on the anode surface of a magnetron are on the order of 10^{15} per square centimeter. Obviously, MD simulations would not be able to sustain such a large number of molecules. Hence a statistical method (DSMC) is sought which makes such simulations tractable.

In addition, DSMC techniques are being considered by AFRL for HPM simulations due to differences in time scales during magnetron operation [156]. For example, it is reasonable for a magnetron to have a 500-ns pulse width with 0.1 s between pulses. The duty cycle is calculated as the ratio of the pulse width to the period. In this example, the duty cycle is 0.0005%. In other words, only 0.0005% of the dwell time is occupied with a pulse. During the pulse width, high-energy electrons are explosively emitted from the plasma created on the cathode surface. Accurate PIC methods are employed at the pulse time scale to adequately resolve particle positions and velocities, as well as the dynamic electromagnetic (EM) field, while low-energy neutrals can be assumed to be stationary. The total EM field is comprised of an applied portion from a permanent magnet, and a dynamic portion created by the motion of the electrons. Once high-velocity particles have transferred their energy and only lower-velocity particles remain in the cavity (i.e. between pulses), the EM

field may be considered static, and DSMC techniques would then be available to describe particle interactions on a larger time scale. This research directly supports their efforts by providing thermal desorption and adsorption models for the anode surface in a DSMC framework.

Adsorption is the process by which a foreign molecule is bound to a surface. Absorption, on the other hand, is the process by which a foreign molecule is bound within the bulk. Desorption is the inverse process of adsorption. Therefore, desorption is the process by which the bond between a foreign molecule and the surface is broken.

Some of the most elementary surface processes in important plasma systems employed in basic research and in modern material science are (dissociative) adsorption and (recombinative) desorption [27]. Modeling these processes efficiently will allow for more accurate predictions of system performance as well as improved system designs [7].

Unfortunately, thermal desorption (and adsorption) dynamics are difficult to model. The description, interpretation, and prediction of state and energy distributions of desorbing molecules currently represent a major challenge in theoretical chemistry [139]. It should come as no surprise that the understanding of surface phenomena is still far from that of gas-phase reactions [107], since a gas-phase reaction involves only a small number of molecules when compared with even the simplest of gas-surface systems.

To complicate matters further, there are multiple desorption pathways available, of which the following are a brief sampling. There is the Langmuir-Hinshelwood (LH) reaction, characterized by two adsorbed atoms combining into a molecule on the surface that is then immediately desorbed [60; 146; 168], and the Eley-Rideal (ER) mechanism, wherein an adatom and a gas-phase atom combine into a molecule that is desorbed immediately [28; 71; 133; 137]. In the presence of strong EM fields,

field-induced desorption (FID) may cause adsorbed molecules to desorb. The bulk material itself may contribute through phonon-induced desorption, in which surface vibrations sufficiently excite adatoms to desorb [15]. In addition, collisions from ions, photons, and electrons are known to cause desorption, through ion-induced desorption (IID) [21], photo-induced desorption (PID) [63], and ESD[3] [4; 6; 41; 69; 70; 113; 121; 140], respectively.

Some of these desorption pathways are present in a typical magnetron system. In the magnetron cavity, a plasma forms out of electrons, ions, and neutral molecules. Those electrons impact the anode surface after being emitted from the cathode and travelling through the annulus. Such impacts cause either ESD, or localized surface heating which in turn induces thermal desorption (LH). When the ions collide with the anode surface, they either scatter or induce the desorption of electrons, ions, or molecules (IID). Surface coverage may repopulate through adsorption from ionic and molecular impacts, as well as from permeation and diffusion of atoms through the bulk. All of these effects combine to create a complex andproblem which is currently unresolved. Questions remain about the relative contributions of each of these effects, questions which can only be answered with experimental and theoretical contributions. Such work will allow for these effects to be understood and decoupled.

Unfortunately, all of the relevant surface effects cannot be addressed in this research. Therefore, their relative contributions must be prioritized. The two most important desorption mechanisms are thought to be caused by the high number of electron impacts [59]. They are (1) thermal desorption via the LH mechanism, indirectly caused by localized surface heating from electron impacts, and (2) ESD. The next contributor to desorption is expected to be thermal desorption via the ER mechanism, indirectly caused by localized surface heating from electron impacts, and

[3]ESD is sometimes referred to as Desorption Induced by Electronic Transitions (DIET).

directly caused by ionic/molecular impacts. Finally, adsorption is thought to occur from ionic and molecular surface impacts.

The phenomena of desorption and adsorption are strongly influenced by the type of chemical bond that exists between the adsorbate/gas and the surface. There are two classifications available in the literature, physical sorption (*physisorption*) and chemical sorption (*chemisorption*) [62:178]. Physisorption is characterized by a weak bond dominated by van der Waals forces, usually on the order of 0.01 to 0.1 eV, and does not involve an activation barrier. On the other hand, chemisorption is characterized by a much stronger bond, typically in the range of 0.1 to 10 eV, with the inclusion of an activation barrier. Chemisorption is the result of either hydrogen bonding, covalent chemical bonding, or metallic bonding.

In order to study thermal desorption via the LH pathway, one of the most important surface effects in HPM magnetrons, both physisorptive and chemisorptive systems will be investigated. First, the inverse process of desorption (adsorption) will be considered for a physisorption system in Chapter II. This system will be as simple as possible, where the adsorbate is xenon, a noble gas, and the surface is platinum. The Xe-Pt gas-surface system is a typical starting point for physisorption modeling, and will provide insight into how to model surface effects in a DSMC framework. Then in Chapter III, the complex process of thermal desorption (LH) will be studied on the simplest chemisorption gas-surface system available, H_2-Cu [126]. Fortunately, H_2-Cu is also the most thoroughly studied example of activated adsorption [114]. The study of H_2-Cu desorption will provide both simulation results directly applicable to current HPM research, and a new methodology from which desorption can be modeled for *any* gas-surface system in the future.

1.1 Physisorption

Physisorption is investigated (adsorption and scattering) in Chapter II for a model system, Xe-Pt(111). This gas-surface combination is typically employed by researchers when developing physisorption models. Xenon is a noble gas, therefore it adsorbs and desorbs monatomically. There are no internal energies to consider. There is no activation energy and the adsorbate bond is weak. Also, the Potential Energy Surface (PES) is relatively smooth.

Even though physisorption is modeled only for adsorption and scattering, all three surface processes (adsorption, scattering, and desorption) are related. Adsorption and scattering have in common the collision of a gas molecule with the surface. The link between adsorption and desorption is even more direct, because they are inverse processes of one another [78:161-166]. The former is concerned with a gas-phase molecule adhering to the surface, while the latter considers a molecule on the surface being released to the gas-phase. An understanding of one of these processes invites greater insight into the other.

The assumption that the problem is symmetric with respect to time is termed microscopic reversibility, a stricter form of the principle of detailed balance. Time symmetry, or T-symmetry, indicates that the physical laws are symmetric whether time is advanced forwards or backwards. Detailed balance is only applicable under equilibrium conditions. However, microscopic reversibility applies even in non-equilibrium situations. The principle of detailed balance provides a mechanism by which the properties of a system in equilibrium are maintained [29]. Population and depopulation rates of every microscopic and macroscopic state are equal under detailed balance. However, microscopic reversibility assumes that the trajectory and state of a molecule can be simulated forwards and backwards in time with identical results, which holds under Hamiltonian dynamics. Thus, under microscopic reversibility, a molecule des-

orbing from a surface provides information on a molecule adsorbing to a surface under identical conditions. Recently, microscopic reversibility was shown to also hold for open systems, bridging the first and second laws of thermodynamics [119].

The novel adsorption and scattering DSMC method developed, called the Modified Kisliuk with Scattering (MKS) method, is simple. The main points are: (1) determine if an impinging gas molecule collides with an adatom or with the surface by comparing a random uniform number with the fractional surface coverage, (2) calculate the molecule's scattering energy and angles by incorporating an existing scattering computational method [Cercignani-Lampis-Lord (CLL)], (3) compare the scattering energy with the well-depth parameter of the PES to determine whether the molecule adsorbs or scatters, and (4) repeat as necessary.

In spite of its simplicity, MKS recreates experimental data for Xe-Pt(111) remarkably well. Thus, a strength of the DSMC method is that underlying assumptions can be included in the model in a relatively simple manner. Analytical expressions do not need to be developed every time an assumption is added or altered. One can pick and choose the assumptions deemed relevant, and build on them as more complex problems are considered. MKS is actually a transformation (or translation) of an existing model [Modified Kisliuk (MK)] into a DSMC algorithm, although this was not recognized originally as MKS was being developed. MKS was built independently from MK with assumptions that expressed the dominant underlying physical phenomena of the Xe-Pt(111) system. Once MKS results were matched with experimental data, it was discovered that the assumptions behind MKS perfectly coincided with the assumptions that went into MK. Hindsight thus showed that analytical models that cannot be directly utilized in DSMC applications, can however be translated into a DSMC algorithm simply by implementing their underlying assumptions. Furthermore, existing models can be augmented, or extended, by this method. The MK

model only calculates the probability that a gas molecule adsorbs as a function of current adsorbate coverage. However, in addition to the adsorption probability, MKS also calculates the scattering energy and angles.

1.2 Chemisorption

Thermal desorption (LH) is modeled in Chapter III for H_2 on the (100) surface of copper [H_2-Cu(100)], a chemisorptive system.[4] Hydrogen is the most prevalent residual gas in metal vacuum systems at very low pressures [Ultra-High Vacuum (UHV) and Extreme-High Vacuum (XHV)]. In fact, researchers who seek to lower the pressure of a metal system down to 10^{-10} Pa (XHV) view the mitigation of hydrogen outgassing as the most challenging problem they face [141], and is investigated in the literature [40; 42; 43; 171]. The H_2-Cu gas-surface system is considered because it is the most commonly-studied example of activated chemisorption. The (100) face of copper was chosen simply because there is sufficient modeling and experimental data in the literature for the H_2-Cu(100) system. Some other resources in the literature include two methods of doping hydrogen onto copper for desorption studies [5; 51], and various investigations into thermal desorption (LH) for the D_2-Cu [115; 116] and H_2-Cu [25; 56; 87; 132; 144; 159] systems.

Hydrogen atoms tend to permeate metals relatively easily [54; 55; 130]. Thus, even if a surface is completely clear of adsorbate, hydrogen desorption and outgassing may still occur during system operation. Sometimes, the hydrogen will first permeate, then bond in sub-surface sites in the metal (even though there is some discussion on this matter) [102; 124]. For hydrogen permeating copper, it is possible that H_2 recombines in a subsurface state [114], and receives additional energy as it desorbs due to the (bulk) absorption energy barrier [33]. Typically in desorption experiments,

[4]The nomenclature for surface structure [i.e. (100)] is discussed in Section 3.1.

hydrogen is supplied to the surface via thin-membrane permeation. However, one can supply hydrogen directly to the surface via an atomic beam in order to avoid any complicating permeation effects [146].

LH reactions are driven by the thermal energy of the surface being transferred to the adsorbate; they are rarely caused by adsorbate excitations, since the energy transfer rate from the lattice to the adsorbate is typically 13 orders of magnitude greater than the reaction rate [60]. However, LH desorption events result in non-equilibrium distributions, heavily influenced by the curvature of the PES [168]. One reason for this result is that the potential energy barrier to recombination at the surface accelerates desorbing molecules away from the bulk (and inhibits adsorption) [146], thus providing desorbed products with higher-than-average kinetic energies than would otherwise be available simply from thermal equilibrium with the surface. In addition, the desorption of hydrogen from copper is an early-barrier process, implying that strong energy transfers occur after recombination [139], further perturbing the molecule's distributions from equilibrium.

Even though it will not be studied here, activated dissociative chemisorption (adsorption) is an important area of study since it is the rate-limiting step in many gas-surface reactions [145]. It is mostly a function of the normal component of the incident energy, a relationship known as normal energy scaling [5]. However, the surface temperature also aids in molecular dissociation [120]. Also, adsorption is enhanced for vibrationally excited H_2 molecules, where around 60% of the vibrational energy is expended in overcoming the activation barrier [114]. In order to understand how each of these mechanisms contributes to adsorption, state-resolved adsorption [76] and scattering [169; 170] has been studied for H_2-Cu(100). Electronically non-adiabatic effects are thought to affect scattering, where hydrogen molecules lose some vibrational energy while exciting copper electrons [101]. Other areas of interest include

low-temperature adsorption [H_2-Cu(100)] [138], how to prepare a copper surface for scattering studies [12], and various theoretical and experimental publications [H_2-Cu] [8; 34; 36; 38; 56; 58; 85; 90; 123; 158; 159; 161; 162].

Unfortunately, chemisorption cannot successfully be modeled in the same manner as physisorption. Physisorption concerns itself with systems in which weak van der Waals interactions dominate. However, in chemisorptive systems, the electronic structure of the adsorbate is significantly modified due to the presence of the surface. As such, the corrugation and shape of the PES can play a large role in chemisorptive dynamics. Thus, a different approach is followed for chemisorption modeling, which is to model the trajectory of each desorbing molecule in a Classical Trajectory (CT) formulation under the influence of a six-dimensional (6D) PES.

The PES describes the interaction between a surface and a molecule. From the PES, one can calculate the forces acting on the molecule, and given appropriate initial conditions, the molecule's position and velocity as well. For a single atom, only three degrees of freedom, or three dimensions (3D), are required to adequately model the PES. For a diatomic molecule, six degrees of freedom are needed. Likewise, for a molecule with N atoms, there are potentially $3N$ degrees of freedom required [65]. One may simplify the calculations by neglecting some of the degrees of freedom. However, it has been shown that all six dimensions must be considered when modeling associative (dissociative) chemisorption for a diatomic molecule [44; 45]. Even though all six degrees of freedom are addressed here, there is assumed to be no change in the electronic state of the system during the reaction. In other words, the reactions are assumed to be electronically adiabatic. Also, since the motion of the admolecule can be obtained from the PES, it is not necessary to identify frustrated (or hindered) degrees of freedom.[5]

[5]Since adsorbed molecules behave differently than free molecules, their motions are sometimes referred to as frustrated or hindered, such as hindered rotation or hindered translation [17; 26; 66;

Lattice motion is assumed to be insignificant. Thus, a Rigid Surface (RS) assumption is employed, which considers bulk atoms frozen in time and space [60]. One reason for this assumption is that phonons can safely be neglected when modeling surface effects for a light molecule such as H_2 [1; 2; 122; 149; 150; 151; 158]. Also, the time scale for hydrogen association (dissociation) on copper is much smaller than that of the substrate motion. Another justification is that surface reconstruction is unimportant in this case, since adsorbed hydrogen perturbs the substrate lattice only minimally [60]. For a more refined look, however, the reader is referred to current investions on how small perturbations in lattice position away from equilibrium can effect the potential energy landscape of the H_2-Cu interaction [22; 177].

Wiesenekker et al. [83; 84; 174] developed a 6D PES to describe the molecule-surface interaction in the H_2-Cu(100) system. This PES is based on slab calculations with the Generalized Gradient Approximation (GGA) in DFT. It is expressed as a fit to an analytical form, bypassing the need for computationally intensive on-the-fly DFT calculations. An analytical fit also provides a high degree of flexibility in matching the PES to experimental and simulated energy values. The full 6D PES is achieved by splicing together eight two-dimensional (2D) PES slices [175; 176], which are individually anchored to experimental results. This 6D PES was specifically tailored to be accurate in the region between the gas phase and the Transition State (TS) (the location or zone where the individual adatoms combine into a molecule). Within the TS, the PES is fairly accurate, and between the TS and the surface, the PES is inaccurate.

There are other options when considering a PES for the H_2-Cu(100) system [32; 37; 48]. One is the common London-Eyring-Polyani-Sato (LEPS) form [109; 154], known for its computational simplicity and speed. The LEPS form assumes that atom-atom

110; 129; 178].

and atom-surface interactions are adequately described by Morse potentials [109]. However, the LEPS form contains only a few adjustable parameters, and is therefore less flexible than the Wiesenekker PES. Another option is the PES constructed by Olsen et al. [126]. Unfortunately, they did not publish their fitting parameters, and hence their PES cannot be reproduced. It should be noted that the methods presented here are applicable to any PES (LEPS, analytical, etc.). In fact, studies concerning H_2-Cu PESs continue to be reported.

The trajectories of desorbing molecules are modeled within the CT formulation. CT simulations ignore the quantum effects of tunneling and interferences [88; 118]. These effects may be neglected for relatively heavy molecules, and for surfaces at temperatures above their Debye temperature [167]. The Debye temperature of a solid is interpreted as the temperature at which all phonon modes are excited. Even though H_2 is considered to be a light molecule, the temperatures considered in this work for copper are well above its Debye temperature of 344 K. Therefore, the CT formulation is appropriate here. A significant benefit of modeling desorption with CT simulations is that rovibrational state distributions can be calculated, which have been shown to be important in H_2-Cu dynamics [152]. As an aside, the Quasi-Classical Trajectory (QCT) method attempts to include quantum effects by incorporating Zero-Point Energy (ZPE) in the initial conditions [19; 108].

Desorption calculations, in order to be incorporated into DSMC codes, need to provide information about the molecule including its velocity, and its rotational and vibrational energies. Fortunately, CT simulations are able to do just that. Recently, kinetic Monte Carlo (MC) simulations of surface reactions have been coupled with continuum computational fluid dynamics (CFD) methods [155]. However, there is no indication in the literature that CT has been developed for use in DSMC simulations before this work.

Also, for time-accurate simulations, a method for timing desorption events must be included. Timing will be incorporated by noting that each desorption event for H_2-Cu(100) can be assumed to be independent of one another, thus representing a Poisson process. A rate of surface activity then allows for the time between successive events to be calculated. In this manner, desorption events will occur during specific times in the DSMC simulation. More about this topic will be discussed in Section 3.8.

1.3 Contributions

In summary, this research develops thermal desorption and adsorption models in a framework to incorporate into Direct Simulation Monte Carlo codes. As a result, plasma-surface modeling will greatly benefit. Current state-of-the-art plasma-surface interaction modeling does not capture essential molecular physics. For example, adsorption is represented by a single probability, scattering is calculated with a probability curve, and desorption is assumed to exhibit equilibrium distributions [165].

This work is a significant step forward for the aeronautical and mechanical engineering communities in modeling dynamic surface phenomena (both physisorptive and chemisorptive) at the microscopic level. These fields have not previously had access to microscopic surface modeling within the Direct Simulation Monte Carlo framework. Microscopic methods have been neglected in favor of macroscopic fluid approaches focusing on reaction rates [103; 105; 163]. Unfortunately, macroscopic approaches are not able to model in detail the state-specific dynamics of desorbing molecules, even when considering many adsorbate spatial configurations [47; 50; 67; 68; 77; 79; 80; 81; 82; 91; 100; 104; 112; 125; 128; 173; 181; 183].

In Chapter II (Physisorption), a new algorithm is developed, called the Modified Kisliuk with Scattering method. This model is the first of its kind to account for both adsorption and scattering. It accurately calculates adsorption probabili-

ties. It also predicts super-elastic scattering profiles, a capability currently lacking in Direct Simulation Monte Carlo models. Scattering calculations are even improved from state-of-the-art models. Gas-adlayer interactions are considered, a first for the Cercignani-Lampis-Lord kernel. Finally, it is demonstrated how the Modified Kisliuk with Scattering method can be used to determine accommodation coefficients.

In Chapter III (Chemisorption), another novel method is introduced to model thermal desorption for Direct Simulation Monte Carlo applications. The equations of motion are non-dimensionalized, a description surprisingly not found in the literature. Multiple transition states are incorporated into the calculations, whereas researchers in the field have only considered a single transition state until now. A truncated Maxwell-Boltzmann distribution is developed and its accept-reject form is derived. Correct event timing, adapted here for Direct Simulation Monte Carlo applications, is included for temporally-accurate simulations. It is shown that Gaussian weighting is not required for this method, an unexpected result which greatly reduces computational run times. Also, the absorption barrier energy due to permeation and/or diffusion is shown to significantly contribute to thermal desorption. Specifically, it directly affects the translational energy, while it has little impact on the internal energies of desorbing molecules.

II. Physisorption

There is an immediate opportunity to improve surface effects modeling in the DSMC field. Currently, adsorption is completely ignored due to its complex nature. The modeling of scattering received significant attention a little less than 20 years ago. However, there has been little improvement since then. The simplest assumption for scattering is that molecules do so specularly. HPM simulations usually only include this specular reflection boundary condition. Other fields, such as hypersonics, have adopted a more advanced technique with the CLL kernel; the CLL boundary condition is capable of producing a somewhat realistic lobular scattering profile [97].

This chapter details the development and results of a new model, MKS, that addresses both adsorption *and* scattering for a physisorptive system in a DSMC framework. First, a brief introduction to simple adsorption models will be given, building to a discussion of the MK model. Then, the MKS method will be developed, including a detailed discussion of the CLL kernel. Finally, adsorption results from MKS will be compared with experimental data with respect to the Xe-Pt(111) gas-surface system, illustrating the benefits of MKS. Besides being the first method to handle both adsorption and scattering in a DSMC framework, MKS also improves the scattering properties of the state-of-the-art DSMC scattering model.

2.1 Previous Adsorption Models

This section introduces simple adsorption models, in preparation to discuss the new MKS model in Section 2.2. Starting with Henry's Law, the historical models will progressively increase in complexity, until an adsorption model capable of handling the behavior of Xe-Pt(111) is explained (MK).

2.1.1 Henry's Law.

The simplest adsorption model, Henry's Law, assumes (1) a gas molecule will adsorb independently of the adlayer, and (2) all adsorption sites are equivalent [62:175-197]. For this model, the adsorption probability is independent of coverage, or

$$S(\theta) = S_0, \tag{1}$$

where θ is the adlayer coverage and S_0 is the initial adsorption probability.[1]

2.1.2 Langmuir Model.

The Langmuir model is slightly more complicated than Henry's Law because it assumes (1) adatoms occupy specific adsorption sites on the surface, (2) there is no adatom mobility, (3) a gas molecule does not adsorb if it encounters an occupied site, and (4) there are no lateral interactions [62:240; 106]. This model predicts that a gas molecule is adsorbed into an unoccupied site with probability S_0, while gas molecules are never adsorbed onto occupied sites. Thus, the adsorption probability $S(\theta)$ decreases linearly with coverage,

$$S(\theta) = S_0(1 - \theta). \tag{2}$$

2.1.3 Kisliuk Model.

Kisliuk developed a model that considered adsorption via both an intrinsic and an extrinsic precursor, with no direct Langmuirian adsorption [10]. An intrinsic precursor in adsorption is a molecule that is occupying an adsorption site, but that has not fully adsorbed to the surface. In other words, the molecule is still mobile on the surface.

[1]For a full listing of all the symbols used in this document, including their respective units, please refer to Appendix A.

Similarly, an extrinsic precursor is a molecule that occupies an adsorption site *above* the adlayer, which has not fully adsorbed to the adlayer (or surface). In other words, precursors are transitory states of an adatom as it either adsorbs or desorbs. In steady-state,

$$S(\theta) = \frac{S_0}{1 + K\dfrac{\theta}{1-\theta}}, \tag{3}$$

where S_0 and K are functions of the trapping probability into precursor states as well as rate constants for the intrinsic and extrinsic precursor states. This model assumes (1) no lateral interactions and (2) a random adlayer configuration. It turns out that according to this model, $S(\theta)$ also decreases with increasing coverage. However, there are systems where the opposite trend holds, such as Xe-Pt(111) [10].

2.1.4 Modified Langmuir Model.

Another model, which will here be referred to as a modified Langmuir model, was proposed to fit experimental data, which assumed that the adsorption pathways included both direct Langmuirian adsorption and mobile adsorption onto the second adlayer. In other words,

$$S(\theta) = S_0(1-\theta) + S_0^*\theta, \tag{4}$$

where S_0^* is the adsorption probability onto the adlayer. For $S_0^* > S_0$, $S(\theta)$ increases with coverage.

2.1.5 Modified Kisliuk Model (MK).

The MK model was developed by combining the original Kisliuk model with the modified Langmuir model [10]. MK assumes (1) Langmuirian adsorption for a gas molecule in contact with an unoccupied site with adsorption probability S_0, (2) extrinsic precursor mobile adsorption with adsorption probability S_0^*, (3) the configu-

ration of the adlayer is random, and (4) no lateral interactions exist. In steady-state, assuming that the extrinsic precursor coverage is small,

$$S(\theta) = S_0(1-\theta) + S_0^*(1-\theta)\frac{q_m\theta}{1-q_m\theta}, \tag{5}$$

where q_m is a function of extrinsic precursor rate constants.

2.2 Novel Adsorption and Scattering Method

With that brief background in mind, a novel adsorption and scattering method is developed in this section. Termed the Modified Kisliuk with Scattering (MKS) method, this new technique builds on the assumptions of MK for DSMC and the Multi-Stage (MS) gas-surface interaction model. It is capable of modeling both adsorption and scattering, an accomplishment previously unattained. Further, scattering properties of MKS are shown to be superior to those of state-of-the-art calculations with the CLL kernel. MKS assumes (1) no precursor-mediated adsorption for impingement on an unoccupied site, (2) mobile precursor-mediated adsorption for impingement on the adlayer, (3) the adlayer configuration is random, and (4) no lateral interactions are present.

2.2.1 Multi-Stage (MS) Gas-Surface Interaction Model.

The implementation of MKS is similar to that of the MS gas-surface interaction model [180]. The MS model is applicable to the thermal scattering regime [53:103], where the interactions produce lobular and diffuse scattering. The MKS method presented in this work is also limited to this regime, and one should be aware of the conditions under which it loses applicability. The radius parameter $\mathcal{R}$ is the main determining factor of the scattering regime, and a value of $\mathcal{R} \geq 1.5$ indicates thermal

scattering. $\mathcal{R}$ is defined as

$$\mathcal{R} \equiv \frac{R_{\text{eff}}}{R_c}, \tag{6}$$

where R_{eff} is the effective interaction radius, or the smallest distance between the gas and surface atoms during a gas-surface collision, and R_c is a critical value of R_{eff}. For a given incident translational energy E_{tr}, R_{eff} is estimated from the one-dimensional (1D) approximation

$$\frac{E_{\text{tr}}}{\varepsilon_{\text{LJ}}} \approx \left(\frac{r_0}{R_{\text{eff}}}\right)^{12} - 2\left(\frac{r_0}{R_{\text{eff}}}\right)^{6}, \tag{7}$$

where ε_{LJ} is the Lennard-Jones (LJ) well-depth parameter for the interaction between the gas molecule and a surface atom, and r_0 is the equilibrium distance between the gas molecule and a surface atom. R_c is then the distance from the gas molecule to a surface atom as it crosses the surface plane. For the commensurate layer on a (111) surface, the critical value is $R_c = d_0/\sqrt{3}$, where d_0 is the equilibrium distance between surface atoms.[2]

The MS model breaks down the gas-surface collision into three steps. First, translational and rotational energies are calculated from a model equation, which is based on MD simulations of that specific collision with those specific gas and surface species. Next, from the PES, the scattering angles are found. Finally, depending on the results from the first two steps, the gas molecule either scatters, re-collides with, or is trapped by the surface. If the gas molecule re-collides with the surface, then the process is repeated, until a maximum of ten collisions occur. At that point, the gas molecule is trapped by the surface, and is assumed to desorb diffusely at the surface temperature T_s during that same time step. Trapping is defined for an adatom in a weakly-bound mobile state. However, once the adatom is more strongly bound to the surface, it is said to stick or adsorb. The MS model only calculates scattering

[2]The commensurate layer on a (111) surface is also described as $(\sqrt{3}\times\sqrt{3})R\,30°$. The unit surface cell of adsorbate is configured in a rhombus, with all four sides of length $\sqrt{3}$ times the length of the bulk unit cell, and rotated 30° from the bulk unit cell's orientation.

and trapping over a simulation time step, meaning that molecules trapped on the surface are scattered by the end of that time step; it does not consider adsorption. In fact, the literature does not appear to contain *any* DSMC adsorption (or desorption) models.

2.2.2 New Algorithm.

The MKS method, on the other hand, can handle adsorption as well as scattering. Like MS, MKS also breaks up the gas-surface collision into stages:

1. Determine if the gas molecule collides with an adatom or with the surface. A uniform random number $0 \leq R \leq 1$ is compared with the adlayer coverage $0 \leq \theta \leq 1$. If $R \leq \theta$, then the gas molecule collides with an adatom. Otherwise, the gas molecule collides with the surface. θ is measured in monolayers (ML).

2. The gas molecule scatters using a scattering method or kernel. Accommodation coefficients, defined below, are provided for both the gas-surface (α_n, α_t) and the gas-adatom ($\alpha_{n,\mathrm{ad}}$, $\alpha_{t,\mathrm{ad}}$) systems. $\alpha_{n,\mathrm{ad}}$ and $\alpha_{t,\mathrm{ad}}$ are new coefficients, introduced with MKS to account for the gas-adlayer interactions. Note that Langmuirian kinetics are recovered for $\alpha_{n,\mathrm{ad}}$, $\alpha_{t,\mathrm{ad}} = 0$.

3. If the post-collisional normal translational energy $E'_{\mathrm{tr},n}$ of the gas molecule is sufficient to escape the PES ($E'_{\mathrm{tr},n} \geq 2\varepsilon_{\mathrm{LJ}}$), then it scatters. Here, $\varepsilon_{\mathrm{LJ}}$ is the Lennard-Jones potential well parameter for the interaction between the gas molecule and *a* surface molecule (*not* the entire surface). The threshold value of $2\varepsilon_{\mathrm{LJ}}$ was determined by Yamanishi et al. and is discussed below [180].

4. If the gas molecule cannot escape the PES, but has enough total energy E'_{tot} to overcome the adsorption energy and has not collided with the surface more than

ten times, then it re-collides with the surface. In other words, if $E'_{\text{tot}} \geq E_{\text{ads}}$ and $N_{\text{colls}} \leq 10$, then return to Step 1 using post-collisional values.

5. Otherwise, the gas molecule is adsorbed.

The MKS method differs from the MS model in a few respects. First, any scattering method or kernel, including a model equation, can be used to determine scattering values in MKS, while MS requires a tailor-made model equation for each separate case. The CLL scattering kernel [97] was chosen since current DSMC codes already use the CLL kernel. However, MKS is modular in that any scattering kernel or model could be employed in the place of the CLL kernel. CLL requires accommodation coefficients (α_n, α_t, $\alpha_{n,\text{ad}}$, and $\alpha_{t,\text{ad}}$) to be specified, and so they are utilized here. But if a different scattering kernel or method were to be incorporated into MKS instead of CLL, then different parameters would be required. A contribution made here is applying the CLL kernel to adlayer scattering. Up until now, only surface scattering has been considered with CLL. Next, the MS model considers only a clean surface while MKS accounts for an adlayer being present, up to one monolayer. This limitation illustrates a drawback of MS, because the model equation must be developed for each individual gas-surface system. In fact, adsorbates alter the PES of the interaction, and therefore a multitude of model equations would ideally have to be developed for a single gas-surface system. The new MKS model is not limited to perfectly-clean surfaces. Additionally, the criteria have been changed for determining whether or not a gas molecule overcomes the potential well of the PES. From MD simulations, Yamanishi et al. claim that when a gas molecule scatters off of a surface, it has an average potential energy of $2\varepsilon_{\text{LJ}}$ [180]. In the MS model, the gas molecule scatters if both the post-collisional normal and tangential translational energies are greater than or equal to this average potential energy (i.e., $E'_{\text{tr},n} \geq 2\varepsilon_{\text{LJ}}$ and $E'_{\text{tr},t} \geq 2\varepsilon_{\text{LJ}}$). However, while comparing MKS with experimental adsorption probability data, this research

found that the gas molecule should scatter only if $E'_{\mathrm{tr},n} \geq 2\varepsilon_{\mathrm{LJ}}$. Hence, no restriction was placed on $E'_{\mathrm{tr},t}$ in MKS. A sensitivity analysis was performed to determine the optimal threshold value. It was found in this work that $2\varepsilon_{\mathrm{LJ}}$ is reasonable. A brief discussion of this finding is in Section 2.4. Finally, MS includes rotational energy while MKS in its current form does not consider internal energy modes.

2.2.3 Accommodation Coefficients.

Before the typical CLL kernel can be reviewed, accommodation coefficients should be discussed since the CLL kernel requires them as inputs. Accommodation coefficients are defined as [127]

$$a_Q \equiv \frac{\Phi_i^Q - \Phi_r^Q}{\Phi_i^Q - \Phi_w^Q}, \tag{8}$$

where Q is the molecular property in question, Φ_i^Q and Φ_r^Q are the incident and reflected fluxes of Q, respectively, and Φ_w^Q is the reflected flux of Q at complete accommodation. Typical properties of Q are tangential momentum mc_t, normal momentum mc_n, and kinetic energy tangential $mc_t^2/2$ and normal $mc_n^2/2$ to the surface. Here, m is the molecular mass, c_t is the tangential velocity to the surface, and c_n is the normal velocity to the surface. Accommodation coefficients for these properties are here referred to as σ_t, σ_n, α_t, and α_n, respectively, so that

$$\sigma_t \equiv \frac{mc_t - mc'_t}{mc_t - mc_w} = \frac{c_t - c'_t}{c_t}, \tag{9}$$

where c_t' is the post-collisional tangential speed, and c_w is the speed of the wall, which in this case is stationary. Similarly,

$$\begin{aligned}\sigma_n &\equiv \frac{c_n - c_n'}{c_n}, \\ \alpha_t &\equiv \frac{c_t^2 - {c_t'}^2}{c_t^2}, \\ \alpha_n &\equiv \frac{c_n^2 - {c_n'}^2}{c_n^2},\end{aligned} \tag{10}$$

where c_n' is the post-collisional normal speed. A useful relation that can easily be shown is $\alpha_t = \sigma_t(2 - \sigma_t)$.

This work extends CLL's usefulness by applying it to adlayer scattering. Therefore, in addition to the typical accommodation coefficients needed by CLL (α_n and α_t), adlayer-specific coefficients are also required ($\alpha_{n,\mathrm{ad}}$, $\alpha_{t,\mathrm{ad}}$).

2.2.4 Cercignani-Lampis-Lord Scattering Kernel.

The CLL scattering kernel is useful because it satisfies the principle of detailed balance (reciprocity), it calculates sufficiently realistic lobular scattering angle and energy distributions, and is well-suited for implementation in DSMC. Not included in this work are Lord's extensions to CLL, which are diffuse scattering with partial accommodation of translational kinetic energy, vibrational energy for a rigid-rotor/harmonic-oscillator diatomic molecule, partially diffuse scattering, and vibrational energy for an anharmonic oscillator [98; 99]. Two of the extensions, which consider vibrational energy, are not applicable to monatomic xenon. Future research may address these extensions, and apply them to MKS if applicable. Two system-specific accommodation coefficients are required for CLL, one for the normal kinetic energy α_n and one for the tangential kinetic energy α_t. α_n and α_t depend upon the gas and the surface, and are typically functions of temperature. Coefficients have

been measured experimentally [52], as well as predicted with MD simulations [49]. A helpful explanation of the CLL kernel is given by Liou and Fang [96:180-187], while a slightly modified implementation is presented in [127].

The CLL scattering kernel first applied to DSMC calculations by Lord is implemented in MKS [97]. Even though CLL is applied here for the first time to adlayer scattering, its implementation remains the same. Please note that for this section only, all of the velocities are normalized by the most probable velocity $\sqrt{2kT_s/m}$, consistent with Lord's development, where k is the Boltzmann constant and T_s is the surface temperature. As a result, kinetic energies (such as u^2) are in units of kT_s. For each of the tangential velocity components u and v, the probabilities that the post-collisional velocities fall between u' and $u'+du'$, and v' and $v'+dv'$, respectively, are,

$$\begin{aligned} P(u \to u')\,du' &= \frac{1}{\sqrt{\pi\alpha_t}} \exp\left\{-\frac{[u'-(1-\sigma_t)u]^2}{\alpha_t}\right\} du', \\ P(v \to v')\,dv' &= \frac{1}{\sqrt{\pi\alpha_t}} \exp\left\{-\frac{[v'-(1-\sigma_t)v]^2}{\alpha_t}\right\} dv', \end{aligned} \tag{11}$$

where $P(u \to u')$ and $P(v \to v')$ are the scattering kernels. The detailed balance relations, or reciprocity, are then satisfied for both components,

$$\begin{aligned} \exp(-u^2)P(u \to u') &= \exp(-u'^2)P(-u' \to -u), \\ \exp(-v^2)P(v \to v') &= \exp(-v'^2)P(-v' \to -v), \end{aligned} \tag{12}$$

The show that the relations in Equation (12) hold, rearrange the exponential terms,

and recall that $\alpha_t = \sigma_t(2-\sigma_t) = 2\sigma_t - {\sigma_t}^2$, so that

$$\begin{aligned}\exp(-u^2)P(u\to u') &= \frac{1}{\sqrt{\pi\alpha_t}}\exp\left\{-\frac{\alpha_t u^2 + [u'-(1-\sigma_t)u]^2}{\alpha_t}\right\},\\ &= \frac{1}{\sqrt{\pi\alpha_t}}\exp\left\{-\frac{u'^2-(1-2\sigma_t)uu'+u^2}{\alpha_t}\right\},\end{aligned} \tag{13}$$

and,

$$\begin{aligned}\exp(-u'^2)P(-u'\to -u) &= \frac{1}{\sqrt{\pi\alpha_t}}\exp\left\{-\frac{\alpha_t u'^2 + [-u-(1-\sigma_t)(-u')]^2}{\alpha_t}\right\},\\ &= \frac{1}{\sqrt{\pi\alpha_t}}\exp\left\{-\frac{u^2-(1-2\sigma_t)uu'+u'^2}{\alpha_t}\right\},\end{aligned} \tag{14}$$

proving that

$$\exp(-u^2)P(u\to u') = \exp(-u'^2)P(-u'\to -u). \tag{15}$$

Similarly,

$$\exp(-v^2)P(v\to v') = \exp(-v'^2)P(-v'\to -v). \tag{16}$$

The normalization conditions are also satisfied,

$$\begin{aligned}\int_{-\infty}^{\infty} P(u\to u')\ du' = 1,\\ \int_{-\infty}^{\infty} P(v\to v')\ dv' = 1,\end{aligned} \tag{17}$$

which state that the cumulative probabilities over all scattered velocities are unity.

For the normal velocity component w, the probability that the post-collisional velocity is between w' and $w'+dw'$ is,

$$P(w\to w')\,dw' = \frac{2w'}{\alpha_n}\ \exp\left[-\frac{w'^2+(1-\alpha_n)w^2}{\alpha_n}\right]\ \mathrm{I}_0\left(\frac{2\sqrt{1-\alpha_n}\,ww'}{\alpha_n}\right)\ dw', \tag{18}$$

where $P(w\to w')$ is a scattering kernel, and I_0 is the modified Bessel function of the

first kind. The reciprocity condition is

$$|w| \exp\left(-w^2\right) P(w \to w') = w' \exp\left(-w'^2\right) P\left(-w' \to -w\right), \tag{19}$$

where positive velocities are taken to be away from the surface. This condition is different from Equation (12) since a bias towards higher normal velocities occurs in the velocity distribution of impinging molecules. The normalization condition is also satisfied,

$$\int_0^\infty P(w \to w')\ dw' = 1. \tag{20}$$

Lord presented a numerical implementation of the CLL model utilizing a geometrical representation, shown in Figure 1 [97]. The figure can be used for both the normal and tangential velocity components. Consider first the tangential velocities u and v. Point P indicates the state of the impinging molecule before it collides with the surface. The abcissa and ordinate each represent one of the tangential velocities, and so the distance from the origin OR is the tangential post-collisional velocity c_t' since R is the state of the reflected molecule. P is shown on the horizontal axis because the velocity distributions are invariant with respect to rotation. The length OP is $|u|$. OQ is the average value for the post-collisional speed $\langle c_t' \rangle = |u|\sqrt{1-\alpha_t}$, which can be seen from the fact that Equation (11) is a Gaussian distribution with a mean of $\langle c_t' \rangle$. The probability that the final state of the molecule lies in an area dA at (r_c, θ_c) is

$$P(u \to u') P(v \to v')\, du'\, dv' = \frac{1}{\pi \alpha_t} \exp\left(-\frac{r^2}{\alpha_t}\right) dA, \tag{21}$$

where $dA = r_c\, dr_c\, d\theta_c$, r_c is the distance QR, and θ_c is the angle $\angle PQR$. Note that

the probability is independent of θ_c. u' and v' are calculated from

$$\begin{aligned}
\theta_c &= 2\pi R_1, \\
r_c &= \sqrt{-\alpha_t \ln R_2}, \\
u' &= |u|\sqrt{1-\alpha_t} + r_c \cos\theta_c, \\
v' &= r_c \sin\theta_c,
\end{aligned} \tag{22}$$

where R_1, $R_2 \in [0,1]$ are uniform random numbers. In actual calculations, one first transforms velocities to the rotated reference frame in which $v = 0$. Once the post-collisional velocities are obtained, one then transforms them back to the original frame of reference.

For the normal velocity component w, many items stay the same. P is the molecule's initial state, the distance OR is w', R is the post-collisional state of the molecule, OP is $|w|$, OQ is $|w|\sqrt{1-\alpha_n}$, and

$$\begin{aligned}
\theta_c &= 2\pi R_3, \\
r_c &= \sqrt{-\alpha_n \ln R_4}, \\
w' &= \sqrt{r_c^2 + (1-\alpha_n)w^2 + 2r_c|w|\sqrt{1-\alpha_n}\cos\theta_c},
\end{aligned} \tag{23}$$

where R_3, $R_4 \in [0,1]$ are uniform random numbers, and w' was determined with the Law of Cosines.

It should be noted here that MKS is not linked to CLL in particular, nor to any specific scattering kernel nor method. MKS is modular in that any scattering method or kernel can be substituted in the place of CLL. MKS is robust in that it does not need to be modified to accommodate application-specific scattering kernels. It has previously been noted that CLL is not completely realistic [97], even though

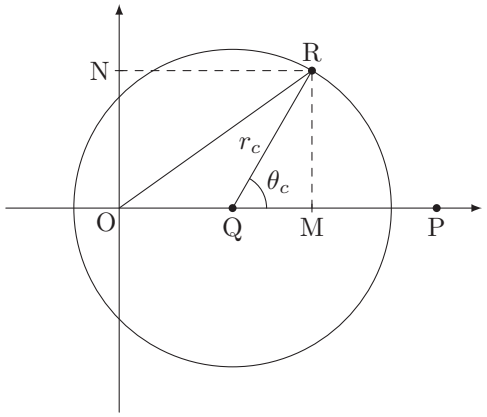

Figure 1. Geometric representation of the CLL scattering model.

it has been considered sufficient for state-of-the-art DSMC calculations [127]. In fact, other scattering kernels have been developed for specific applications [179; 180]. MKS could easily incorporate other scattering kernels as long as they are amenable to DSMC techniques, making it a strong

2.3 Xe-Pt(111) System

A brief overview of Xe-Pt(111) interactions and properties is included in this section since adsorption results will be presented with respect to the Xe-Pt(111) system. The Xe-Pt(111) system includes attractive lateral interactions among the adatoms [134]. Xenon is a 2D gas on the surface if T_s is either above the critical temperature T_c, which in this case is 120 K, or if $T_s < T_c$ and $0 \leq \theta \leq 0.06$. Otherwise, the xenon phase is a 2D gas with either a 2D solid ($T_s < T_{\text{tr}}$) or a 2D liquid ($T_s > T_{\text{tr}}$), where T_{tr} is the triple-point temperature [134]. MKS assumes no lateral adatom interactions, and that the adlayer structure is commensurate up to $\theta = 1$.[3] In reality, the commensurate monolayer becomes saturated at $\theta \approx 0.4$. The monolayer transitions through several incommensurate phases until the first monolayer is filled [74]. These

[3]A commensurate layer is one in which adatoms occupy energetically-favored adsorption sites, and is dominated by the substrate-adatom potential. An incommensurate layer, on the other hand, is determined by the natural adlayer interatomic distance, or the adatom-adatom lateral interactions [75].

phase transitions occur due to competing forces. As long as adsorbate-substrate interactions dominate, the phase remains commensurate. However, once the lateral adatom forces begin to dominate, the phase transitions to incommensurate [74]. Even though one might expect to see effects of the phase transitions in experiments, none are observed in Reference [10]. Arumainayagam et al. caution that this result may be due to the relatively high (1%) defect density on their crystal surface. From Temperature-Programmed Desorption (TPD) spectra, it has been observed that first-order desorption occurs at $\theta \leq 0.10$, while for $\theta > 0.10$, zero-order desorption is present [173]. The 2D gas at low coverages explains the first-order behavior, and the zero-order desorption is explained by the coexisting 2D solid and gas phases for higher coverages. Also, xenon atoms have a higher mobility than expected, due to effective transfer of the adsorption energy into kinetic energy [93].

Xe-Pt(111) is a good system with which to initially compare an adsorption method because it is relatively simple. Xenon is an inert gas, and the Pt(111) samples may be single-crystal, clean, and well-defined metal surfaces with a relatively smooth PES. The adsorption of xenon on Pt(111) is a non-activated process, meaning that no chemical reaction occurs during adsorption. It is a weakly-interacting gas-surface system since the energy is transferred to the surface by exciting phonons. No internal energy transfer occurs in the incident species.

2.3.1 Xe-Pt(111) Potentials.

In simulating the dynamics of the Xe-Pt(111) system, different potentials have been investigated, namely the LJ, the Barker-Rettner (BR), and the Morse potentials. The performance of MKS will be compared with calculations from the BR and Morse potentials in Section 2.4.2, and since the Morse potential is based on the LJ potential, all three potentials will be briefly discussed here.

The LJ potential $V_{\rm LJ}$ has two adjustable parameters ($\varepsilon_{\rm LJ}$ and $\sigma_{\rm LJ}$), and is of the form

$$V_{\rm LJ} = 4\,\varepsilon_{\rm LJ}\left[\left(\frac{\sigma_{\rm LJ}}{r}\right)^{12} - \left(\frac{\sigma_{\rm LJ}}{r}\right)^{6}\right], \tag{24}$$

where $\sigma_{\rm LJ}$ is the intermolecular distance at which the potential is zero, and r is the intermolecular distance.

The Morse potential $V_{\rm M}$ has three adjustable parameters ($\varepsilon_{\rm M}$, $\sigma_{\rm M}$, and r_0), and is of the form [9]

$$V_{\rm M} = \varepsilon_{\rm M}\left\{\exp\left[-2\sigma_{\rm M}(r-r_0)\right] - 2\exp\left[-\sigma_{\rm M}(r-r_0)\right]\right\}, \tag{25}$$

where $\varepsilon_{\rm M}$ is the well-depth parameter, $\sigma_{\rm M}$ is a parameter which adjusts the steepness of the potential, and r_0 is the equilibrium intermolecular distance.

The BR potential has a more complicated form than the LJ and Morse potentials. It was developed specifically for the Xe-Pt(111) system, and is intended for MD simulations. The BR potential $V_{\rm BR}$ has nine adjustable parameters (A_1, α_1, c_6, h_s, r_1, A_g, W, α, and δ) with the following form [13; 172]:

$$V_{\rm BR} = \sum\left[u(r_i) + v(r_i')\right] + V(z_g^{\rm ave}), \tag{26}$$

where

$$u(r_i) \equiv A_1\exp(-\alpha_1 r_i), \tag{27}$$

and

$$v(r_i') \equiv -\frac{c_6\,G(r_i')}{r_i'^6}, \tag{28}$$

where A_1, α_1, and c_6 are adjustable parameters, r_i is the distance between the gas molecule and the $i^{\rm th}$ bulk molecule, and r_i' is centered a distance h_s above the bulk

molecule with

$$r_i'^2 \equiv (x_g - x_i)^2 + (y_g - y_i)^2 + (z_g - z_i - h_s)^2, \tag{29}$$

where $(x_i,\ y_i,\ z_i)$ is the position of the bulk molecule, the coordinates of the gas molecule are $(x_g,\ y_g,\ z_g)$, and h_s is an adjustable height parameter. $G(r)$ is a damping function defined as

$$G(r) \equiv \begin{cases} 1 & \text{for } r > r_1, \\ \exp\left[-\left(\dfrac{r_1}{r} - 1\right)^2\right] & \text{for } r \le r_1, \end{cases} \tag{30}$$

where r_1 is an adjustable parameter. The term $V(z_g^{\text{ave}})$ is defined as

$$V(z_g^{\text{ave}}) \equiv \frac{A_g\, W \exp\left(-\alpha z_g^{\text{ave}}\right)}{W + A_g \exp\left(-\alpha z_g^{\text{ave}}\right)}, \tag{31}$$

where A_g, W, and α are adjustable parameters, and z_g^{ave} is the height above the "local-average" surface z_{gs}^{ave},

$$z_g^{\text{ave}} \equiv z_g - z_{gs}^{\text{ave}}, \tag{32}$$

where z_{gs}^{ave} is a weighted average over the surface molecules,

$$z_{gs}^{\text{ave}} \equiv \frac{\sum_{\text{s}} z_i\, \phi(r_i)}{\sum \phi(r_i)}, \tag{33}$$

with the subscript s indicating that the summation in the numerator is performed only for the surface molecules. $\phi(r)$ is a weighting function given by

$$\phi(r) \equiv \exp\left(-\delta r^2\right), \tag{34}$$

where δ is an adjustable parameter.

2.4 Results

To verify that MKS may be utilized to simulate adsorption and scattering in DSMC simulations, it will be shown in this section that (1) not only is the integrity of CLL maintained, but its performance is actually improved, (2) initial adsorption probabilities S_0 compare favorably with experiment, and (3) coverage-dependent probabilities agree well with data.

2.4.1 Scattering.

The scattering properties of CLL are improved when incorporated into MKS. Figures 2 and 3 compare experimental data with MKS and CLL calculations for scattering angles and $E'_{\rm tr}$ [13]. The incident angle is 45° and the incident translational energy is 48.2 kJ mol^{-1}. The CLL and MKS results were sampled from 10^7 simulated particles. Only molecules scattered in-plane ($\pm 1°$) are reported, to match what was measured by experiment [143; 147; 148]. In Figure 2, the in-plane scattering angle is measured from the surface normal. The scattered intensity for MKS has a tighter distribution than CLL, and approaches experimental values. In Figure 3, $E'_{\rm tr}$ is the average total energy in that scattering direction. At higher angles, MKS approaches CLL, while at lower angles, MKS follows the upward trend seen from experiment. It is interesting to note that when the gas molecule collides with the surface, it may scatter such that $E'_{\rm tr} > E_{\rm tr}$. This phenomenon is termed super-elastic scattering, and describes the case where the gas molecule picks up thermal energy from the surface during the collision.

It would be preferable to compare scattering data at the same surface temperature used in Sections 2.4.2 and 2.4.3 (i.e., 95 K). However, there is little scattering data for the Xe-Pt(111) system in the literature. In Reference [13], scattering data were reported for Xe-Pt(111) at $T_s = 800$ K, which is much higher than $T_s = 95$ K. In

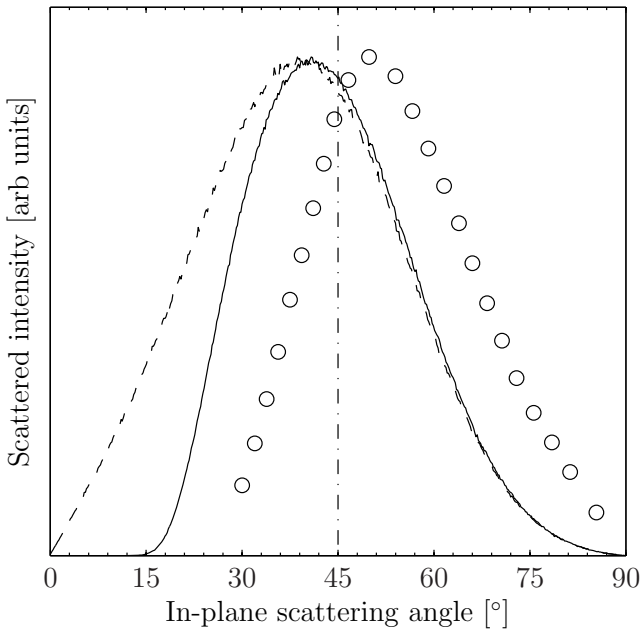

Figure 2. Scattered intensity versus in-plane scattering angle for Xe-Pt(111). Calculations from CLL and MKS are compared with experiment. The surface temperature is $T_s = 800$ K. The angle of incidence θ_i and the in-plane scattering angle are measured from the surface normal. The angle of incidence θ_i is 45° with an incident energy $E_{\rm tr} = 48.2$ kJ mol^{-1}. The vertical line indicates purely specular scattering. CLL and MKS simulations were performed with $\alpha_n = 0.74$, $\alpha_t = 0.60$, $\varepsilon_{\rm LJ} = 2.142$ kJ mol^{-1}, and $E_{\rm ads} = 25.9$ kJ mol^{-1}. —, MKS; – –, CLL; ∘, experimental data from [13], Figure 7.

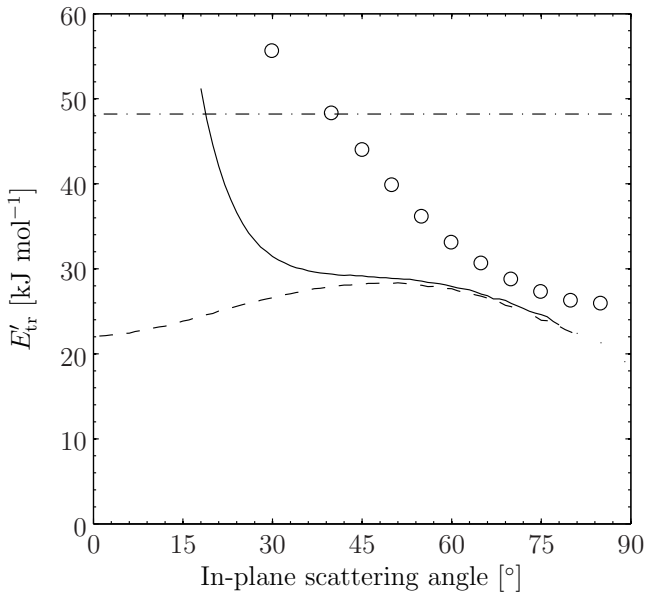

Figure 3. Final translational energy $E'_{\rm tr}$ versus in-plane scattering angle for Xe-Pt(111). Calculations from CLL and MKS are compared with experiment. The surface temperature is $T_s = 800$ K. The angle of incidence θ_i is 45°. The horizontal line represents the incident energy $E_{\rm tr} = 48.2$ kJ mol^{-1}. CLL and MKS simulations were performed with $\alpha_n = 0.74$, $\alpha_t = 0.60$, $\varepsilon_{\rm LJ} = 2.142$ kJ mol^{-1}, and $E_{\rm ads} = 25.9$ kJ mol^{-1}. —, MKS; – –, CLL; ∘, experimental data from [13], Figure 7.

spite of this deficiency, comparison with experiment at the elevated temperature still provides an opportunity to consider how MKS performs.

2.4.2 Initial Adsorption Probabilities.

Arumainayagam et al. reported experimental initial adsorption probabilities S_0 for the Xe-Pt(111) system using supersonic atomic beam techniques [9]. The surface temperature of Pt(111) was held at $T_s = 95$ K while the incident translational energy $E_{\rm tr}$ of the xenon atoms varied from 7 to 63 kJ mol^{-1} at incident angles θ_i from 0° to 60° with respect to the surface normal. At these incident energies, the radius parameter $\mathcal{R}$ is between 1.6 and 1.7 (2.52 Å $\leq R_{\rm eff} \leq$ 2.65 Å, $d_0 = 2.70$ Å, and $R_c = 1.56$ Å), indicating that this system falls under the thermal scattering regime and that MKS is applicable. S_0 was measured within an experimental error of ± 0.02, and the coverage θ noise level was about 0.01 ML.

MKS simulations are compared with data in Figure 4 [9]. Each point on the MKS curve is from a sample of 10^5 molecules impinging on the surface with incident normal and in-plane tangential velocities $c_n = c\cos\theta_i$ and $c_t = c\sin\theta_i$, respectively, where $c = \sqrt{2E_{\rm tr}/m}$ is the total incident velocity, and m is the gas molecule molar mass. Points were chosen at 11 different angles equally spaced from 0° to 90°, and 11 different specific energies equally spaced from 0 to 63 kJ mol^{-1}. For $n_m = 2.0$, all of the points fell onto a single curve. The values for α_n and α_t were chosen to best match experiment in Figure 6, and are both within the published ranges of $0.7 - 1.0$ and $0.6 - 0.8$, respectively [49]. The simulations were less sensitive to α_t than to α_n, indicating that the MKS method would perhaps need to be modified to handle larger surface corrugation; the PES for Xe-Pt(111) is relatively smooth. $\alpha_{n,\rm ad}$ and $\alpha_{t,\rm ad}$ were not specified, since the surface was assumed to be clean. The other parameters were taken from the literature [9]: $\varepsilon_{\rm LJ} = 2.142$ kJ mol^{-1}, and $E_{\rm ads} = 25.9$ kJ mol^{-1}, where $E_{\rm ads}$ is the molar energy of adsorption. The surface temperature was $T_s = 95$ K. The exponent n_m from $E_{\rm tr}\cos^{n_m}\theta_i$ is not based in theory, but has been found to place S_0 data points on a single curve. $n_m = 2.0$ was chosen in Figure 4 to highlight the MKS curve. In Figure 5, MKS calculations are compared with values obtained by Weaver et al. [172] from Morse and BR potentials, with $n_m = 1.8$, 10^5 simulated impinging molecules per point at 50 different angles equally spaced from 0° to 90°, and 50 different specific energies equally spaced from 0 to 63 kJ mol^{-1}, with the other parameters the same as in Figure 4. The BR and Morse potential parameters are listed in the caption to Figure 5. Admittedly, MKS does not recreate S_0 well, even though it will be shown in Figure 6 to match $S(\theta)$ much better. For the results in Figures 4 and 5, adsorption is occurring as a 2D gas.

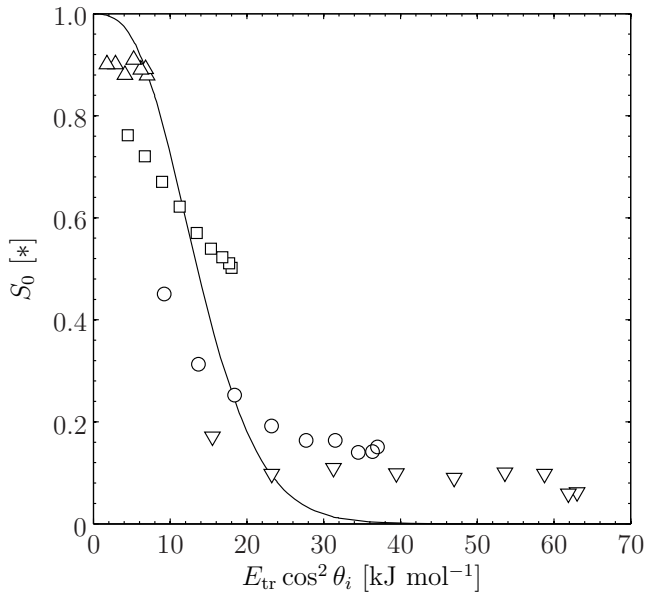

Figure 4. Initial adsorption probability S_0 versus modified energy $E_{\rm tr}\cos^2\theta_i$ for Xe-Pt(111). The surface temperature is $T_s = 95$ K. The curve is from MKS simulations with $\alpha_n = 0.74$, $\alpha_t = 0.60$, $\varepsilon_{\rm LJ} = 2.142$ kJ mol^{-1}, and $E_{\rm ads} = 25.9$ kJ mol^{-1}. —, MKS; $\triangle$, 7 kJ mol^{-1} (exp); $\square$, 18 kJ mol^{-1} (exp); $\circ$, 37 kJ mol^{-1} (exp); $\triangledown$, 63 kJ mol^{-1} (exp). Experimental data are from [9], Figure 4.

2.4.3 Coverage-Dependent Adsorption Probabilities.

The adsorption probability $S(\theta)$ is also a function of coverage. Adsorption probability versus coverage for five different initial conditions is shown in Figure 6; the data are from [10] with uncertainties of ± 3 K for T_s, and ± 0.03 for $S(\theta)$. The parameters are the same as those from Figure 4. In addition, $\alpha_{n,\rm ad} = 0.89$ and $\alpha_{t,\rm ad} = 0.60$ were chosen in order to best fit MKS results to experiment. $S(\theta)$ was not sensitive to the choice of $\alpha_{t,\rm ad}$. $S(\theta)$ increases with coverage, requiring $\alpha_{n,\rm ad} > \alpha_n$. This finding is consistent with observations made in [10] where the adsorption probability on covered surfaces was greater than the adsorption probability on a clean surface. The results are a 2D gas where $\theta < 0.02$, and a 2D solid combined with a 2D gas otherwise.

A sensitivity analysis was performed to determine the optimal value for the post-collisional energy threshold value, and it was verified in this work that $2\varepsilon_{\rm LJ}$ provides satisfactory results. Yamanishi et al. claim that when a gas molecule scatters off of

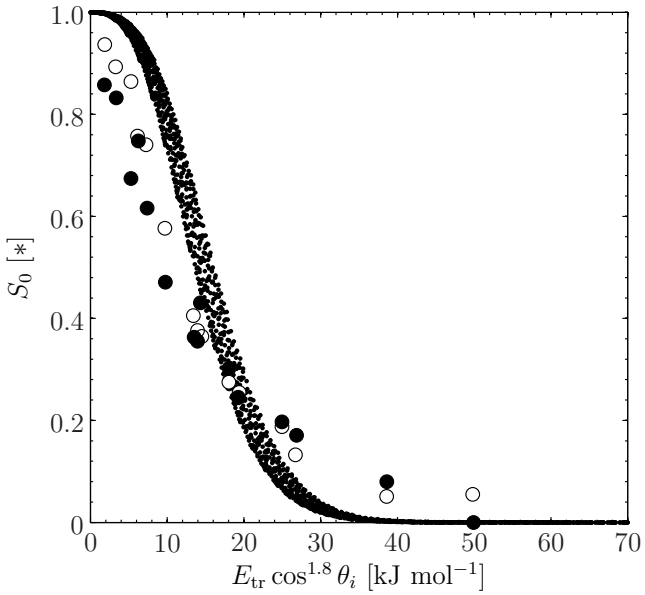

Figure 5. Initial adsorption probability S_0 versus modified energy $E_{\rm tr}\cos^{1.8}\theta_i$ for Xe-Pt(111). The surface temperature is $T_s = 95$ K. The curve is from MKS simulations with $\alpha_n = 0.74$, $\alpha_t = 0.60$, $\varepsilon_{\rm LJ} = 2.142$ kJ mol^{-1}, and $E_{\rm ads} = 25.9$ kJ mol^{-1}. •, MKS; ●, BR; ○, Morse. Morse potential parameters are [172]: $\varepsilon_{\rm M} = 2.628$ kJ mol^{-1}, $\sigma_{\rm M} = 1.05\,$Å^{-1}, and $r_0 = 3.20\,$Å. BR parameters are [13]: $A_g = 3.084 \times 10^6$ kJ mol^{-1}, $\alpha = 4.25\,$Å^{-1}, $W = 96$ kJ mol^{-1}, $A_1 = 5.718 \times 10^{11}$ kJ mol^{-1}, $\alpha_1 = 9.00\,$Å^{-1}, $\delta = 0.22\,$Å^{-2}, $c_6 = 7.981 \times 10^3$ kJ Å^6 mol^{-1}, $h_s = 1.83\,$Å, and $r_1 = 6.8247\,$Å [14]. BR and Morse calculations are from [172], Figure 3.

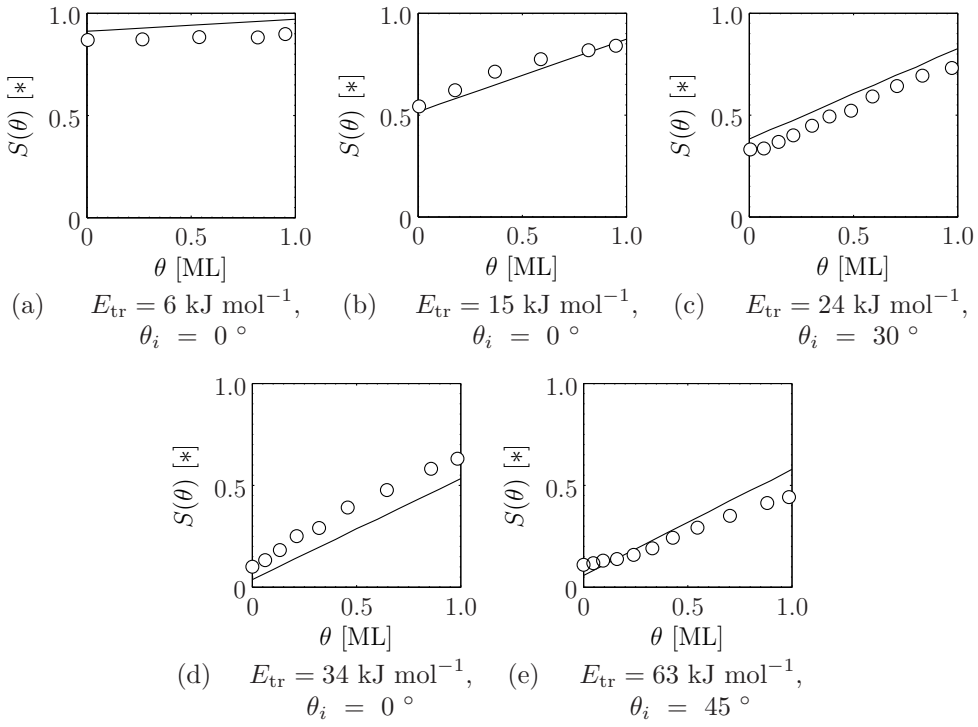

(a) $E_{\rm tr} = 6$ kJ mol^{-1}, $\theta_i = 0\,^\circ$ (b) $E_{\rm tr} = 15$ kJ mol^{-1}, $\theta_i = 0\,^\circ$ (c) $E_{\rm tr} = 24$ kJ mol^{-1}, $\theta_i = 30\,^\circ$

(d) $E_{\rm tr} = 34$ kJ mol^{-1}, $\theta_i = 0\,^\circ$ (e) $E_{\rm tr} = 63$ kJ mol^{-1}, $\theta_i = 45\,^\circ$

Figure 6. Adsorption probability $S(\theta)$ versus coverage θ for Xe-Pt(111) at different incident kinetic energies and angles. The surface temperature is $T_s = 95$ K. θ is measured in monolayers. MKS simulations were performed with $\alpha_n = 0.74$, $\alpha_t = 0.60$, $\alpha_{n,\rm ad} = 0.89$, $\alpha_{t,\rm ad} = 0.60$, $\varepsilon_{\rm LJ} = 2.142$ kJ mol^{-1}, and $E_{\rm ads} = 25.9$ kJ mol^{-1}. —, MKS; ∘, experimental data is from [10], Figure 1.

a surface, it has an average potential energy of $2\varepsilon_{\mathrm{LJ}}$, and so $2\varepsilon_{\mathrm{LJ}}$ was the threshold value that they chose [180]. For the MKS method, values higher than $2\varepsilon_{\mathrm{LJ}}$ were discovered to improve post-collisional energies and scattering angles when compared with experiment, but caused the adsorption probabilities to deviate even more from experimental values. For a value of $5\varepsilon_{\mathrm{LJ}}$, calculated post-collisional energies and scattering angles agreed well with experiment, while adsorption probabilities increased dramatically and were too large compared with experimental values. On the other hand, threshold values less than $2\varepsilon_{\mathrm{LJ}}$ did not improve any of the MKS results.

2.5 Physisorption Summary

A new method, the Modified Kisliuk with Scattering method, has successfully been developed for calculating adsorption probabilities and scattering properties in Direct Simulation Monte Carlo applications. The Modified Kisliuk with Scattering method incorporates a commonly-employed scattering kernel, the Cercignani-Lampis-Lord kernel, with the underlying assumptions of an existing adsorption model, the Modified Kisliuk model. The results show that, for the Xe-Pt(111) system, the new method was not only able to reproduce adsorption probabilities as a function of coverage, but it also improved the scattering properties of the Cercignani-Lampis-Lord kernel.

This work provides two significant contributions to the Cercignani-Lampis-Lord kernel. First, the kernel was applied to scattering off of an adlayer with favorable results. Previously, work with this kernel has been confined to the gas scattering off of the primary surface. This is the first time that gas-adlayer interactions have been modeled with the Cercignani-Lampis-Lord kernel. Second, optimal values for the accommodation coefficients were found by comparing results with experiment. The Modified Kisliuk with Scattering method thus provides an additional method for

determining appropriate accommodation coefficients.

Direct Simulation Monte Carlo techniques have now been shown to be capable of simulating surface effects, accomplished by successfully modeling adsorption and scattering for a physisorptive system. The next step, examined in Chapter III, will be to demonstrate that desorption in a chemisorptive system can also be modeled for Direct Simulation Monte Carlo.

III. Chemisorption

Chemisorption is much more complex than physisorption, and will therefore require different modeling methods than those presented in Chapter II. In addition, Chapter II was concerned with adsorption, whereas desorption will now be examined, the microscopically inverse process of adsorption. However, desorption is more complicated than adsorption for at least two reasons. First, the timing of desorption events must be determined accurately for a temporal simulation. Adsorption events simply occur when a gas molecule impinges the surface, and in a DSMC code, the positions and velocities of all the gas molecules are known and tracked. Therefore, the timing of adsorption events is not an issue. However, determining when an admolecule will (statistically) attain a sufficiently high enough energy to desorb, obtained from the surface thermal energy, is not trivial. Second, there are many desorption pathways for the same adsorbate. As discussed in Chapter I, desorption may be caused by surface thermal energy (LH), strong EM fields (FID), atom/molecule (ER), ion (IID), photon (PID), or electron (ESD) surface impact, and each of these pathways involves separate physical phenomena.

Desorption induced by surface thermal energy (LH) is thought to be a significant contributor to hydrogen-gas contamination in magnetron devices, therefore that pathway is investigated here for the relevant H_2-Cu(100) system (Section 3.1) in the following manner. Each desorbing molecule is modeled with the CT method (Section 3.3) as it is influenced by a 6D PES (Section 3.2). Initial conditions are assigned at the average TS locations (Section 3.6) according to a truncated Maxwell-Boltzmann (MB) distribution (Section 3.7). Then, the molecule is simulated forwards and backwards in time according to Keck's method (Section 3.5) to determine if that specific trajectory represents a valid desorption event. Since simulations are performed at the molecular scale, all of the relevant equations are non-dimensionalized

(Section 3.4). The timing of desorption events is determined via a Poisson process given a desorption rate (Section 3.8). Outputs of this method include the desorption angle, the translational energy, and the internal energies of the desorbing H_2 molecule (Section 3.9).

This work is a significant step forward for at least seven reasons. First, desorption modeling has not been available in DSMC applications until now. Desorption has been ignored in the DSMC community due to its complexity. The methods presented here can be directly applied to DSMC applications as a desorption boundary condition. Second, the timing of desorption events can now be coupled with CT simulations to model temporal desorption, a necessary requirement for system-level desorption simulations. Third, a non-dimensionalization scheme is developed for use with the CT method. Not a single non-dimensionalization scheme was found in the literature. Fourth, this work considers all of the contributing TS locations and weights them accordingly. Previous work only considered one TS location when implementing Keck's method. Fifth, a truncated MB distribution is developed (with its accompanying accept-reject form) to determine initial conditions at the TS locations. Sixth, state-resolved average translational energies are accurately modeled without the need for resource-intensive Gaussian Weighting (GW). Finally, the absorption energy barrier is shown to significantly contribute to the translational energy of desorbing molecules, but has little effect on their rotational and vibrational energies.

3.1 H_2-Cu(100) System

H_2-Cu is the simplest chemisorption desorption system to model [126], and the most thoroughly studied example of activated adsorption [114]. It is a fully-activated system, with activation barriers ranging from 0.5 to 1.0 eV [11; 126]. The strength of these barriers ensures that there is virtually no desorption (adsorption) on H_2-Cu

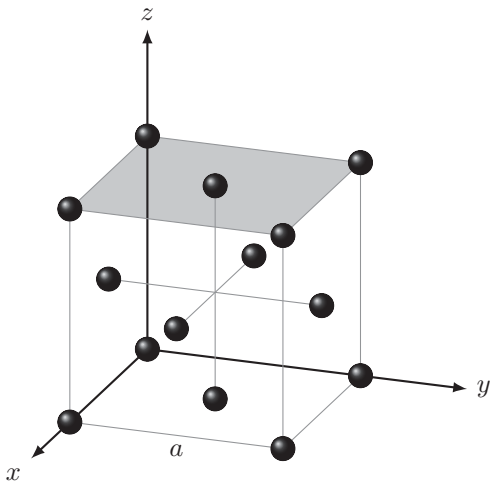

Figure 7. The unit cube for an FCC crystal structure. The lattice parameter a is defined as the average equilibrium length of the unit cube. The top face is highlighted to show the (100) surface.

at room temperature [5]. Since these average barriers have been shown to be only weakly dependent on surface coverage [166], the assumption that desorption events occur independently will be asserted here. This assumption equivalently describes a system in which desorption events are dependent upon one another, but where there is (almost) zero surface coverage.

When describing the surface of a crystal, it is important to identify how the crystal is cut in reference to the unit cube. Copper exhibits a face-centered cubic (FCC) crystalline structure, shown in Figure 7 as a unit cube. Copper atoms are placed at each corner of the cube and at the center of each of the six faces. As a brief introduction to the nomenclature, the (111) surface is found by cutting the unit cube parallel to the plane defined by the vector $\langle x, y, z\rangle = \langle 1, 1, 1\rangle$ and passing through the points $(x, y, z) = (a, 0, 0)$, $(0, a, 0)$, and $(0, 0, a)$, where a is the lattice parameter, or the average equilibrium length of the unit cube. Similarly, the (100) face (see Figure 7) is parallel to the plane defined by the vector $\langle 1, 0, 0\rangle$ and the point $(1, 0, 0)$. Note that since all six faces of an FCC crystal are identical, the (100), (010), and (001) surfaces are equivalent.

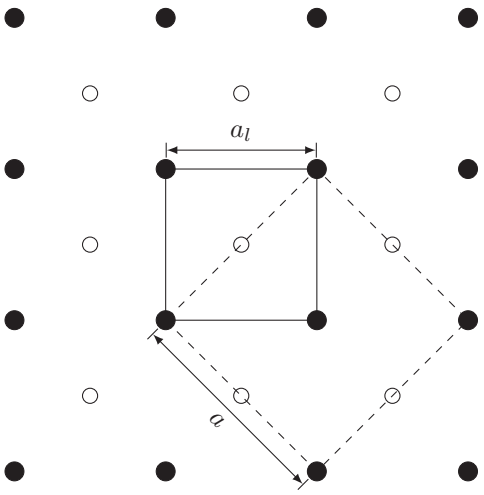

Figure 8. A comparison of the unit cube and cuboid on the Cu(100) surface. Filled circles represent the copper atoms in the top layer, while empty circles represent the layer of copper atoms immediately below the surface layer. The unit cube from Figure 7 is shown with dashed lines, including the typcial lattice parameter a. However, the smaller unit cuboid enclosed within the solid lines, with its corresponding distance a_l, is the unit cell to which reference is made in this work.

The unit surface cell utilized in this work, shown in Figure 8, differs slightly from the unit cube defined in Figure 7. The unit cell is a rectangular cuboid, the smallest repeating unit on the (100) FCC surface. By inspection, the length a_l is calculated from the relation $a_l = a/\sqrt{2}$. The experimental value a for copper is $a = 3.609$ Å [174], so that $a_l = 2.552$ Å.[1]

3.2 Potential Energy Surface (PES)

The interaction between a molecule and a surface is described by the PES, from which one can calculate the relevant forces. Then, with appropriate initial conditions, the molecule's position and velocity can also be determined. Diatomic hydrogen has six degrees of freedom, and therefore a 6D PES is required for a full description of the molecular motion [44; 45].

Wiesenekker et al. [174] developed a 6D PES to describe the molecule-surface

[1]In units of the Bohr radius a_0, $a = 6.820\ a_0$ and $a_l = 4.822\ a_0$.

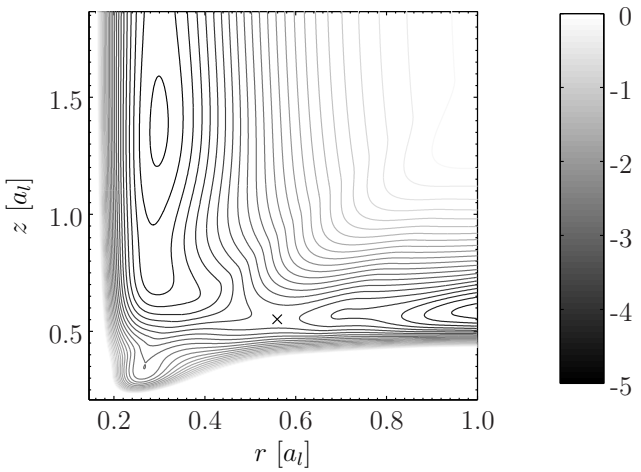

Figure 9. An example 2D slice of the full PES. Taken at $x = a_l$, $y = a_l/2$, $\theta = 90°$, and $\phi = 90°$, copresponding to the case where hydrogen atoms are adsorbed on top of adjacent copper atoms, and desorbed as H_2 above a bridge site. The TS is located at the saddle point, indicated by an $\times$. The contours represent potential energy in units of eV. The reaction path would follow the path of lowest potential energy from the adsorbed state ($r = a_l$) to the desorbed state ($z = 1.87\ a_l$), passing through the TS. Note that the H_2-Cu(100) system exhibits early (late) barriers to desorption (adsorption) [139].

interaction for the H_2-Cu(100) system. The PES is based on slab calculations with the GGA in DFT with an RS assumption (bulk atoms are frozen in time and space), and is expressed as an analytical fit, allowing for a high degree of flexibility, and bypassing the need for computationally intensive on-the-fly DFT calculations. The full 6D PES is achieved by splicing together eight 2D PES slices [175; 176], which are individually anchored to experimental results. This 6D PES was specifically tailored to be accurate in the region between the gas phase and the TS (the location or zone where the individual adatoms combine into a molecule). Within the TS, the PES is fairly accurate, and between the TS and the surface, the PES is inaccurate. However, since results will focus on desorption properties (with initial conditions specified at the TS), the region where the PES is inaccurate will not play a large enough role to be a concern.

The 6D Wiesenekker PES is constructed in two stages. First, eight 2D PES slices are calculated as functions of r (interatomic bond length) and z (shortest distance

from the center of mass of the molecule to the surface) for various molecular orientations and desorption paths. The eight 2D PESs are then combined into a 6D PES by solving sets of linear equations. The details of this process are provided below for the convenience of the reader.

Four of the eight 2D PES slices (V_{bh90}, V_{bt90}, V_{hb90}, and V_{tb90}) are created by summing the contributions from a two-body potential V_2 and a three-body potential V_3,

$$V(r,z) = V_2(r,z) + V_3(r,z), \tag{35}$$

where the two- and three-body potentials are constructed similarly,

$$V_2(r,z) = \begin{cases} V_2^A(r,z), & \zeta < \zeta_0 - \Delta\zeta, \\ f_c(\zeta)V_2^A(r,z) + [1 - f_c(\zeta)]V_2^B(r,z), & \zeta_0 - \Delta\zeta \leq \zeta \leq \zeta_0 + \Delta\zeta, \\ V_2^B(r,z), & \zeta > \zeta_0 + \Delta\zeta, \end{cases} \tag{36}$$

and

$$V_3(r,z) = \begin{cases} V_3^A(r,z), & \zeta < \zeta_0 - \Delta\zeta, \\ f_c(\zeta)V_3^A(r,z) + [1 - f_c(\zeta)]V_3^B(r,z), & \zeta_0 - \Delta\zeta \leq \zeta \leq \zeta_0 + \Delta\zeta, \\ V_3^B(r,z), & \zeta > \zeta_0 + \Delta\zeta, \end{cases} \tag{37}$$

and $f_c(\zeta)$ is the switching function, defined by

$$f_c(\zeta) = \frac{1 + \cos\chi}{2}, \tag{38}$$

with

$$\chi = \frac{\pi}{2}\left[\frac{\zeta - (\zeta_0 - \Delta\zeta)}{\Delta\zeta}\right], \tag{39}$$

and

$$\zeta = \tan^{-1}\left(\frac{z - z_{\text{ref}}}{r - r_{\text{ref}}}\right). \tag{40}$$

Values for the above parameters are given in Reference [174] as $z_{\text{ref}} = 18.3\,a_0$, $r_{\text{ref}} = 11.0\,a_0$, $\zeta_0 = 61.5°$, and $\Delta\zeta = 2.5°$. The two-body expressions V_2^A and V_2^B are superpositions of attractive (V_{att}) and repulsive (V_{rep}) potentials,

$$V_2^A(r, z) = V_{\text{att}}(r) + V_{\text{rep}}(z), \tag{41}$$

$$V_2^B(r, z) = 2V_{\text{att}}(z) + V_{\text{rep}}(r). \tag{42}$$

V_2^A represents the H_2 molecule as it desorbs, so that the molecule experiences an attractive force between the two hydrogen atoms but a repulsive interaction with the surface. On the other hand, V_2^B represents the two H atoms before they combine into an H_2 molecule, so that both an attractive interaction with the surface, and a repulsive interaction between the atoms, exist. The attractive potential is fit to a modified Rydberg form,

$$V_{\text{att}}(\rho) = -D_e\left(1.0 + a_1\rho_{\text{att}} + a_2\rho_{\text{att}}^2 + a_3\rho_{\text{att}}^3\right)\exp(-a_4\rho_{\text{att}}), \tag{43}$$

where $\rho_{\text{att}} = r - r_e$ in Equation (41), but $\rho_{\text{att}} = z - z_e$ in Equation (42), and the Pauli repulsion V_{rep} is expressed as

$$V_{\text{rep}}(\rho_{\text{rep}}) = a\,\exp(-b\rho_{\text{rep}}), \tag{44}$$

where $\rho_{\text{rep}} = r$ in Equation (41), $\rho_{\text{rep}} = z$ in Equation (42), and the remaining parameters are found in Tables II and III in Reference [174]. The actual fitting is contained within the three-body expressions V_3^A and V_3^B, which represent the energy differences between the GGA energy and the two-body potential, fitted with a least-

squares procedure in the following expressions,

$$V_3^A(r,z) = P(s_1,s_2)\left[1.0 - \tanh(\gamma_1 s_1)\right]\left[1.0 - \tanh(\gamma_2 s_2)\right], \tag{45}$$

$$V_3^B(r,z) = P(s_1,s_2)\left[1.0 - \tanh(\gamma_1 s_1)\right]\left[1.0 - \tanh(\gamma_2 s_2)\right], \tag{46}$$

where $P(s_1, s_2)$ is the analytical curve fit,

$$\begin{aligned} P(s_1,s_2) =& c_0 + c_1 s_1 + c_2 s_2 \\ &+ c_{11} s_1^2 + c_{12} s_1 s_2 + c_{22} s_2^2 \\ &+ c_{111} s_1^3 + c_{112} s_1^2 s_2 + c_{122} s_1 s_2^2 + c_{222} s_2^3 \\ &+ c_{1111} s_1^4 + c_{1112} s_1^3 s_2 + c_{1122} s_1^2 s_2^2 + c_{1222} s_1 s_2^3 + c_{2222} s_2^4 \\ &+ c_{11112} s_1^4 s_2 + c_{11122} s_1^3 s_2^2 + c_{11222} s_1^2 s_2^3 + c_{12222} s_1 s_2^4, \end{aligned} \tag{47}$$

with $s_1 = r - r_0$ and $s_2 = z - z_0$. Note that if $r < r_{3b}$, then $r = r_{3b}$. Likewise, if $z < z_{3b}$, then $z = z_{3b}$. All of the parameters for V_3^A and V_3^B are taken from Tables IV and V in Reference [174], respectively.

The remaining four 2D PES slices (V_{bh140}, V_{bt140}, V_{hb140}, and V_{tb140}) are also superpositions of two-body (V_2) and three-body (V_3) interactions,

$$V = V_2(r,z,\theta) + V_3(r,z). \tag{48}$$

The two-body potential V_2 is

$$V_2(r,z,\theta) = V_{\text{att}}(r) + V_{\text{rep}}(z,\theta), \tag{49}$$

where V_{att} is taken from Equation (43) with $\rho = r - r_e$ and the parameters from the column labeled H_2 in Table II, Reference [174]. The repulsive potential is dependent

upon θ,

$$V_{\text{rep}}(z,\theta) = \frac{a}{2}\left[\exp(-bz_1) + \exp(-bz_2)\right], \tag{50}$$

where z_1 and z_2 are the z-coordinates (height above the surface) of the individual atoms,

$$z_1 = z - \frac{r\cos\theta}{2}, \qquad\qquad z_2 = z + \frac{r\cos\theta}{2}, \tag{51}$$

and the parameters a and b are found in the column for Cu-H_2 interactions in Table III, Reference [174]. The three-body potential V_3^A is again calculated from Equations (45) and (47), with $s_1 = r - r_0$ and $s_2 = z - z_0$. If $r < r_{3b}$ then $r = r_{3b}$, and if $z < z_{3b}$ then $z = z_{3b}$ (parameters taken from Table VI in Reference [174]). V_3 is determined from,

$$V_3(r,z) = \begin{cases} V_3^A(r,z), & \xi < \xi_0 - \Delta\xi, \\ f_d(\xi)V_3^A(r,z), & \xi_0 - \Delta\xi \le \xi \le \xi_0 + \Delta\xi, \\ 0, & \xi > \xi_0 + \Delta\xi, \end{cases} \tag{52}$$

with the help of another switching function $f_d(\xi)$, similar to $f_c(\zeta)$, where

$$f_d(\xi) = \frac{1 + \cos\chi_2}{2}, \tag{53}$$

$$\chi_2 = \frac{\pi}{2}\left[\frac{\xi - (\xi_0 - \Delta\xi)}{\Delta\xi}\right], \tag{54}$$

and

$$\xi = \tan^{-1}\left(\frac{z - z_{\text{ref},2}}{r - r_{\text{ref},2}}\right). \tag{55}$$

Values for the above parameters are given as $z_{\text{ref},2} = 14.0\,a_0$, $r_{\text{ref},2} = 15.0\,a_0$, $\xi_0 = 46.15°$, and $\Delta\xi = 1.15°$ in Reference [174]. As a side note, there is an error in Figure 5a

in Wiesenekker et al. [174]. That plot does not represent calculations with the parameter z_{3b}, as it should. Figures 3a, 3b, 4a, 4b, 5a, and 5b in Wiesenekker et al. [174] can be recreated by plotting $V_{bh90}(r,z)$, $V_{bt90}(r,z)$, $V_{hb90}(r,z)$, $V_{tb90}(r,z)$, $V_{bh140}(r,z,\theta)$, and $V_{bt140}(r,z,\theta)$, respectively.

The 2D expansion coefficients are constructed from the various 2D PES slices. They are grouped according to whether desorption occurs over a bridge site,

$$V_{20b}(r,z,\theta) = \frac{V_{bh140}(r,z,\theta) + V_{bt140}(r,z,\theta) - V_{bh90}(r,z) - V_{bt90}(r,z)}{2\left[Y_2^0(\theta = 140.8^\circ) - Y_2^0(\theta = 90^\circ)\right]},$$

$$V_{00b}(r,z) = \frac{V_{bh90}(r,z) + V_{bt90}(r,z) - V_{20b}(r,z)Y_2^0(\theta = 90^\circ)}{2Y_0^0},$$

$$V_{2eb}(r,z) = \frac{V_{bh90}(r,z) - V_{bt90}(r,z)}{2Y_2^e(\theta = 90^\circ, \phi = 0^\circ)}, \tag{56}$$

a hollow site,

$$V_{20h}(r,z,\theta) = \frac{V_{hb140}(r,z,\theta) - V_{hb90}(r,z)}{Y_2^0(\theta = 140.8^\circ) - Y_2^0(\theta = 90^\circ)},$$

$$V_{00h}(r,z) = \frac{V_{hb90}(r,z) - V_{20h}(r,z)Y_2^0(\theta = 90^\circ)}{Y_0^0}, \tag{57}$$

or a top site,

$$V_{20t}(r,z,\theta) = \frac{V_{tb140}(r,z,\theta) - V_{tb90}(r,z)}{Y_2^0(\theta = 140.8^\circ) - Y_2^0(\theta = 90^\circ)}$$

$$V_{00t}(r,z) = \frac{V_{tb90}(r,z) - V_{20t}(r,z)Y_2^0(\theta = 90^\circ)}{Y_0^0}. \tag{58}$$

The 6D expansion coefficients are calculated as,

$$
\begin{aligned}
V_{0000}(r,z) &= \frac{\sqrt{A}}{4}\left[V_{00t}(r,z) + V_{00h}(r,z) + 2V_{00b}(r,z)\right], \\
V_{0010}(r,z) &= \frac{\sqrt{A}}{4}\left[V_{00t}(r,z) - V_{00h}(r,z)\right], \\
V_{0011}(r,z) &= \frac{\sqrt{A}}{8}\left[V_{00t}(r,z) + V_{00h}(r,z) - 2V_{00b}(r,z)\right], \\
V_{2000}(r,z,\theta) &= \frac{\sqrt{A}}{4}\left[V_{20t}(r,z,\theta) + V_{20h}(r,z,\theta) + 2V_{20b}(r,z,\theta)\right], \\
V_{2010}(r,z,\theta) &= \frac{\sqrt{A}}{4}\left[V_{20t}(r,z,\theta) - V_{20h}(r,z,\theta)\right], \\
V_{2011}(r,z,\theta) &= \frac{\sqrt{A}}{8}\left[V_{20t}(r,z,\theta) + V_{20h}(r,z,\theta) - 2V_{20b}(r,z,\theta)\right], \\
V_{2e10}(r,z) &= \frac{\sqrt{A}}{2}V_{2eb}(r,z),
\end{aligned}
\tag{59}
$$

where A is the area of the surface unit cell, and the spherical harmonics $Y_l^m(\theta,\phi)$ are defined for degree $l = 0$ and order $m = 0$,

$$
Y_0^0 = \frac{1}{2}\sqrt{\frac{1}{\pi}}, \tag{60}
$$

for degree $l = 2$,

$$
Y_2^0(\theta) = \sqrt{\frac{5}{16\pi}}\left(3\cos^2\theta - 1\right),
$$

$$
Y_2^2(\theta,\phi) = \sqrt{\frac{15}{32\pi}}\sin^2\theta\,\exp(2i\phi),
$$

$$
Y_2^{-2}(\theta,\phi) = \sqrt{\frac{15}{32\pi}}\sin^2\theta\,\exp(-2i\phi), \tag{61}
$$

and for a combination of Y_2^2 and Y_2^{-2} [174],

$$Y_2^e(\theta,\phi) = \sqrt{\frac{1}{2}}\left[Y_2^2(\theta,\phi) + Y_2^{-2}(\theta,\phi)\right],$$

$$= \sqrt{\frac{15}{16\pi}}\sin^2\theta\cos 2\phi, \tag{62}$$

where i is the imaginary number $i = \sqrt{-1}$.

Finally, the 6D potential $V_{6\mathrm{D}}$ is constructed as,

$$\begin{aligned} V_{6\mathrm{D}}(x,y,z,r,\theta,\phi) =& H_{00}(x,y)\,V_{0000}(r,z)\,Y_0^0 \\ &+ H_{00}(x,y)\,V_{2000}(r,z,\theta)\,Y_2^0(\theta) \\ &+ H_{10}(x,y)\,V_{0010}(r,z)\,Y_0^0 \\ &+ H_{10}(x,y)\,V_{2010}(r,z,\theta)\,Y_2^0(\theta) \\ &+ H_{11}(x,y)\,V_{0011}(r,z)\,Y_0^0 \\ &+ H_{11}(x,y)\,V_{2011}(r,z,\theta)\,Y_2^0(\theta) \\ &+ H_{B_1 10}(x,y)\,V_{2e10}(r,z)\,Y_2^e(\theta,\phi), \end{aligned} \tag{63}$$

where the plane-wave diffraction functions are defined as [86],

$$\begin{aligned} H_{00}(x,y) &= \sqrt{\frac{1}{A}}, \\ H_{10}(x,y) &= \sqrt{\frac{1}{A}}\left[\cos Gx + \cos Gy\right], \\ H_{11}(x,y) &= 2\sqrt{\frac{1}{A}}\left[\cos Gx \times \cos Gy\right], \\ H_{B_1 10}(x,y) &= \sqrt{\frac{1}{A}}\left[\cos Gx - \cos Gy\right], \\ G &= \frac{2\pi}{a_l}. \end{aligned} \tag{64}$$

Note that in Equation (63), V_{6D} is not a function of A.

3.3 Classical Trajectory (CT) Formulation

The trajectories of desorbing molecules are modeled classically (CT) with the aid of Hamiltonian mechanics. The equations of motion are derived for a linear rotor molecule, and energies are identified as translational, rotational, or vibrational. Quantum effects are ignored, a necessary assumption for engineering applications. Otherwise, computational times would be prohibitively long for large-scale simulations.

The kinetic energy $\mathcal{T}$ of a linear rotor molecule of (total) mass M and reduced mass μ is formed by taking the sum of two components: (1) the motion of the center of mass about the origin, and (2) the motion of the atoms about the center of mass. In mathematical terms [164:318, 330],

$$\mathcal{T} = \frac{1}{2}M\left(\dot{x}^2 + \dot{y}^2 + \dot{z}^2\right) + \frac{1}{2}\mu\left(\dot{r}^2 + r^2\dot{\theta}^2 + r^2\dot{\phi}^2\sin^2\theta\right), \tag{65}$$

where $(x,\, y,\, z)$ is the location of the center of mass in the Cartesian reference frame, $(r,\, \theta,\, \phi)$ is the location of the two atoms in spherical coordinates with respect to the center of mass (r is the interatomic distance, θ is the elevation, and ϕ is the azimuth), and the dot notation indicates a derivative with respect to time t (see Section 3.6.1 for a further explanation of these coordinates). There are six degrees of freedom since the molecule has two atoms. The second term in Equation (65) can be derived by noting that for a single particle (mass m) described by spherical coordinates, its velocity is $\boldsymbol{v} = \dot{r}\,\hat{\boldsymbol{r}} + r\dot{\theta}\,\hat{\boldsymbol{\theta}} + r\dot{\phi}\sin\theta\,\hat{\boldsymbol{\phi}}$ ($\hat{\boldsymbol{r}}$, $\hat{\boldsymbol{\theta}}$, and $\hat{\boldsymbol{\phi}}$ are the unit-vectors in the r-, θ-, and ϕ-directions, respectively), its kinetic energy is $\boldsymbol{v}\cdot\boldsymbol{v}\,m/2$, and the linear rotor system is obtained by replacing m with μ. Note that for a homonuclear system of

mass m, $\mathcal{T}$ is only comprised of the motion of the center of mass about the origin, so that

$$\mathcal{T} = \frac{1}{2} m \left(\dot{x}^2 + \dot{y}^2 + \dot{z}^2 \right). \tag{66}$$

The Lagrangian $\mathcal{L} = \mathcal{T} - V$, in terms of the generalized coordinates x, y, z, r, θ, and ϕ, and the generalized velocities $\dot{x}$, $\dot{y}$, $\dot{z}$, $\dot{r}$, $\dot{\theta}$, and $\dot{\phi}$, is written as

$$\mathcal{L} = \frac{1}{2} M \left(\dot{x}^2 + \dot{y}^2 + \dot{z}^2 \right) + \frac{1}{2} \mu \left(\dot{r}^2 + r^2 \dot{\theta}^2 + r^2 \dot{\phi}^2 \sin^2 \theta \right) - V, \tag{67}$$

where V is the potential energy of the PES. The generalized momenta are then calculated from

$$p_i = \frac{\partial \mathcal{L}}{\partial \dot{q}_i}, \tag{68}$$

where p_i and $\dot{q}_i$ are the generalized momenta and generalized velocities, respectively, so that

$$p_x = \frac{\partial \mathcal{L}}{\partial \dot{x}} = M\dot{x}, \qquad p_r = \frac{\partial \mathcal{L}}{\partial \dot{r}} = \mu \dot{r},$$

$$p_y = \frac{\partial \mathcal{L}}{\partial \dot{y}} = M\dot{y}, \qquad p_\theta = \frac{\partial \mathcal{L}}{\partial \dot{\theta}} = \mu r^2 \dot{\theta},$$

$$p_z = \frac{\partial \mathcal{L}}{\partial \dot{z}} = M\dot{z}, \qquad p_\phi = \frac{\partial \mathcal{L}}{\partial \dot{\phi}} = \mu r^2 \dot{\phi} \sin^2 \theta. \tag{69}$$

The generalized velocities can then be expressed as $\dot{x} = p_x/M$, $\dot{y} = p_y/M$, $\dot{z} = p_z/M$,

$\dot{r} = p_r/\mu$, $\dot{\theta} = p_\theta/(\mu r^2)$, and $\dot{\phi} = p_\phi/(\mu r^2 \sin^2\theta)$. Thus, $\mathcal{T}$ can be rewritten,

$$\mathcal{T} = \frac{p_x^2 + p_y^2 + p_z^2}{2M} + \frac{p_r^2}{2\mu} + \frac{p_\theta^2}{2\mu r^2} + \frac{p_\phi^2}{2\mu r^2 \sin^2\theta}$$

$$= \frac{p_x^2 + p_y^2 + p_z^2}{2M} + \frac{p_r^2}{2\mu} + \frac{\mathcal{J}^2}{2I}, \tag{70}$$

where $I = \mu r^2$ is the reduced moment of inertia, and the rotational angular momentum $\mathcal{J}$ is defined by

$$\mathcal{J}^2 = p_\theta^2 + \frac{p_\phi^2}{\sin^2\theta}. \tag{71}$$

The Hamiltonian $\mathcal{H}$ (or total energy) can now be calculated from the Legendre transformation of $\mathcal{L}$ [131],

$$\mathcal{H} = \sum_i p_i \dot{q}_i - \mathcal{L},$$

$$= p_x\dot{x} + p_y\dot{y} + p_z\dot{z} + p_r\dot{r} + p_\theta\dot{\theta} + p_\phi\dot{\phi} - (\mathcal{T} - V),$$

$$= \frac{p_x^2 + p_y^2 + p_z^2}{M} + \frac{p_r^2}{\mu} + \frac{p_\theta^2}{\mu r^2} + \frac{p_\phi^2}{\mu r^2 \sin^2\theta} - \mathcal{T} + V,$$

$$= 2\mathcal{T} - \mathcal{T} + V,$$

$$= \mathcal{T} + V,$$

$$= \frac{p_x^2 + p_y^2 + p_z^2}{2M} + \frac{p_r^2}{2\mu} + \frac{\mathcal{J}^2}{2I} + V. \tag{72}$$

Equation (72) could have also been obtained from the knowledge that since the molecule is acting under a conservative force (i.e. a closed system), $\mathcal{H} = \mathcal{T} + V$.

The rotational angular momentum $\mathcal{J}$ from Equation (71) is

$$\mathcal{J}^2 = p_\theta^2 + \frac{p_\phi^2}{\sin^2\theta}. \tag{71}$$

From the Schrödinger equation for a rigid rotor, we have that $\mathcal{J}^2 = J(J+1)\hbar^2$. Thus the rotational number J is

$$J = -\frac{1}{2} + \sqrt{\frac{\mathcal{J}^2}{\hbar^2} + \frac{1}{4}}, \tag{73}$$

where $\hbar = h/(2\pi)$ is the reduced Planck constant, and h is the Planck constant. Note that J must be calculated with the dimensional value of $\mathcal{J}$.

The vibrational number n_v is calculated from the vibrational term of the Hamiltonian $H_v = p_r^2/(2\mu)$ in Equation (72),

$$n_v = \frac{H_v}{h\nu} - \frac{1}{2}, \tag{74}$$

where ν is the vibrational frequency. The value of ν for H_2 in the gas phase is taken here to be $\nu = 1.242 \times 10^{14}$ cycles per second (see Table 1 in Reference [131]).

Hamilton's equations then uniquely describe the time evolution of the molecule,

$$\dot{q}_i = \frac{\partial \mathcal{H}}{\partial p_i}, \qquad\qquad \dot{p}_i = -\frac{\partial \mathcal{H}}{\partial q_i}, \tag{75}$$

so that

$$\dot{x} = \frac{\partial \mathcal{H}}{\partial p_x} = \frac{p_x}{M}, \qquad \dot{r} = \frac{\partial \mathcal{H}}{\partial p_r} = \frac{p_r}{\mu},$$

$$\dot{y} = \frac{\partial \mathcal{H}}{\partial p_y} = \frac{p_y}{M}, \qquad \dot{\theta} = \frac{\partial \mathcal{H}}{\partial p_\theta} = \frac{p_\theta}{I},$$

$$\dot{z} = \frac{\partial \mathcal{H}}{\partial p_z} = \frac{p_z}{M}, \qquad \dot{\phi} = \frac{\partial \mathcal{H}}{\partial p_\phi} = \frac{p_\phi}{I \sin^2 \theta}, \tag{76}$$

and

$$\dot{p}_x = -\frac{\partial \mathcal{H}}{\partial x} = -\frac{\partial V}{\partial x}, \qquad \dot{p}_r = -\frac{\partial \mathcal{H}}{\partial r} = \frac{p_\theta^2}{\mu r^3} + \frac{p_\phi^2}{\mu r^3 \sin^2 \theta} - \frac{\partial V}{\partial r},$$

$$\dot{p}_y = -\frac{\partial \mathcal{H}}{\partial y} = -\frac{\partial V}{\partial y}, \qquad \dot{p}_\theta = -\frac{\partial \mathcal{H}}{\partial \theta} = \frac{p_\phi^2 \cos \theta}{\mu r^2 \sin^3 \theta} - \frac{\partial V}{\partial \theta},$$

$$\dot{p}_z = -\frac{\partial \mathcal{H}}{\partial z} = -\frac{\partial V}{\partial z}, \qquad \dot{p}_\phi = -\frac{\partial \mathcal{H}}{\partial \phi} = -\frac{\partial V}{\partial \phi}. \tag{77}$$

3.4 Non-Dimensionalization

Since simulations are conducted on the molecular scale, equations are non-dimensionalized to avoid unnecessary numerical errors. The non-dimensional parameters reported here are not available elsewhere in the literature. Therefore, this formulation is novel and would improve the accuracy of current CT implementations if employed.

Non-dimensionalization is achieved with the aid of the mass of the molecule M, the reduced mass of the molecule μ, the length of the surface unit cell a_l, the most-probable speed of a gas-phase molecule under equilibrium conditions $u_{\mathrm{mp}} = \sqrt{2kT_s/M} = \sqrt{2R_{\mathrm{sp}}T_s}$, a characteristic energy kT_s, the most probable time that

it takes one gas-phase molecule under equilibrium conditions to cross the unit cell $t_{\mathrm{mp}} = a_l/u_{\mathrm{mp}}$, two different characteristic linear momenta (Mu_{mp} and $\mu\, u_{\mathrm{mp}}$), and one characteristic angular momentum $a_l\, \mu\, u_{\mathrm{mp}}$. Here, k is the Boltzmann constant, T_s is the temperature of the surface, and $R_{\mathrm{sp}} = k/M$ is the specific gas constant. The non-dimensional parameters (denoted by an asterisk superscript) are

$$
\begin{aligned}
x^* &= \frac{x}{a_l}, & y^* &= \frac{y}{a_l}, & z^* &= \frac{z}{a_l}, \\
r^* &= \frac{r}{a_l}, & \theta^* &= \theta, & \phi^* &= \phi, \\
p_x^* &= \frac{p_x}{Mu_{\mathrm{mp}}}, & p_y^* &= \frac{p_y}{Mu_{\mathrm{mp}}}, & p_z^* &= \frac{p_z}{Mu_{\mathrm{mp}}}, \\
p_r^* &= \frac{p_r}{\mu\, u_{\mathrm{mp}}}, & p_\theta^* &= \frac{p_\theta}{a_l\, \mu\, u_{\mathrm{mp}}}, & p_\phi^* &= \frac{p_\phi}{a_l\, \mu\, u_{\mathrm{mp}}}, \\
V^* &= \frac{V}{kT_s}, & \mathcal{H}^* &= \frac{\mathcal{H}}{kT_s}, & \mathcal{J}^* &= \frac{\mathcal{J}}{a_l\, \mu\, u_{\mathrm{mp}}}, \\
& & t^* &= \frac{t}{t_{\mathrm{mp}}}.
\end{aligned}
\tag{78}
$$

Note that even though θ and ϕ are already non-dimensionalized (radians), they are included for completeness.

With these parameters, the non-dimensionalized Hamiltonian $\mathcal{H}^*$ is

$$
\mathcal{H}^* = p_x^{*2} + p_y^{*2} + p_z^{*2} + \frac{\mu}{M} p_r^{*2} + \frac{\mu}{M} \frac{\mathcal{J}^{*2}}{r^{*2}} + V^*, \tag{79}
$$

where the non-dimensionalized rotational angular momentum $\mathcal{J}^*$ is

$$\mathcal{J}^{*2} = p_\theta^{*2} + \frac{p_\phi^{*2}}{\sin^2\theta^*}, \tag{80}$$

and the non-dimensionalized Hamilton's equations of motion are

$$\begin{aligned} \dot{x}^* &= p_x^*, & \dot{r}^* &= p_r^*, \\ \dot{y}^* &= p_y^*, & \dot{\theta}^* &= \frac{p_\theta^*}{r^{*2}}, \\ \dot{z}^* &= p_z^*, & \dot{\phi}^* &= \frac{p_\phi^*}{r^{*2}\sin^2\theta^*}, \end{aligned} \tag{81}$$

and

$$\begin{aligned} \dot{p}_x^* &= -\frac{1}{2}\frac{dV^*}{dx^*}, & \dot{p}_r^* &= \frac{p_\theta^{*2}}{r^{*3}} + \frac{p_\phi^{*2}}{r^{*3}\sin^2\theta^*} - \frac{1}{2}\frac{M}{\mu}\frac{dV^*}{dr^*}, \\ \dot{p}_y^* &= -\frac{1}{2}\frac{dV^*}{dy^*}, & \dot{p}_\theta^* &= \frac{p_\phi^{*2}\cos\theta^*}{r^{*2}\sin^3\theta^*} - \frac{1}{2}\frac{M}{\mu}\frac{dV^*}{d\theta^*}, \\ \dot{p}_z^* &= -\frac{1}{2}\frac{dV^*}{dz^*}, & \dot{p}_\phi^* &= -\frac{1}{2}\frac{M}{\mu}\frac{dV^*}{d\phi^*}, \end{aligned} \tag{82}$$

where the dot notation indicates a derivative with respect to the non-dimensionalized

time t^*, and

$$\dot{x}^* = \frac{\dot{x}}{u_{\mathrm{mp}}}, \qquad \dot{y}^* = \frac{\dot{y}}{u_{\mathrm{mp}}}, \qquad \dot{z}^* = \frac{\dot{z}}{u_{\mathrm{mp}}},$$

$$\dot{r}^* = \frac{\dot{r}}{u_{\mathrm{mp}}}, \qquad \dot{\theta}^* = \dot{\theta}\, t_{\mathrm{mp}}, \qquad \dot{\phi}^* = \dot{\phi}\, t_{\mathrm{mp}}, \tag{83}$$

and

$$\dot{p}_x^* = \frac{t_{\mathrm{mp}}}{M u_{\mathrm{mp}}}\, \dot{p}_x, \qquad \dot{p}_y^* = \frac{t_{\mathrm{mp}}}{M u_{\mathrm{mp}}}\, \dot{p}_y, \qquad \dot{p}_z^* = \frac{t_{\mathrm{mp}}}{M u_{\mathrm{mp}}}\, \dot{p}_z,$$

$$\dot{p}_r^* = \frac{t_{\mathrm{mp}}}{\mu\, u_{\mathrm{mp}}}\, \dot{p}_r, \qquad \dot{p}_\theta^* = \frac{\dot{p}_\theta}{\mu\, u_{\mathrm{mp}}^2}, \qquad \dot{p}_\phi^* = \frac{\dot{p}_\phi}{\mu\, u_{\mathrm{mp}}^2}. \tag{84}$$

For the case where the atoms have equal mass (i.e. $m = m_1 = m_2$), $\mu = m/2$ and $\mu/M = 1/4$. This quantity, μ/M, is the product of the non-dimensionalized masses of each atom,

$$\frac{\mu}{M} = \frac{m_1}{M}\frac{m_2}{M}, \tag{85}$$

and as such could be considered another non-dimensional parameter.

3.5 Keck's Method

To calculate a trajectory, one must supply initial conditions. Intuitively, one might set the initial conditions of the adsorbate, then integrate the equations of motion forwards in time until (and if) the molecule desorbs. However, it was found early on that by applying initial conditions in this manner, only a small number of trajectories would even reach the reaction zone, or TS. Keck found an easier way. Basing his work on Transition State Theory (TST) [89; 139], Keck noted that every valid reaction must

pass through the TS. Hence, he chose to set initial conditions *at* the TS, rather than outside of it. He then integrated the equations of motion forwards and backwards in time, observing whether or not the full trajectory represented a chemical reaction. If not, it was rejected. He noticed that most of the trajectories were accepted. Due to its success, Keck's method is applied here [18; 72; 73].

A couple of observations can be made at this point about Keck's method. First, microscopic reversibility must hold in order to integrate the equations of motion backwards in time. Second, an assumption must be made about the initial conditions. Fortunately, it has been shown that an equilibrium distribution is present at the TS when products are absent [3]. For desorption, an absence of products implies that desorption is occuring in a vacuum, a valid assumption here.

3.6 Transition State (TS) Determination

TS locations must be determined before Keck's method can be implemented. The calculation of TS locations continues to be an active area for research [111]. As an example, one study on the H_2-Cu(111) system found that all desorption events had a single TS location in common [131], made possible perhaps by the simplified PES model (LEPS) employed. Meanwhile, another author has warned against assuming that desorption occurs from a well-defined TS since the surface provides a distribution of varying activation barriers [60].

With those studies in mind, this research has taken the following approach for the 6D Wiesenekker PES on H_2-Cu(100), similar to that found in Reference [131]. First, it is assumed that hydrogen is adsorbed to the surface either on top (T), hollow (H), or bridge (B) sites. Then, the 20 unique H-H adsorbate configurations with the adatom separation distance r within the bounds $a_l \leq r \leq 2a_l$ are considered. For each configuration, approximate reaction paths are calculated with their corresponding TS

locations via the Chain algorithm. Since each configuration usually exhibits a poorly-defined TS, the average TS location is assumed to be the TS through which every reaction path passes for that configuration. Finally, of the 20 configurations, only four were found to significantly contribute to thermal desorption (see Figure 13).

The determination of TS locations involves multiple coordinate systems, explained in Section 3.6.1, and the use of the Hessian matrix, explained in Section 3.6.2. The details of the Chain algorithm are presented in Section 3.6.3, after which an explanation of how average TS locations are determined for the H_2-Cu(100) system is given in Section 3.6.4.

3.6.1 Different Coordinate Systems.

There are multiple coordinate systems employed in CT simulations. They are introduced here to familiarize the reader with the different nomenclature. First, there is the Cartesian coordinate system, which explicitly describes the (x, y, z) coordinates of every atom in the molecule. For a molecule composed of two atoms with individual Cartesian coordinates (x_1, y_1, z_1) and (x_2, y_2, z_2), the molecule's location and orientation in Cartesian coordinates is $(x_1, y_1, z_1, x_2, y_2, z_2)$, as shown in Figure 10(a).

Then there are the internal coordinates of a molecules. Again, for a molecule with only two atoms, its location and orientation can be described by the Cartesian coordinates of its center of mass (x, y, z) and the spherical coordinates of the atoms (r, θ, ϕ) with respect to the center of mass. In internal coordinates, the molecule is represented by $(x, y, z, r, \theta, \phi)$, shown in Figure 10(b). To convert from Cartesian to

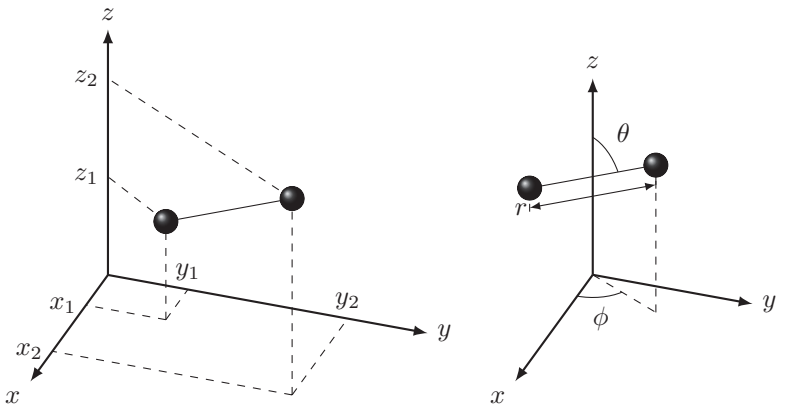

(a) Cartesian: $(x_1, y_1, z_1, x_2, y_2, z_2)$ (b) Internal: $(x, y, z, r, \theta, \phi)$

Figure 10. Cartesian and internal coordinate systems for a molecule with two atoms. The *x*-, *y*-, and *z*-coordinates for the internal system are at the center of mass of the molecule.

internal coordinates,

$$\begin{aligned} x &= \frac{x_1 + x_2}{2}, & r &= \sqrt{(x_1 - x_2)^2 + (y_1 - y_2)^2 + (z_1 - z_2)^2}, \\ y &= \frac{y_1 + y_2}{2}, & \theta &= \cos^{-1}\left(\frac{z_1 - z_2}{r}\right), \\ z &= \frac{z_1 + z_2}{2}, & \phi &= \tan^{-1}\left(\frac{y_1 - y_2}{x_1 - x_2}\right), \end{aligned} \tag{86}$$

and to convert from internal to Cartesian coordinates,

$$\begin{aligned} x_1 &= x + \Delta x, & x_2 &= x - \Delta x, \\ y_1 &= y + \Delta y, & y_2 &= y - \Delta y, \\ z_1 &= z + \Delta z, & z_2 &= z - \Delta z, \end{aligned} \tag{87}$$

where

$$\begin{aligned}\Delta x &= \frac{r}{2}\sin\theta\cos\phi,\\ \Delta y &= \frac{r}{2}\sin\theta\sin\phi,\\ \Delta z &= \frac{r}{2}\cos\theta.\end{aligned} \tag{88}$$

It is also be necessary to convert the time derivatives between the two coordinate systems, $(\dot{x}_1, \dot{y}_1, \dot{z}_1, \dot{x}_2, \dot{y}_2, \dot{z}_2)$ and $(\dot{x}, \dot{y}, \dot{z}, \dot{r}, \dot{\theta}, \dot{\phi})$, respectively. To convert the derivatives from Cartesian to internal coordinates, take the derivative with respect to time of Equation (86) while recalling the chain rule,

$$\dot{x} = \frac{\dot{x}_1 + \dot{x}_2}{2}, \qquad \dot{y} = \frac{\dot{y}_1 + \dot{y}_2}{2}, \qquad \dot{z} = \frac{\dot{z}_1 + \dot{z}_2}{2},$$

$$\dot{r} = \frac{(x_1 - x_2)(\dot{x}_1 - \dot{x}_2) + (y_1 - y_2)(\dot{y}_1 - \dot{y}_2) + (z_1 - z_2)(\dot{z}_1 - \dot{z}_2)}{r},$$

$$\dot{\theta} = \frac{-(\dot{z}_1 - \dot{z}_2) + \left(\dfrac{z_1 - z_2}{r}\right)\dot{r}}{r\sqrt{1 - \left(\dfrac{z_1 - z_2}{r}\right)^2}},$$

$$\dot{\phi} = \frac{-\left(\dfrac{y_1 - y_2}{x_1 - x_2}\right)(\dot{x}_1 - \dot{x}_2) + \dot{y}_1 - \dot{y}_2}{(x_1 - x_2)\left[1 + \left(\dfrac{y_1 - y_2}{x_1 - x_2}\right)^2\right]}. \tag{89}$$

To convert the derivatives from internal to Cartesian systems, take the derivative

with respect to time of Equations (87)-(88),

$$\dot{x}_1 = \dot{x} + \frac{1}{2}\,\dot{r}\sin\theta\cos\phi + \frac{1}{2}\,r\,\dot{\theta}\cos\theta\cos\phi - \frac{1}{2}\,r\,\dot{\phi}\sin\theta\sin\phi,$$

$$\dot{y}_1 = \dot{y} + \frac{1}{2}\,\dot{r}\sin\theta\sin\phi + \frac{1}{2}\,r\,\dot{\theta}\cos\theta\sin\phi + \frac{1}{2}\,r\,\dot{\phi}\sin\theta\cos\phi,$$

$$\dot{z}_1 = \dot{z} + \frac{1}{2}\,\dot{r}\cos\theta - \frac{1}{2}\,r\,\dot{\theta}\sin\theta,$$

$$\dot{x}_2 = \dot{x} - \frac{1}{2}\,\dot{r}\sin\theta\cos\phi - \frac{1}{2}\,r\,\dot{\theta}\cos\theta\cos\phi + \frac{1}{2}\,r\,\dot{\phi}\sin\theta\sin\phi,$$

$$\dot{y}_2 = \dot{y} - \frac{1}{2}\,\dot{r}\sin\theta\sin\phi - \frac{1}{2}\,r\,\dot{\theta}\cos\theta\sin\phi - \frac{1}{2}\,r\,\dot{\phi}\sin\theta\cos\phi,$$

$$\dot{z}_2 = \dot{z} - \frac{1}{2}\,\dot{r}\cos\theta + \frac{1}{2}\,r\,\dot{\theta}\sin\theta. \tag{90}$$

Note that the non-dimensionalized forms of Equations (86)-(90) are obtained by simply replacing each variable with its non-dimensional analog.

Even though Equations (86)-(90) are non-dimensionalized in a straight-forward manner, the non-dimensionalizations of the momenta in Cartesian coordinates must be handled more carefully. Each atom is represented with its own set of coordinates. Since each atom has its own mass (m_1 or m_2), the generalized momenta must be non-dimensionalized by the mass of the atom they are representing:

$$\begin{aligned} p_{x_1} &= m_1\dot{x}_1, & p_{y_1} &= m_1\dot{y}_1, & p_{z_1} &= m_1\dot{z}_1, \\ p_{x_2} &= m_2\dot{x}_2, & p_{y_2} &= m_2\dot{y}_2, & p_{z_2} &= m_2\dot{z}_2, \end{aligned} \tag{91}$$

and

$$p^*_{x_1} = \frac{p_{x_1}}{u_{\rm mp}\sqrt{m_1 M}}, \qquad p^*_{y_1} = \frac{p_{y_1}}{u_{\rm mp}\sqrt{m_1 M}}, \qquad p^*_{z_1} = \frac{p_{z_1}}{u_{\rm mp}\sqrt{m_1 M}},$$

$$p^*_{x_2} = \frac{p_{x_2}}{u_{\rm mp}\sqrt{m_2 M}}, \qquad p^*_{y_2} = \frac{p_{y_2}}{u_{\rm mp}\sqrt{m_2 M}}, \qquad p^*_{z_2} = \frac{p_{z_2}}{u_{\rm mp}\sqrt{m_2 M}}. \tag{92}$$

Or, in terms of velocities,

$$p^*_{x_1} = \dot{x}^*_1 \sqrt{\frac{m_1}{M}}, \qquad p^*_{y_1} = \dot{y}^*_1 \sqrt{\frac{m_1}{M}}, \qquad p^*_{z_1} = \dot{z}^*_1 \sqrt{\frac{m_1}{M}},$$

$$p^*_{x_2} = \dot{x}^*_2 \sqrt{\frac{m_2}{M}}, \qquad p^*_{y_2} = \dot{y}^*_2 \sqrt{\frac{m_2}{M}}, \qquad p^*_{z_2} = \dot{z}^*_2 \sqrt{\frac{m_2}{M}}, \tag{93}$$

where for equal masses $m_1 = m_2 = M/2$, and $\sqrt{m_1/M} = \sqrt{m_2/M} = 1/\sqrt{2}$.

Another way to describe the dynamics of the molecule is in the mass-weighted Cartesian (MWC) coordinate system [160:196-208]. Each of the Cartesian coordinates are multiplied by the square root of their respective atom's mass,

$$\left(x_1\sqrt{m_1},\, y_1\sqrt{m_1},\, z_1\sqrt{m_1},\, x_2\sqrt{m_2},\, y_2\sqrt{m_2},\, z_2\sqrt{m_2}\right),$$

where m_1 and m_2 are the masses of the two atoms in the molecule. The benefit of the MWC coordinate system can be seen by considering the Euler-Lagrange equations in Cartesian coordinates,

$$\frac{d}{dt}\left(\frac{\partial \mathcal{L}}{\partial \dot{q}_j}\right) = \frac{\partial \mathcal{L}}{\partial q_j}, \tag{94}$$

where q_j are the generalized coordinates $(x_1, y_1, z_1, x_2, y_2, z_2)$, and $\dot{q}_j$ are the generalized velocities $(\dot{x}_1, \dot{y}_1, \dot{z}_1, \dot{x}_2, \dot{y}_2, \dot{z}_2)$, and the Lagrangian $\mathcal{L} = \mathcal{T} - V$ is composed of the kinetic energy $\mathcal{T}$ and the potential energy V. The kinetic energy $\mathcal{T}$ is a function

of the $\dot{q}_j$ only,

$$\mathcal{T} = \frac{1}{2}\sum_j m_j \dot{q}_j^2. \tag{95}$$

The potential energy V can be expressed in the harmonic approximation as

$$V = V_0 + \frac{1}{2}\sum_{j,k} q_j H_{j,k} q_k, \tag{96}$$

where the linear term is neglected, V_0 is the potential energy V evaluated at some initial configuration, and $H_{j,k}$ is the (j,k) element of the Hessian matrix $\mathbf{H}$ (evaluated at the same initial configuration). By noting that $\mathcal{T} = \mathcal{T}(\dot{q})$ and $V = V(q)$, Equation (94) can be expressed as

$$\frac{d}{dt}\left(\frac{\partial \mathcal{T}}{\partial \dot{q}_j}\right) = \frac{\partial V}{\partial q_j},$$

$$m_j \ddot{q}_j = \sum_k H_{j,k} q_k, \tag{97}$$

where the double-dot notation indicates a second derivative with respect to time t. However, Equation (97) can be further simplified by expressing it in MWC coordinates,

$$\ddot{\beta}_j = \sum_k H'_{j,k} \beta_k, \tag{98}$$

where β_j is the j^{th} element of the generalized coordinates,

$$\left(x_1\sqrt{m_1},\, y_1\sqrt{m_1},\, z_1\sqrt{m_1},\, x_2\sqrt{m_2},\, y_2\sqrt{m_2},\, z_2\sqrt{m_2}\right),$$

and the MWC Hessian $\mathbf{H'}$ has elements

$$H'_{j,k} = \frac{H_{j,k}}{\sqrt{m_j m_k}}. \tag{99}$$

For the case where all of the atoms in the molecule have the same mass (i.e. $m_j = m_k$), or for the case where the molecule only has two atoms, $\mathbf{H'}$ is just a contant multiple of $\mathbf{H}$. The MWC generalized momenta p'_i can be expressed in terms of the momenta in Cartesian coordinates p_i, so that,

$$p'_{x_1} = \frac{p_{x_1}}{\sqrt{m_1}}, \qquad p'_{y_1} = \frac{p_{y_1}}{\sqrt{m_1}}, \qquad p'_{z_1} = \frac{p_{z_1}}{\sqrt{m_1}},$$

$$p'_{x_2} = \frac{p_{x_2}}{\sqrt{m_2}}, \qquad p'_{y_2} = \frac{p_{y_2}}{\sqrt{m_2}}, \qquad p'_{z_2} = \frac{p_{z_2}}{\sqrt{m_2}}. \tag{100}$$

The non-dimensionalized MWC momenta p'^*_i are then,

$$p'^*_{x_1} = \frac{p'_{x_1}}{u_{\mathrm{mp}}\sqrt{M}}, \qquad p'^*_{y_1} = \frac{p'_{y_1}}{u_{\mathrm{mp}}\sqrt{M}}, \qquad p'^*_{z_1} = \frac{p'_{z_1}}{u_{\mathrm{mp}}\sqrt{M}},$$

$$p'^*_{x_2} = \frac{p'_{x_2}}{u_{\mathrm{mp}}\sqrt{M}}, \qquad p'^*_{y_2} = \frac{p'_{y_2}}{u_{\mathrm{mp}}\sqrt{M}}, \qquad p'^*_{z_2} = \frac{p'_{z_2}}{u_{\mathrm{mp}}\sqrt{M}}. \tag{101}$$

It is interesting to note that the non-dimensional values of the Cartesian and the MWC momenta are identical (e.g. $p^*_{x_1} = p'^*_{x_1}$).

3.6.2 Hessian Matrix.

The Hessian matrix $\mathbf{H}$ is an important quantity because it arises in the quadratic term of a Taylor series expansion. For the Taylor series expansion of the potential energy V of the 6D PES [160:196-208],

$$V(\boldsymbol{q_0} + \boldsymbol{\Delta q}) = V(\boldsymbol{q_0}) + \sum_k \left.\frac{\partial V}{\partial q_k}\right|_{\boldsymbol{q_0}} \Delta q_k + \frac{1}{2}\sum_{j,k} \Delta q_j H_0^{j,k} \Delta q_k + \cdots, \tag{102}$$

where the Δq-terms represent steps of the Cartesian coordinates

$$\boldsymbol{\Delta q} = (\Delta x_1,\, \Delta y_1,\, \Delta z_1,\, \Delta x_2,\, \Delta y_2,\, \Delta z_2), \tag{103}$$

$\boldsymbol{q_0}$ is some initial system configuration, and $H_0^{j,k}$ is defined as the (j,k) element of the Hessian $\mathbf{H}$ evaluated at $\boldsymbol{q_0}$,

$$H_0^{j,k} = \left.\frac{\partial^2 V}{\partial q_j \partial q_k}\right|_{\boldsymbol{q_0}}. \tag{104}$$

Thus, the Hessian contains information concerning the second derivatives, and is the multi-dimensional analog to the one-dimensional second derivative. The non-dimensional form for a Hessian element in Cartesian coordinates $H^*_{j,k}$ is

$$H^*_{i,j} = \frac{a_l^2}{kT_s} H_{i,j}. \tag{105}$$

$\mathbf{H}$ is a symmetric matrix, so there is a unitary matrix $\mathbf{U}$ that diagonalizes $\mathbf{H}$, $(\mathbf{U}^T\mathbf{H}\mathbf{U})_{k,l} = \delta_{k,l}\lambda_k$, where $\delta_{k,l}$ is the delta function, λ_k is an eigenvalue of $\mathbf{H}$, and the ^{T} superscript denotes the matrix transpose. In addition, the columns of $\mathbf{U}$ are the eigenvectors of $\mathbf{H}$. For non-linear molecules, $3N-6$ of the eigenvalues will be non-zero, while for linear molecules, $3N-5$ of the eigenvalues will be non-zero. For a linear molecule with two atoms ($N=2$), only one eigenvalue will be non-zero, and five will be zero. Those five trivial eigenvalues correspond to the translational and rotational motions of the molecule. If the non-zero eigenvalue is actually negative, then the location $\boldsymbol{q_0} + \boldsymbol{\Delta q}$ is a saddle point on the PES. Hence, the problem of finding a saddle point on the PES (which can indicate a TS) is equivalent to locating where the Hessian has a negative eigenvalue.

To discretize Equation (104), a double-sided finite difference is employed. Since

the Hessian is a symmetric matrix, $H_0^{j,k} = H_0^{k,j}$. To reduce numerical error, each element is of the Hessian is calculated by averaging the two equal values, $H_0^{j,k}$ and $H_0^{k,j}$, so that

$$H_0^{j,k} = \frac{\left.\frac{\partial V}{\partial q_j}\right|_{\boldsymbol{q_0}+\boldsymbol{\Delta q_k}/2} - \left.\frac{\partial V}{\partial q_j}\right|_{\boldsymbol{q_0}-\boldsymbol{\Delta q_k}/2}}{2\Delta q_k} + \frac{\left.\frac{\partial V}{\partial q_k}\right|_{\boldsymbol{q_0}+\boldsymbol{\Delta q_j}/2} - \left.\frac{\partial V}{\partial q_k}\right|_{\boldsymbol{q_0}-\boldsymbol{\Delta q_j}/2}}{2\Delta q_j}, \tag{106}$$

where the configuration $\boldsymbol{q_0} + \boldsymbol{\Delta q_j}/2$ is the initial configuration $\boldsymbol{q_0}$ perturbed only in the j-direction by the value $\Delta q_j/2$, and the first-order derivatives are calculated with a central finite difference scheme,

$$\left.\frac{\partial V}{\partial q_j}\right|_{\boldsymbol{q_0}+\boldsymbol{\Delta q_j}/2} = \frac{V\left(\boldsymbol{q_0} + \frac{\boldsymbol{\Delta q_j}}{2} + \boldsymbol{\Delta q_j}\right) - V\left(\boldsymbol{q_0} + \frac{\boldsymbol{\Delta q_j}}{2} - \boldsymbol{\Delta q_j}\right)}{2\Delta q_j},$$

$$= \frac{V\left(\boldsymbol{q_0} + \frac{3}{2}\boldsymbol{\Delta q_j}\right) - V\left(\boldsymbol{q_0} - \frac{1}{2}\boldsymbol{\Delta q_j}\right)}{2\Delta q_j}, \tag{107}$$

and

$$\left.\frac{\partial V}{\partial q_j}\right|_{\boldsymbol{q_0}-\boldsymbol{\Delta q_j}/2} = \frac{V\left(\boldsymbol{q_0} - \frac{\boldsymbol{\Delta q_j}}{2} + \boldsymbol{\Delta q_j}\right) - V\left(\boldsymbol{q_0} - \frac{\boldsymbol{\Delta q_j}}{2} - \boldsymbol{\Delta q_j}\right)}{2\Delta q_j},$$

$$= \frac{V\left(\boldsymbol{q_0} + \frac{1}{2}\boldsymbol{\Delta q_j}\right) - V\left(\boldsymbol{q_0} - \frac{3}{2}\boldsymbol{\Delta q_j}\right)}{2\Delta q_j}. \tag{108}$$

The non-dimensionalized form of Equation (106) is obtained by simply starring each of the quantities.

When assigning initial values at the TS, it is important to consider the eigenmode

basis of $\mathbf{H}$. Mathematically, the eigenmode basis can be seen by employing the unitary matrix $\mathbf{U}$ in Equation (102),

$$\begin{aligned} V(\boldsymbol{q_0} + \boldsymbol{\Delta q}) &= V(\boldsymbol{q_0}) + \boldsymbol{g_0}^T \boldsymbol{\Delta q} + \frac{1}{2} \boldsymbol{\Delta q}^T \mathbf{H_0} \boldsymbol{\Delta q} + \cdots , \\ &= V(\boldsymbol{q_0}) + \boldsymbol{g_0}^T \mathbf{U}\mathbf{U}^T \boldsymbol{\Delta q} + \frac{1}{2} \boldsymbol{\Delta q}^T \mathbf{U}\mathbf{U}^T \mathbf{H_0} \mathbf{U}\mathbf{U}^T \boldsymbol{\Delta q} + \cdots , \\ &= V(\boldsymbol{q_0}) + \mathbf{G_0}^T \mathbf{Q} + \frac{1}{2} \mathbf{Q}^T \boldsymbol{\lambda_0} \mathbf{Q} + \cdots , \end{aligned} \tag{109}$$

since $\mathbf{U}\mathbf{U}^T = \mathbf{U}^T\mathbf{U} = \mathbf{I}$ by definition ($\mathbf{I}$ is the identity matrix), $\boldsymbol{g_0}$ is the gradient of V at $\boldsymbol{q_0}$ with components

$$g_0^k = \left. \frac{\partial V}{\partial q_k} \right|_{\boldsymbol{q_0}} , \tag{110}$$

$\boldsymbol{\lambda_0}$ is a diagonal matrix with the eigenvalues of $\mathbf{H_0}$ as elements of the diagonal, $\mathbf{Q} = \mathbf{U}^T \boldsymbol{\Delta q}$ is the component of the step $\boldsymbol{\Delta q}$ along the eigenvector basis set, and $\mathbf{G_0} = \mathbf{U}^T \boldsymbol{g_0}$ is the component of the gradient $\boldsymbol{g_0}$ along the eigenvector basis set. For a linear rotor, $\mathbf{H'}$ is a constant multiple of $\mathbf{H}$, and therefore the unit-length eigenvectors of $\mathbf{H'}$ and $\mathbf{H}$ are identical.

3.6.3 Chain Algorithm.

The determination of TS locations and reaction paths are active research areas [30; 142], and fall under the more general Mountain Pass Theorem [64]. The Chain algorithm, developed by Liotard and Penot [94; 95], addresses a specific need to calculate the TS location for a (approximate) reaction path, described by a chain of discrete points.

The Chain algorithm takes as inputs the initial (adsorbed) and final (desorbed) configurations, as well as the known PES. An initial path is chosen that connects the initial and final configurations, which is then modified until the TS is found. The TS is located at the saddle point with the largest energy value, while a saddle point

occurs where a negative eigenvalue of the Hessian matrix exists. The (approximate) Hessian is calculated on-the-fly via gradient calculations and the Broyden-Fletcher-Goldfarb-Shanno (BFGS) algorithm [136:521-523]. Note that the linear dependence threshold mentioned by Liotard and Penot [94; 135] is overcome by instead utilizing BFGS.

The initial reaction path is created with two straight lines connecting known starting and ending configurations M_1 and M_2, respectively, which are both minima on the PES. The intermediate point connecting M_1 with M_2 is taken as the starting configuration M_1 but with the intermolecular distance of the ending configuration M_2. In other words, if the starting configuration M_1 in internal coordinates is (x_1, y_1, z_1, r_1, θ_1, ϕ_1), and the ending configuration M_2 is (x_3, y_3, z_3, r_3, θ_3, ϕ_3), then the intermediate configuration is (x_1, y_1, z_1, r_3, θ_1, ϕ_1) since r_3 is the intermolecular distance of M_2. For each line, a linear interpolation between each of the coordinates creates the chain of points. In this work, each line was divided equally into 10 segments.

The calculation steps of the Chain algorithm are:

1. Set the threshold parameters ($l_1 = 0.01\, l_2$ and $l_0 = 0.01\, l_1$).

2. Determine the point $\boldsymbol{p_H}$ which currently approximates the TS. This is done by evaluating the potential V at every point on the chain. $\boldsymbol{p_H}$ is the point with the highest value of V.

3. Calculate the negative gradient of the potential at $\boldsymbol{p_H}$, $\boldsymbol{G} = -\nabla V(\boldsymbol{p_H})$, in Cartesian coordinates. Each of the partial derivatives is calculated with a central difference,

$$\frac{\partial V}{\partial x_i} = \frac{V(x_i + \Delta x) - V(x_i - \Delta x)}{2\Delta x}, \tag{111}$$

   where $\Delta x = l_0$.

4. Update the Hessian $\mathbf{H}$ via the BFGS algorithm. If the point $\boldsymbol{p_H}$ has not moved significantly in the most recent step, then $\mathbf{H}$ is not updated. In other words, if $||\boldsymbol{p_{H_{\text{new}}}} - \boldsymbol{p_{H_{\text{old}}}}|| < \epsilon_1$, then $\mathbf{H}_{\text{new}} = \mathbf{H}_{\text{old}}$. For this work, $\epsilon_1 = 10^{-5}\, a_l$.

5. Calculate the quadratic direction, $\boldsymbol{Q} = \mathbf{H}^{-1}\boldsymbol{G}$, and determine if $\boldsymbol{Q}$ is operative.

   (a) $\boldsymbol{Q}$ is operative if the index[2] of $\mathbf{H}$ is unity, $||\boldsymbol{Q}|| < l_2$, and $\boldsymbol{Q} \cdot \boldsymbol{G} > \epsilon_2\, ||\boldsymbol{Q}||\, ||\boldsymbol{G}||$, where $\epsilon_2 = 0.1$.

6. If the magnitude of the negative gradient $||\boldsymbol{G}||$ falls below a given threshold g_c (i.e. $||\boldsymbol{G}|| < g_c$), then stop; $\boldsymbol{p_H}$ is the TS. The gradient threshold g_c, below which the PES is assumed to be flat, is set at $0.04\ \text{kT}_s\, a_l^{-1}$.

7. Select the step direction $\boldsymbol{D}$ from either the quadratic direction $\boldsymbol{Q}$, the direction of the projected gradient $\boldsymbol{G}^*$, or one of the unit vectors $\boldsymbol{A}$ of the links adjacent to $\boldsymbol{p_H}$.

   (a) The quadratic direction $\boldsymbol{Q}$ is chosen if:

      i. $\boldsymbol{Q}$ is operative, $\boldsymbol{Q}$ is decreasing ($\boldsymbol{Q} \cdot \boldsymbol{G} > 0$), and $||\boldsymbol{G}|| < g_1$, where g_1 is a pre-convergence threshold on the gradient norm ($g_1 = 10 g_c$ here); or

      ii. $\boldsymbol{Q}$ is operative, $\boldsymbol{Q}$ is decreasing, and $\theta > \eta$, where θ is the angle between $\boldsymbol{G}$ and the pseudo-tangent to the path $\boldsymbol{T}$ ($\theta \in [0, 90^\circ]$), and η is a threshold value ($\eta = 30^\circ$ here). The pseudo-tangent $\boldsymbol{T}$ is defined as the unit vector parallel to the straight line between $\boldsymbol{p_{H-1}}$ and $\boldsymbol{p_{H+1}}$, or

$$\boldsymbol{T} = \frac{\boldsymbol{p_{H+1}} - \boldsymbol{p_{H-1}}}{||\boldsymbol{p_{H+1}} - \boldsymbol{p_{H-1}}||}. \tag{112}$$

[2]The index of $\mathbf{H}$ is defined as the number of negative eigenvalues of $\mathbf{H}$.

(b) The projected gradient $\boldsymbol{G^*}$ is defined as $\boldsymbol{G^*} = \boldsymbol{G} - (\boldsymbol{G} \cdot \boldsymbol{T})\boldsymbol{T}$. The direction of $\boldsymbol{G^*}$ is chosen if:

i. $\boldsymbol{Q}$ is operative, $\boldsymbol{Q}$ is increasing, and $\theta > \eta$; or

ii. $\boldsymbol{Q}$ is not operative, $\boldsymbol{Q}$ is decreasing, and $\theta > \eta$; or

iii. $\boldsymbol{Q}$ is not operative or $||\boldsymbol{G}|| < g_1$, and $\theta \leq \eta$.

(c) The more increasing unit vector $\boldsymbol{A}$ of the two links adjacent to $\boldsymbol{p_H}$ is chosen if:

i. $\boldsymbol{Q}$ is operative, $\boldsymbol{Q}$ is increasing, and $||\boldsymbol{G}|| < g_1$;

ii. $\boldsymbol{Q}$ is not operative, $\boldsymbol{Q}$ is increasing, and $\theta > \eta$; or

iii. If neither unit vector $\boldsymbol{A}$ is increasing, then no search direction is chosen for this step. Skip to Step 10, with $\boldsymbol{p^*}$ chosen as the midpoint between $\boldsymbol{p_{H-1}}$ and $\boldsymbol{p_{H+1}}$, or

$$\boldsymbol{p^*} = \frac{\boldsymbol{p_{H-1}} + \boldsymbol{p_{H+1}}}{2}. \tag{113}$$

8. Conduct a line search to find the optimal step length $\lambda \in [l_0,\, l_2]$. In the direction $\boldsymbol{D}$, evaluate V at 10 equally-spaced points beginning at l_0 and ending at l_2. The point with the lowest value of V determines the step length.

9. Calculate the new point $\boldsymbol{p^*}$, where

$$\boldsymbol{p^*} = \boldsymbol{p_H} + \lambda \frac{\boldsymbol{D}}{||\boldsymbol{D}||}. \tag{114}$$

10. Replace $\boldsymbol{p_H}$ with $\boldsymbol{p^*}$.

11. If necessary, reconstruct the chain by eliminating meanders and/or inserting new points.

12. Decrease the value of l_2. Here, $l_{2_{\text{new}}} = 0.9\, l_{2_{\text{old}}}$. The value of l_2 for the first step is 2 Å.

13. Return to Step 1.

The BFGS algorithm (see Step 4) is a quasi-Newton method, since it utilizes not the actual Hessian but an approximation to it. BFGS assumes that the PES can be approximated (locally) by the Taylor series expansion in Equation (109), so that at step i,

$$V(\boldsymbol{q}_\mathbf{0}^i + \boldsymbol{q}) \approx V(\boldsymbol{q}_\mathbf{0}^i) + \boldsymbol{g}_\mathbf{0}^{i\,T}\boldsymbol{q} + \frac{1}{2}\boldsymbol{q}^T\mathbf{H}_\mathbf{0}^i\boldsymbol{q}. \tag{115}$$

At each subsequent step $i+1$, the Hessian $\mathbf{H}_\mathbf{0}^i$ is updated to $\mathbf{H}_\mathbf{0}^{i+1}$ with information gained from the step taken $(\boldsymbol{q}_\mathbf{0}^{i+1} - \boldsymbol{q}_\mathbf{0}^i)$, and from the gradients at steps i and $i+1$, which are $\boldsymbol{g}_\mathbf{0}^i$ and $\boldsymbol{g}_\mathbf{0}^{i+1}$, respectively. In mathematical terms,

$$\begin{aligned}\mathbf{H}_\mathbf{0}^{i+1} =& \mathbf{H}_\mathbf{0}^i + \frac{(\boldsymbol{q}_\mathbf{0}^{i+1} - \boldsymbol{q}_\mathbf{0}^i) \otimes (\boldsymbol{q}_\mathbf{0}^{i+1} - \boldsymbol{q}_\mathbf{0}^i)}{(\boldsymbol{q}_\mathbf{0}^{i+1} - \boldsymbol{q}_\mathbf{0}^i)\cdot(\boldsymbol{g}_\mathbf{0}^{i+1} - \boldsymbol{g}_\mathbf{0}^i)} - \frac{[\mathbf{H}_\mathbf{0}^i\cdot(\boldsymbol{g}_\mathbf{0}^{i+1} - \boldsymbol{g}_\mathbf{0}^i)] \otimes [\mathbf{H}_\mathbf{0}^i\cdot(\boldsymbol{g}_\mathbf{0}^{i+1} - \boldsymbol{g}_\mathbf{0}^i)]}{(\boldsymbol{g}_\mathbf{0}^{i+1} - \boldsymbol{g}_\mathbf{0}^i)\cdot\mathbf{H}_\mathbf{0}^i\cdot(\boldsymbol{g}_\mathbf{0}^{i+1} - \boldsymbol{g}_\mathbf{0}^i)} \\ &+ [(\boldsymbol{g}_\mathbf{0}^{i+1} - \boldsymbol{g}_\mathbf{0}^i)\cdot\mathbf{H}_\mathbf{0}^i\cdot(\boldsymbol{g}_\mathbf{0}^{i+1} - \boldsymbol{g}_\mathbf{0}^i)]\,\boldsymbol{u}\otimes\boldsymbol{u},\end{aligned} \tag{116}$$

where the vector $\boldsymbol{u}$ is defined as

$$\boldsymbol{u} = \frac{(\boldsymbol{q}_\mathbf{0}^{i+1} - \boldsymbol{q}_\mathbf{0}^i)}{(\boldsymbol{q}_\mathbf{0}^{i+1} - \boldsymbol{q}_\mathbf{0}^i)\cdot(\boldsymbol{g}_\mathbf{0}^{i+1} - \boldsymbol{g}_\mathbf{0}^i)} - \frac{\mathbf{H}_\mathbf{0}^i\cdot(\boldsymbol{g}_\mathbf{0}^{i+1} - \boldsymbol{g}_\mathbf{0}^i)}{(\boldsymbol{g}_\mathbf{0}^{i+1} - \boldsymbol{g}_\mathbf{0}^i)\cdot\mathbf{H}_\mathbf{0}^i\cdot(\boldsymbol{g}_\mathbf{0}^{i+1} - \boldsymbol{g}_\mathbf{0}^i)}, \tag{117}$$

and $\otimes$ is the outer product of two vectors, resulting in a matrix. For example, the (i,j) component of $\boldsymbol{v}\otimes\boldsymbol{w}$ is $v_i w_j$. The Hessian at the first step is taken to be the identity matrix.

To avoid severe kinks in the reaction path, the chain is reconstructed and/or new points are inserted in Step 11, as shown in Figure 11. For the insertion of new points, if either of the two links connected to $\boldsymbol{p_H}$ have lengths longer than l_2, then a new point

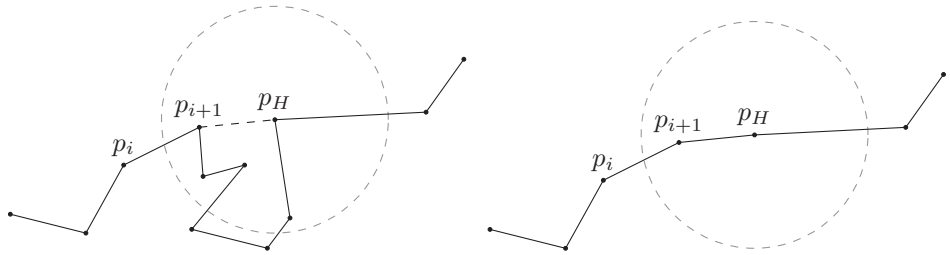

(a) Before (b) After

Figure 11. Two-dimensional representation of a meander bypass in the Chain algorithm. Here, p_{i+1} is inside the hypersphere, so the link is made between p_{i+1} and p_H. However, if p_i happened to be the point in the hypersphere, then the new link would be made between p_i and p_H.

is either placed halfway through that link, or at a distance l_2 from $\boldsymbol{p_H}$, whichever is smaller. To bypass meanders in the chain, a hypersphere is constructed around point $\boldsymbol{p_H}$ of radius r_{HS} (set to 2 Å). Beginning at the start of the chain (with M_1 as the first point of the first link), each link is tested in order until $\boldsymbol{p_H}$ is reached. Let point $\boldsymbol{p_i}$ be the start of the link under consideration, and let $\boldsymbol{p_{i+1}}$ be the end of the same link. If the link crosses the hypersphere, then the chain is modified in one of two ways. Either $\boldsymbol{p_H}$ is connected with $\boldsymbol{p_i}$ or with $\boldsymbol{p_{i+1}}$, depending on whether $\boldsymbol{p_{i+1}}$ is outside of the hypersphere or not, respectively. As a result, all of the points that existed on the chain between $\boldsymbol{p_i}$ (or $\boldsymbol{p_{i+1}}$) and $\boldsymbol{p_H}$ are permanently removed. The same procedure is repeated, except that it is begun at the end of the chain (with M_2 as the last point of the last link).

An example reaction path calculated with the Chain algorithm is presented in Figure 12. The adsorbed configuration corresponds to $r = a_l$, while the desorbed configuration is located at $z = 1.8\,a_l$. The x-, y-, θ-, and ϕ-values are constant in this example. The atoms start in the adsorbed configuration, travel along the 2D PES to the TS, and then continue on to the desorbed configuration. The calculated reaction path is approximate; output of the Chain algorithm is only the TS location.

The example shown in Figure 12 is only for two dimensions. Even though Chain

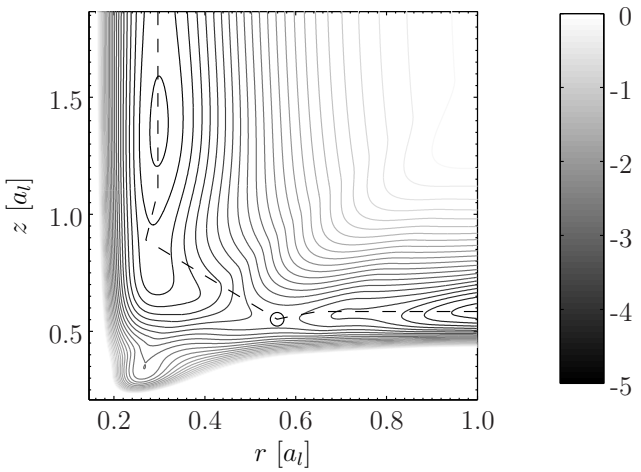

Figure 12. An example path calculation with the Chain algorithm. The important data point is the TS location (circle). The approximate reaction path (dashed line) is only useful in arriving at the TS location, and is discarded after the calculations are completed. x, y, θ, and ϕ are constant in this example. The adsorbed configuration is at $r = a_l$, while the desorbed configuration is at $z = 1.8\ a_l$. Contour lines are expressed in units of eV. This contour plot is a 2D slice of the 6D PES for $x = a_l$, $y = a_l/2$, $\theta = 90°$, and $\phi = 90°$, copresponding to the case wherein hydrogen atoms are adsorbed on top of adjacent copper atoms, and desorbed as H_2 above a bridge site.

calculations must consider all six dimensions, each link can be uniquely described by five 2D lines,

$$\alpha_j = m_j \alpha_1 + b_j, \tag{118}$$

where α_1 is one of the six Cartesian coordinates (not neccesarily x_1), j is an index that cycles through the remaining five coordinates, b_j is the α_j-intercept (when $\alpha_1 = 0$), and m_j is the slope of the 2D line,

$$m_j = \frac{\alpha_{j,i+1} - \alpha_{j,i}}{\alpha_{1,i+1} - \alpha_{1,i}}, \tag{119}$$

where the subscripts $i+1$ and i signify that the coordinates are from points $\boldsymbol{p_{i+1}}$ and $\boldsymbol{p_i}$, respectively. α_1 must be chosen such that m_j is defined. However, unless $\boldsymbol{p_i}$ and $\boldsymbol{p_{i+1}}$ are the same point, there will be at least one coordinate that can be chosen as α_1.

The equations to determine whether or not a link crosses the hypersphere were

not found in the literature. Thus, they were derived for this work. The equation for the hypersphere, centered at (α_{1c}, α_{2c}, α_{3c}, α_{4c}, α_{5c}, α_{6c}), is

$$\begin{aligned} r_{\mathrm{HS}}^2 &= \sum_{j=1}^{6}(\alpha_j - \alpha_{jc})^2, \\ &= (\alpha_1 - \alpha_{1c})^2 + \sum_{j=2}^{6}(\alpha_j - \alpha_{jc})^2, \\ &= (\alpha_1 - \alpha_{1c})^2 + \sum_{j=2}^{6}\left[(m_j\alpha_1 + b_j) - \alpha_{jc}\right]^2. \end{aligned} \tag{120}$$

Solving for α_1, the generalized quadratic formula is obtained,

$$\alpha_1 = \frac{-b \pm \sqrt{b^2 - 4ac}}{2a}, \tag{121}$$

where

$$\begin{aligned} a &= \frac{1}{2}\left(1 + \sum_{j=2}^{6} m_j^2\right), \\ b &= \sum_{j=2}^{6} b_j m_j - \sum_{j=2}^{6} m_j\alpha_{jc} - \alpha_{1c}, \\ c &= \frac{1}{2}\left[\sum_{j=2}^{6}(\alpha_{jc} - b_j)^2 + \alpha_{1c}^2 - r_{\mathrm{HS}}^2\right]. \end{aligned} \tag{122}$$

Once α_1 is calculated, the rest of the crossing-point coordinates can be determined from Equation (118). The crossing points are then tested to determine if they lie on the link in question or not.

3.6.4 TS Locations for H_2-Cu(100).

This section describes in detail how adsorbed and desorbed configurations are chosen (inputs to the Chain algorithm), and how the most important (average) TS

locations are selected for CT simulations.

The Chain algorithm requires adsorbed and desorbed configurations as inputs. Adsorbate configurations are assumed to be a subset of the symmetry adsorption sites on the copper surface. A symmetry site is one in which the hydrogen atom is adsorbed either above a bridge site (B), a hollow site (H), or directly on top of a copper atom (T). Since there are many unique symmetry configurations on a surface, only a subset of symmetry configurations may be chosen to determine the most likely TS locations that contribute to H_2 desorption. If only symmetry configurations where the two H atoms are no less than a_l (but no more than $2\,a_l$) apart, $a_l \leq r \leq 2a_l$, are considered, then there are 20 unique symmetry configurations. All of the adsorbed configurations are initially assumed to be parallel to the surface ($\phi = 90°$) while the height above the surface z is optimized by minimizing V while keeping x, y, r, θ, and ϕ constant. The configurations are then relaxed by minimizing V within a hypersphere of radius $r_{\mathrm{HS}} = 0.01\,a_l$ by taking an optimal step in the direction of the negative gradient of the potential $\boldsymbol{G} = -\nabla V$ [see Equation (111)]. This optimization strategy is also referred to as a line search. A line search is therefore conducted to find the optimal step length $\lambda \in [r_{\mathrm{HS}}/100, r_{\mathrm{HS}})$ in the direction of $\boldsymbol{G}$. To do so, V is evaluated at 10 equally-spaced points beginning at $r_{\mathrm{HS}}/100$ and ending at r_{HS}. If it is found that $\lambda = r_{\mathrm{HS}}$, then r_{HS} is increased by $0.01\,a_l$, and the line search is repeated until $r_{\mathrm{HS}}/100 \leq \lambda < r_{\mathrm{HS}}$. This technique is similar to the trust radius method [35]. Examples of initial and relaxed adsorbed configurations are shown in Figure 13.

Desorbed configurations have as their height $z = 9\,a_0 = 1.87\,a_l$ (above which the influence of the PES is negligible), and as their intermolecular bond length $r = 0.291\,a_l$, which is the equilibrium bond distance for an H_2 molecule in the gas phase [175]. The remaining locations and angles are chosen randomly with a uniform distribution over the unit cell and the unit sphere, so that $x \in [0, a_l]$, $y \in [0, a_l]$,

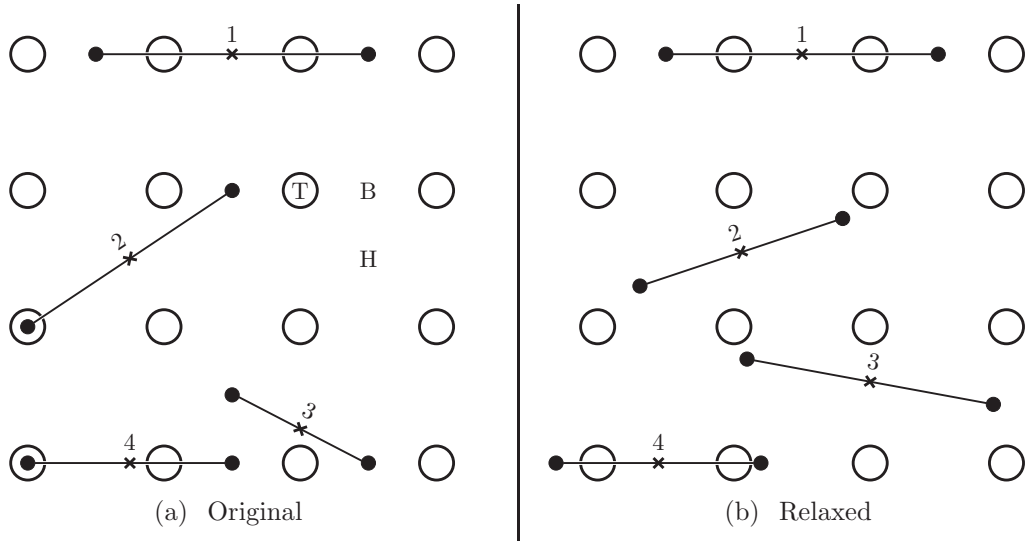

Figure 13. The symmetry sites found to contribute the most to thermal desorption under the CT construct, as seen perpendicular to the xy-plane. Empty circles represent the copper surface atoms, while filled circles represent adsorbed hydrogen atoms. The numbers correspond to those found in Table 1. The perfectly symmetric (original) configurations are shown in 13(a), where the adsorbed hydrogen atoms are located either on top (T), bridge (B), or hollow (H) sites. After conducting a trust radius calculation on the original configurations, the actual (relaxed) configurations are obtained [shown in 13(b)]. It is interesting to note that the relaxed configurations tend to position the midpoints near bridge sites.

$\theta \in [0, 2\pi]$, and $\phi \in [0, \pi]$. Note that for a random location on the unit sphere, θ can be assigned a uniform random angle by $\theta = 2\pi R_1$, while ϕ must be assigned a random angle through the relation $\phi = \cos^{-1}(2R_2 - 1)$, where R_1 and R_2 are uniform random numbers on $[0, 1]$.

Each adsorbed configuration is matched with 5000 random desorbed configurations, from which 5000 TS locations are determined. By taking an average TS location for each symmetry configuration, 20 average TS locations are identified as possible contributors to thermal desorption. To determine which TS locations significantly contribute to thermal desorption, trajectories were calculated for 19 of the 20 configurations[3] at a surface temperature of $T_s = 1100$ K. The desorption angle results were then compared with experimental values (see Figure 16(a)), and each configuration was weighted to optimize the fit between simulation and experiment. The corresponding relaxed adsorption configurations are shown in Table 1, the weights and average TS locations are shown in Table 2, and a comparison between TS locations and relaxed adsorption configurations is shown in Figure 14. It was found in this research that only four configurations were required to match desorption angle experimental values for that specific temperature. It is assumed that those four configurations dominate thermal desorption over all temperature regimes.

Trajectories were calculated by integrating Equations (82) forwards and backwards in time from the TS accroding to Keck's method. The ode45 function in MATLAB™ solves nonstiff differential equations with fourth-order accuracy, and was used to perform the calculations. It employs the explicit Runge-Kutta $(4, 5)$ formula (the Dormand-Prince pair). As such, ode45 is a one-step solver, meaning that it only requires information from the immediately-preceding step. For integration forward in

[3]One of the configurations was rejected due to unreasonable simulation times (more than four hours per trajectory on average). That configuration corresponded to the H atoms both adsorbed at bridge sites ($2\,a_l$ apart), desorbing as H_2 above the bridge site halfway between them.

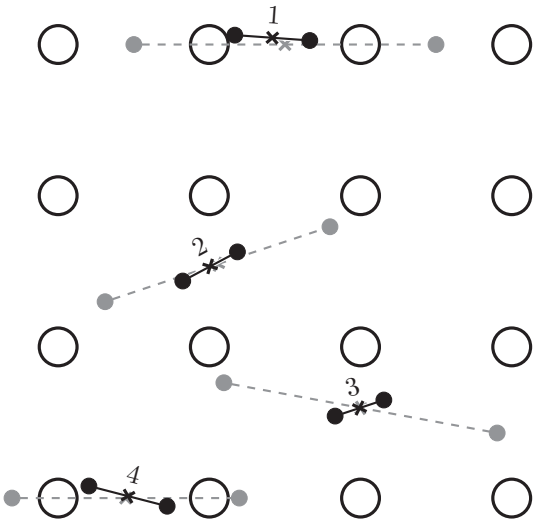

Figure 14. A comparison of the average TS locations (black) and the relaxed adsorption configurations (grey), as seen perpendicular to the xy-plane. The TS locations tend to have midpoints directly above the midpoints for the relaxed adsorption configurations.

Table 1. Relaxed adsorption symmetry site values.

	Internal Coordinates					
Site Label	x $[a_l]$	y $[a_l]$	z $[a_l]$	r $[a_l]$	θ	ϕ
1	0.50	0.00	0.59	2.00	90°	0°
2	0.05	0.55	0.52	1.57	90°	18°
3	0.00	0.60	0.48	1.84	90°	170°
4	0.45	0.00	0.56	1.50	90°	0°

time from the TS, integration stops when the molecule's height above the surface is $z = 1.87\, a_l$, which is the criterion for desorption. If, however, the molecule dissociates ($r > 0.784\ a_l$) before desorbing, then the trajectory is rejected [131]. For integration backward in time from the TS, integration stops once the molecule has dissociated. Similarly, the molecule cannot desorb before it dissociates in the backwards direction in order for the trajectory to be considered valid.

Table 2. Average TS locations with their respective weights.

		Internal Coordinates					
TS Label	Weight [%]	x $[a_l]$	y $[a_l]$	z $[a_l]$	r $[a_l]$	θ	ϕ
1	44.6	0.42	0.04	0.71	0.50	96°	176°
2	32.2	0.01	0.53	0.52	0.45	115°	28°
3	12.2	0.99	0.60	0.50	0.35	104°	18°
4	11.0	0.46	0.01	0.60	0.54	100°	165°

3.7 Initial Conditions

With Keck's method, a trajectory begins at the TS and is calculated forwards and backwards in time. Therefore, initial conditions correspond to the momenta at the TS location. The momenta are found by first selecting a random value of the molecule's energy from a truncated MB distribution (adjusted for the energy lost by the adsorbate in overcoming the activation barrier), and then randomly distributing that energy among the six momenta in the MWC Hessian eigenspace with equal probability. The MWC momenta in the Hessian eigenspace are then converted to MWC momenta in the Cartesian eigenspace, after which the momenta are converted to internal coordinates for calculation purposes.

3.7.1 Truncated Maxwell-Boltzmann (MB) Distribution.

The adatoms are assumed to be in equilibrium at the surface temperature, described by the MB distribution f_E,

$$f_E \, dE = 2 \sqrt{\frac{E}{\pi}} \left(\frac{1}{kT_s} \right)^{3/2} \exp\left(-\frac{E}{kT_s} \right) dE, \tag{123}$$

where $f_E\,dE$ is the probability that an adatom will have an energy in the range E to $E + dE$. In non-dimensional units,

$$f_{E^*}\,dE^* = 2\sqrt{\frac{E^*}{\pi}}\,\exp\left(-E^*\right)dE^*. \tag{124}$$

However, once the molecules arrive at the TS, they have lost some energy. This energy is simply the difference in potential energy between the adsorbed configuration and the TS configuration, ΔV. The energy distribution of the molecules at the TS can then be described by a truncated MB distribution f_{TS},

$$f_{\mathrm{TS}}\,dE^* = 2\sqrt{\frac{E^* + \Delta V^*}{\pi}}\,\exp\left[-(E^* + \Delta V^*)\right]dE^*, \tag{125}$$

where Equation (124) has been shifted to the left by $\Delta V^* = \Delta V/(kT_s)$, and only positive values of E^* are valid. Discrete values are chosen randomly from this distribution in an accept-reject manner [20:423-428], which requires the distribution to be normalized by its maximum value. Equation (124) has its maximum at $E^* = 1/2$, while Equation (125) peaks at $E^* = 1/2 - \Delta V^*$ with a value of $f_{\max}$,

$$f_{\max} = \sqrt{\frac{2}{\pi}}\,\exp\left(-\frac{1}{2}\right). \tag{126}$$

However, this maximum only occurs for $\Delta V^* \leq 1/2$. For $\Delta V^* > 1/2$, the maximum occurs at $E^* = 0$ with the value

$$f_{\max} = 2\sqrt{\frac{\Delta V^*}{\pi}}\,\exp\left(-\Delta V^*\right). \tag{127}$$

Therefore, the fully normalized and truncated MB distribution f'_{TS}, shown in Figure 15, is

$$f'_{\mathrm{TS}} = \begin{cases} \left[2\left(E^* + \Delta V^*\right)\right]^{1/2} \exp\left[-\left(E^* + \Delta V^* - \dfrac{1}{2}\right)\right], & \Delta V^* \leq \dfrac{1}{2}, \\ \left(\dfrac{E^*}{\Delta V^*} + 1\right)^{1/2} \exp\left(-E^*\right), & \Delta V^* > \dfrac{1}{2}. \end{cases} \tag{128}$$

Following the accept-reject method, given ΔV^*, a random value of E^* is chosen from a uniform distribution $E^* \in [0, E^*_{\mathrm{max}}]$, where E^*_{max} is a discrete approximation for positive infinity. For $E^*_{\mathrm{max}} = 12$, the cumulative distribution function (CDF) value at E^*_{max} is at most only 0.000025 less than unity, so $E^*_{\mathrm{max}} = 12$ is the chosen upper limit. A uniform random number is then selected, $R \in [0, 1]$. If $R < f'_{\mathrm{TS}}(E^*)$, then E^* is accepted. Otherwise, E^* is rejected, and another value of E^* is randomly selected until a value is accepted. Note that in the limit as $\Delta V^* \to \infty$, the normalized distribution approaches an exponential decay curve, $f'_{\mathrm{TS}} \to \exp(-E^*)$. On a practical level, for $\Delta V^* \geq 10$, the normalized distribution can reasonably be approximated as $f'_{\mathrm{TS}} = \exp(-E^*)$.

3.7.2 Mass-Weighted Cartesian (MWC) Hessian Eigenspace.

With E^* chosen, the initial momenta in the MWC Hessian eigenspace $p'^*_{u,i}$ are determined by dividing the energy among the (squared) six momenta randomly from uniform distributions. The subscript u indicates that the momenta are in the directions of the MWC Hessian eigenvectors $\bar{u}_i$. Since the change in the potential energy has already been taken into account, E^* is equivalent to the non-dimensional kinetic

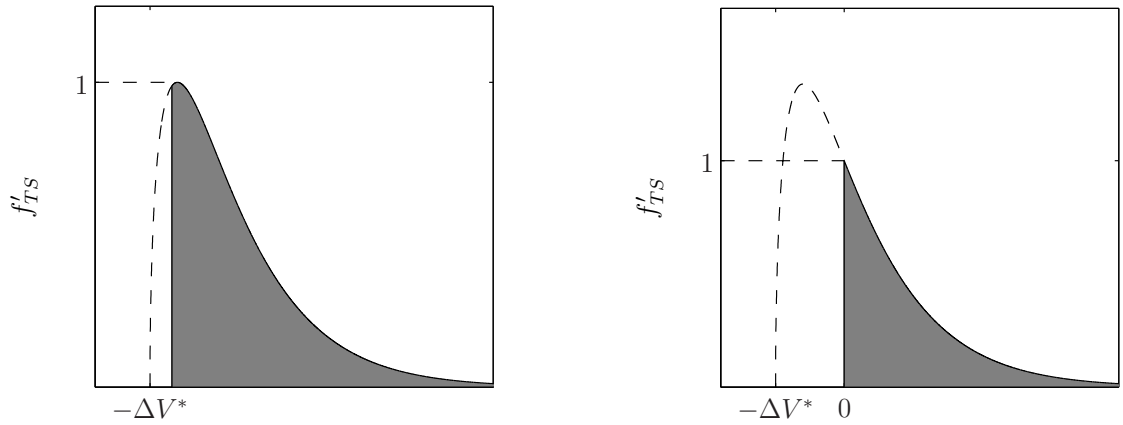

(a) $\Delta V^* \leq \frac{1}{2}$ (b) $\Delta V^* > \frac{1}{2}$

Figure 15. Representations of the fully-normalized and truncated MB distribution f'_{TS} for different values of ΔV^* [see Equation (128)]. The shaded area is the actual distribution, starting at $E^* = 0$. The dashed portion of the curve shows where the MB distribution has been truncated, and has as its minimum abscissal value $-\Delta V^*$.

energy of the molecule $\mathcal{T}^*$, which can be written as

$$\mathcal{T}^* = \sum_{i=1}^{6} {p'^*_{u,i}}^2. \tag{129}$$

For six random uniform numbers $R_i \in [0, 1]$ such that,

$$\sum_{i=1}^{6} R_i = 1, \tag{130}$$

the momenta can be expressed as,

$$\sum_{i=1}^{6} {p'^*_{u,i}}^2 = \sum_{i=1}^{6} R_i \mathcal{T}^*, \tag{131}$$

such that,

$$p'^*_{u,i} = \pm\sqrt{R_i \mathcal{T}^*}. \tag{132}$$

If $\bar{u}_j$ is the Hessian eigenvector with the negative eigenvalue, then the corresponding momentum $p'^*_{u,k}$ should be in the positive direction,

$$p'^*_{u,k} = \sqrt{R_k \mathcal{T}^*}, \tag{133}$$

since that is the direction of recombination across the TS. The other five momenta, however, retain the $\pm$ symbol in Equation (132).

The momenta in MWC coordinates $p'^*_{c,i}$ are then recovered by multiplying the momenta in the MWC Hessian eigenspace $p'^*_{u,j}$ by the Hessian eigenvectors $\bar{u}_j$,

$$p'^*_{c,i} = \sum_{j=1}^{6} \bar{u}_j(i)\, p'^*_{u,j}, \tag{134}$$

where $\bar{u}_j(i)$ is the i-th element of the eigenvector $\bar{u}_j$. Momenta in internal coordinates can then be obtained by the transformations discussed previously [see Equations (76), (78), (90)-(91), and (100)-(101)].

3.8 Dynamic Simulation of Desorption Events

As time passes in a real gas-surface system, the coverage on the surface changes due to adsorption, desorption, and permeation. Desorption modeling has been addressed for each event. However, one must calculate when each desorption event occurs. Also, the rate of atoms arriving at the surface via permeation must be identified. Therefore, Section 3.8.1 introduces the topic of permeation and how it can be applied to the current model, and Section 3.8.2 applies MC event timing to the DSMC framework.

3.8.1 Permeation.

As hydrogen molecules desorb from the surface, new hydrogen atoms are supplied to the surface via permeation at the rate Q. When a pressure differential exists,

molecules tend to diffuse from areas of high concentration to areas of low concentration, even in the presence of a membrane or structural component, such as a magnetron wall. For the example of a magnetron, the outer casing experiences atmospheric pressure, while the inner cavity is held at a sub-atmospheric pressure. Thus, molecules from the atmosphere tend to permeate the structure because of the pressure differential, and find their way to the surface of the inner cavity. Hydrogen permeates easily through many materials, including copper. The process of permeation (and then desorption) for hydrogen on copper is [54]:

1. The (atmospheric) hydrogen gas first adsorbs to the outer surface, dissociating into hydrogen adatoms in the process.

2. Hydrogen adatoms are then *ab*sorbed into the copper bulk according to the hydrogen-copper solubility.

3. Hydrogen atoms then diffuse through the copper bulk to the inner surface, driven by the pressure differential existing between the two surfaces, and determined by the hydrogen-copper diffusivity.

4. Upon reaching the inner surface, hydrogen atoms become adatoms, adsorbed to the surface.

5. Through a desorption process, the hydrogen molecule desorbs from the copper surface into the low-pressure environment.

By inspection, it is apparent that Steps 1 and 2 are the reverse processes of Steps 4 and 5. Permeation is a function of the pressures at both surfaces, the solubility and diffusivity of the system, as well as the temperature of the copper. These dependencies will become more apparent as the relevant mathematical relations are presented.

The total permeation Q of molecules per unit time t through the membrane is calculated by

$$Q = \boldsymbol{J} \cdot \boldsymbol{A}, \tag{135}$$

where $\boldsymbol{J}$ is the flux of molecules traveling through the area $\boldsymbol{A}$, and the dot product is necessary so that only the flux normal to the surface is considered.

Fick's First and Second Laws describe how the flux $\boldsymbol{J}$ and concentration of molecules ϕ varies within the material according to diffusion, in steady-state and general conditions, respectively [54; 153]. Fick's Second Law, analogous to the heat equation, is

$$\frac{\partial \phi}{\partial t} = D \, \nabla^2 \phi, \tag{136}$$

where ϕ is the concentration, D is the diffusion coefficient, t is time, and ∇^2 is the Laplace operator. Under steady-state conditions, Fick's Second Law reduces to Laplace's equation,

$$\nabla^2 \phi = 0, \tag{137}$$

which can be further manipulated to obtain Fick's First Law,

$$\boldsymbol{J} = -D \, \nabla \phi, \tag{138}$$

where ∇ is the gradient operator.

Boundary conditions at both surfaces are required to solve Equation (138), which are determined via Sievert's Law. This law states that the concentration of atoms ϕ dissolved in a metal is directly proportional to the gas-solid solubility S and the square root of the fugacity f of the gas molecules in thermodynamic equilibrium,

$$\phi = S \sqrt{f}, \tag{139}$$

where the fugacity f is equal to the gas partial pressure P for an ideal gas. With the assumption that the desorption surface is under vacuum conditions ($P = 0$), Equation (138) can be solved for a given geometry. For a planar geometry,

$$Q = \frac{A\,\Phi\,\sqrt{P}}{d}, \tag{140}$$

where d is the thickness of the membrane, P is the non-vacuum pressure, and $\Phi = DS$ is the permeability, while for a cylindrical geometry,

$$Q = \frac{2\pi h\,\Phi\,\sqrt{P}}{\ln\left(\frac{a}{b}\right)}, \tag{141}$$

where h is the height of the cylinder, a is the outside radius, and b is the inside radius. Because of the assumption of vacuum conditions, Equations (140)-(141) give the maximum permeation rate. Real conditions will therefore exhibit a lower Q-value.

The permeability Φ is identified with the product of diffusivity D and solubility S, which is independent of the specific geometry,

$$\Phi = DS. \tag{142}$$

Typically, D and S are expressed in terms of temperature by

$$D(T) = D_0 \exp\left(-\frac{E_D}{kT}\right),$$

$$S(T) = S_0 \exp\left(-\frac{E_S}{kT}\right), \tag{143}$$

where D_0 and S_0 are constants, E_D and E_S are activation energies, k is the Boltzmann constant, and T is temperature. Therefore, the permeability Φ is expressed as

$$\Phi(T) = \Phi_0 \exp\left(-\frac{E_\Phi}{kT}\right), \tag{144}$$

where $\Phi_0 = D_0 S_0$ and $E_\Phi = E_D + E_S$. Values of the constants and activation energies for Hydrogen in various materials can be found in Reference [153].

3.8.2 Timing.

The timing of events is an important part of simulating dynamic desorption and adsorption [46; 61; 92]. The DSMC algorithm simulates the discrete Bernoulli process. By associating a time step with each event, DSMC desorption produces a Markov chain of events [61], which simulates a Poisson process since the system is large and contains only independent events [46].

The probability density of times between successive events f_t for a Poisson process is [46]

$$f_t = r \exp\left(-r\, t\right), \tag{145}$$

with the average time between events $\langle t \rangle$ being

$$\langle t \rangle = \frac{1}{r}, \tag{146}$$

where r is the event rate. Instead of invoking the average time between events as the time step, however, time is incremented after each desorption event by

$$\Delta t = -\frac{1}{r} \ln R, \tag{147}$$

where R is a uniform random number between 0 and 1, and r may be different for

each event. Equation (147) differs from the corresponding equation in Reference [46] by determining Δt only from the desorption rate of that particular event, rather than from the sum of the rates of all events from all subpopulations. The distinction is made here since time is incremented in a different fashion than it is with MC methods. In MC, the time step is incremented after a certain number of events have passed (e.g. 50), while in these simulations, time is incremented after *every* event.

The total rate of desorption r is calculated from the Polanyi-Wigner model [77],

$$r = \frac{dN}{dt} = -\nu N^x \exp\left(-\frac{E}{kT}\right) \tag{148}$$

where ν is a frequency factor, x is the reaction order for desorption, E is the average desorption activation energy, and N is the number of adatoms on the surface. Values of ν, x, and E are published in the literature. Anger et al. present these values for H_2-Cu(111) and H_2-Cu(110) [5]. However, since the surface of Cu(100) undergoes a reconstruction at high hydrogen coverage [31], H_2-Cu(100) TPD spectra are published, but values for ν, x, and E are not. Fortunately, their TPD spectra can be analyzed independently by the Threshold TPD (TTPD) method presented in References [57; 77; 117].

To calculate r for the next time step $(i+1)$, values must be taken from step (i) (e.g. Q, r, and Δt), since r is a function of the number of adatoms found on the surface, supplied by permeation and adsorption, and depleted via desorption. Therefore, the number of adatoms available for desorption at time step $(i+1)$ is calculated as

$$N^{(i+1)} = \left[Q^{(i)}(T^{(i)}) - r^{(i)}\right] \Delta t^{(i)}, \tag{149}$$

where the superscript indicates the time step from which values are taken. Substituting Equation (149) into Equation (148), r for the $(i+1)^{\text{th}}$ time step is readily

calculated by

$$r^{(i+1)} = -\nu \left[N^{(i+1)}\right]^x \exp\left[-\frac{E}{kT^{(i+1)}}\right]. \tag{150}$$

During a DSMC simulation, each desorption event should be determined in the following manner. Before time step $(i+1)$ begins, if the time that has passed since the last desorption event is greater than $\Delta t^{(i)}$, then desorption should occur at the local surface temperature $T_s^{(i)}$. A new value of Δt should be calculated at each time step until this condition is reached, unless if the surface temperature remains unchanged from the previous time step.

3.9 Results

Results from the current method are presented in this section. Emphasis is placed on comparing theoretical simulations with the most up-to-date experimental data available for thermal desorption from the H_2-Cu(100) gas-surface system [158]. These results are for a surface temperature of $T_s = 1030$ K and include state-resolved mean translational energy values, state-resolved translational energy distributions, and the quadrupole alignment parameter $A_0^{(2)}$. In addition, the desorption angle distribution at $T_s = 1100$ K is shown. Recall from Section 3.6.4 that contributing TS locations and their respective weights were determined by fitting simulation results to experimental data.

3.9.1 Desorption Angle Distribution.

In order to compare theory with experimental results from Reference [12], a geometrical factor based on the experimental measuring equipment must be taken into account. Simulation results give a desorption angle for each molecule, while experimental data provide the number of molecules that arrive at a detector covering a finite solid angle Ω, at multiple locations in space.

As an example, for the measurements reported in Reference [157], the detector is 9 mm away from the surface with a diameter of 2 mm, giving a solid angle of $\Omega = 0.0384$ steradians, whereas an entire sphere covers 4π steradians. Thus, the detector covers only a portion (a cap) of the surface of the sphere, while all simulated molecules with identical desorption angles have the same latitude. To compare the two, a latitudinal band is constructed by rotating the cap about the surface normal. This band has a finite width corresponding to the diameter of the detector. The cap covers an area A_{cap} of

$$A_{\text{cap}} = 2\pi R^2(1 - \cos\Delta\theta), \tag{151}$$

where R is the distance of the detector from the surface, $\Delta\theta = \tan^{-1}(r/R)$, and r is the radius of the detector. To continue this example, $R = 9$ mm, $r = 1$ mm, $\Delta\theta = 6.34°$, and $A_{\text{cap}} = 3.11$ mm^2. The area of the latitudinal band A_{band} is found to be

$$A_{\text{band}} = 4\pi R^2 \sin\theta \sin\Delta\theta, \tag{152}$$

where θ is the desorption angle of interest, measured from the surface normal. However, Equation (152) only holds when $\theta \geq \Delta\theta$. For the case where $\theta < \Delta\theta$, Equation (152) must be modified to account for overlapping areas,

$$A_{\text{band}} = 2\pi R^2 \left(1 + \sin\theta \sin\Delta\theta - \cos\theta \cos\Delta\theta\right). \tag{153}$$

To then compare simulation results with experimental data, one needs to only multiply the simulation values by the ratio $A_{\text{cap}}/A_{\text{band}}$,

$$\frac{A_{\text{cap}}}{A_{\text{band}}} = \begin{cases} \dfrac{1 - \cos\Delta\theta}{1 + \sin\theta \sin\Delta\theta - \cos\theta \cos\Delta\theta}, & \theta < \Delta\theta, \\ \dfrac{1 - \cos\Delta\theta}{2\sin\theta \sin\Delta\theta}, & \theta \geq \Delta\theta. \end{cases} \tag{154}$$

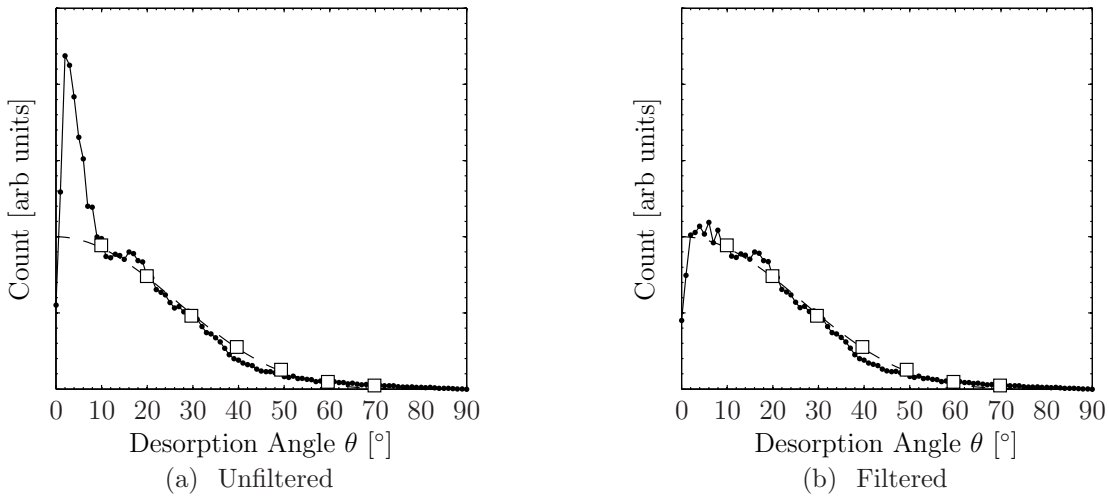

Figure 16. Distribution of desorption angle θ with respect to the surface normal for H_2-Cu(100) at T_s = 1100 K. Simulation results are compared with experiment and a curve fit to experimental data. The sampling is from 500k trajectories. Dashed curve, $\cos^d(\theta)$ with $d = 5$; □, experimental data; —, simulation results. Experimental data are from Reference [12], Figure 3. Differs from Figure 17 by $(A_{\mathrm{cap}}/A_{\mathrm{band}})^{-1}$ in Equation (154).

With the aid of Equation (154), desorption angle results are compared in Figure 16(a) to experimental values taken at $T_s = 1100$ K. As discussed in Section 3.6.4, contributing TS locations were determined by optimizing the fit of simulation results at $T_s = 1100$ K to the experimental data. Figure 16(a) illustrates how well desorption data can be duplicated by this method and the Wiesenekker PES. The dashed curve represents a curve fit to experimental data of the form $\cos^d(\theta)$ with $d = 5$. A cosine distribution ($d = 1$) would occur with complete thermalization of the molecules to the surface temperature if there were no surface corrugation. However, a corrugated PES alters the distribution from that of a pure cosine. Thus, even though the molecule is assumed to be fully thermalized to the surface temperature, the a cosine distribution is still not observed due to the PES.

Simulation results match well the experimental data points in Figure 16(a), except for desorption angles below 10.5°. A desorption peak is predicted at 2° from the normal, a feature not shown by the experimental measurements. Further des-

Table 3. Filtering ratios for desorption angles $\theta \leq 10.5°$.

Range [°]	Filtering Ratio	Range [°]	Filtering Ratio
$[0.5, 1.5)$	0.773	$[5.5, 6.5)$	0.644
$[1.5, 2.5)$	0.456	$[6.5, 7.5)$	0.802
$[2.5, 3.5)$	0.467	$[7.5, 8.5)$	0.798
$[3.5, 4.5)$	0.515	$[8.5, 9.5)$	0.942
$[4.5, 5.5)$	0.594	$[9.5, 10.5)$	0.938

orption experiments would need to be conducted to determine whether or not that peak is physical. There is no indication in the literature that such a peak has been found before. However, measurements are typically reported at large intervals due to limitations in the experimental equipment (i.e. 10°, 20°, etc.), so that if a peak does exist near 2°, it would not have been found unintentionally. However, the peak appears to be non-physical and simply represents a limitation of the current method. One could mitigate this peak in engineering applications by randomly rejecting excess molecules. To illustrate this possibility, consider a molecule desorbing with an angle between 1.5° and 2.5°. Since the experimental curve-fit value at $\theta = 2°$ is 45.6% of the predicted value in Figure 16(a), randomly accept (reject) the molecule. Choose a uniform random number R between 0 and 1. If $R \leq 0.456$, then accept the trajectory. Otherwise, reject it and calculate a new trajectory. The desorption angle ranges and ratios of experimental to predicted values are listed in Table 3. Note that since the results in Figure 16(a) are binned with a bin width of 1°, the desorption angle ranges have a width of 1° and are centered at integer values.

Figure 16(b) shows the modified desorption angle results with the accept-reject criteria taken into account for desorption angles $\theta \leq 10.5°$. Less than 4% of the trajectories are rejected. Even though it appears that a much higher percentage of molecules would need to be filtered when comparing Figures 16(a) and 16(b), recall

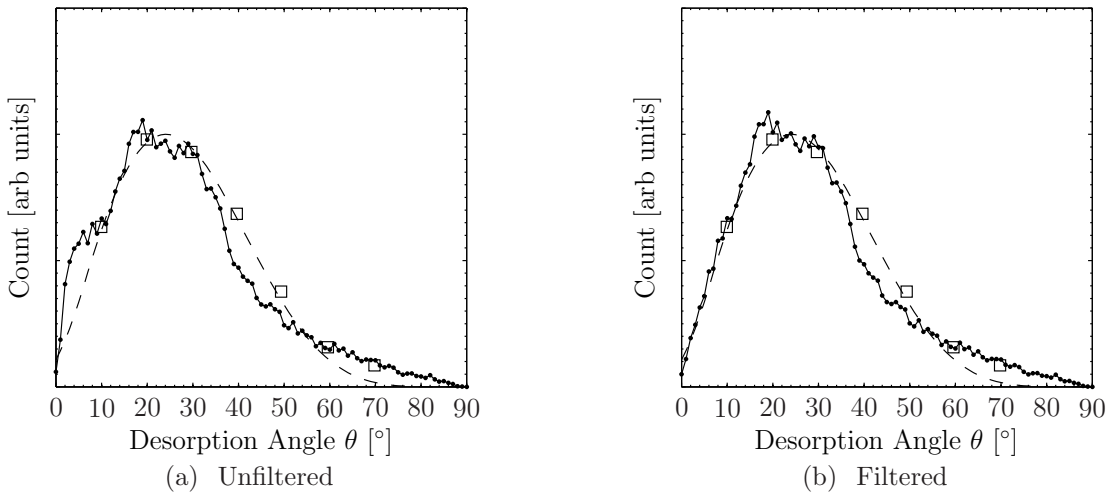

Figure 17. Raw distribution of desorption angle θ with respect to the surface normal for H_2-Cu(100) at $T_s = 1100$ K. Simulation results are compared with experiment and a curve fit to experimental data. The sampling is from 500k trajectories (unfiltered) and 481k (filtered). Dashed curve, $\cos^d(\theta)$ with $d = 5$; □, experimental data; —, simulation results. Experimental data are from Reference [12], Figure 3. Differs from Figure 16 by $A_{\mathrm{cap}}/A_{\mathrm{band}}$ in Equation (154).

that simulation values are modified per Equation (154) before they are compared with experimental data. Thus, the predicted raw count is only modified by less than 4%. This idea is illustrated in Figure 17, where simulation results are presented in their raw count, while experimental results are modified by $(A_{\mathrm{cap}}/A_{\mathrm{band}})^{-1}$ in Equation (154). Figures 16 and 17 contain identical data, just presented in a different manner. The filtering effect in Figure 17(b) is only for desorption angles $\theta \leq 10.5°$, where it is clear that only a small portion (less than 4%) of the trajectories are filtered out.

The remaining figures will be presented with filtering taken into account. Energy distributions see less than a 2% change (see Figures 18 and 19) and less than a 9% change (see Figure 20) when filtering is applied. More variability is seen in the translational energy distributions than in the mean translational energy values due to mathematical averaging. Likewise, the quadrupole alignment parameter $A_0^{(2)}$ experiences less than a 3% change over its entire range (see Figures 21, 22, and 23).

3.9.2 Energy Distributions.

The average translational energy of desorbing H_2 is shown in Figure 18 as a function of the rotational number J for two different vibrational numbers ($n_v = 0, 1$), where J and n_v are calculated by rounding to the nearest integer. Simulations predict lower average kinetic energies than is observed in experiments (0.28 eV for $n_v = 0$, and 0.15 eV for $n_v = 1$). This result is to be expected due to how the calculations are conducted. Recall that the Wiesenekker PES was constructed from MD simulations of hydrogen already adsorbed to the copper surface. However, in the experiments the hydrogen adlayer was populated via permeation through the bulk. Thus, either the PES needs to be constructed taking into account the absorption energy barrier, or vibrational-phonon coupling should be modeled to more accurately predict desorption energies. Figure 18(a) presents the simulation data without the absorption barrier energy, while Figure 18(b) includes the absorption barrier energy. Predictions match experiment with excellent agreement. The one questionable data point is at $J = 3$, where experimental measurements show a sudden drop in the mean translational energy. Sementa et al. [158] provide no explanation for the abnormal data point, so that one is left to conclude that it was an unexpected measurement.

Since simulations are able to recreate the shape of the experimental curves in Figure 18(b) for both vibrational and rotational numbers, the absorption barrier is shown here to primarily affect the translational energy of the desorbing gas, and then only as a function of the vibrational energy. For engineering applications, one can take an upper-limit approach, assuming that the absorption barrier contribution is a constant value for all vibrational numbers. Since there is no vibrational-phonon coupling for $n_v = 0$, the value found here (0.28 eV) can serve as that upper limit. The absorption barrier is equivalent to the solubility energy E_S in Equation (143), and the value of 0.28 eV falls within the published range for E_S [153]. Vibrational-

phonon coupling may explain why the absorption barrier energy contribution is less for $n_v = 1$ than for $n_v = 0$.

Since the absorption barrier energy mainly affects the mean translational energy, it is reasonable to conclude that adatoms receive this additional energy in a similar manner. On average, the adatoms receive the additional energy in the x-, y-, and z-directions in equal proportion to each other. In other words, the absorption barrier energy accelerates both adatoms in the same direction before they arrive at the TS location.

Some researchers employ GW, which rejects trajectories that have vibrational energies far from quantum values, in order to achieve more realistic statistics from their Monte Carlo simulations [23; 24; 131]. However, it was found in this research that GW is not required.

Figure 18(b) is a key result of this work. One of the original goals of modeling thermal desorption in DSMC was to accurately predict internal and translational energy distributions. Up until now, no research effort has been able to accomplish this feat, especially without GW. Therefore, this work provides an engineering alternative to time-intensive MD and DFT calculations.

The average total energy is presented in Figure 19, shown as a function of both n_v and J. The average total energy of desorbing molecules actually increases with increasing J. This result indicates that two desorbing molecules with the same initial total energy will transfer different energy amounts to the surface, depending on their rotational energy. Thus, molecules with lower (final) rotational energies tend to transfer more energy to the surface than those with higher (final) rotational energies.

The translational energy distributions for $(n_v = 0, J = 1 - 9)$ are shown in Figure 20. As the rotational number increases, the distribution changes from unimodal $(J = 1 - 2)$, to bimodal $(J = 3 - 7)$, and then back to unimodal $(J = 8 - 9)$. In

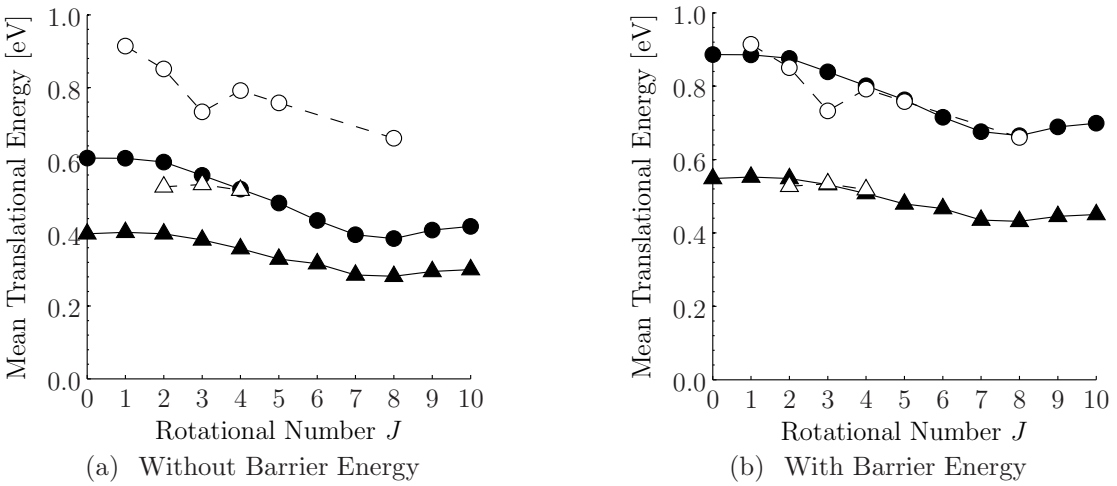

(a) Without Barrier Energy (b) With Barrier Energy

Figure 18. State-resolved mean translational energy of desorbing H_2 from Cu(100) at $T_s = 1030$ K. The sampling is from a total of 1M trajectories (600k for $n_v = 0$, 213k for $n_v = 1$). Simulation results are shown with filled symbols (● for $n_v = 0$, ▲ for $n_v = 1$), while experimental values are shown in open symbols (○ for $n_v = 0$, Δ for $n_v = 1$), taken from Reference [158], Figure 9. Simulations predict a lower mean translational energy due to the energy barrier a hydrogen atom experiences when migrating from the bulk to the surface of copper. The simulation curves are therefore adjusted upwards in (b) to illustrate this effect (0.28 eV for $n_v = 0$, and 0.15 eV for $n_v = 1$). Vibrational-phonon coupling explains why the energy barrier contribution is less for $n_v = 1$ than for $n_v = 0$.

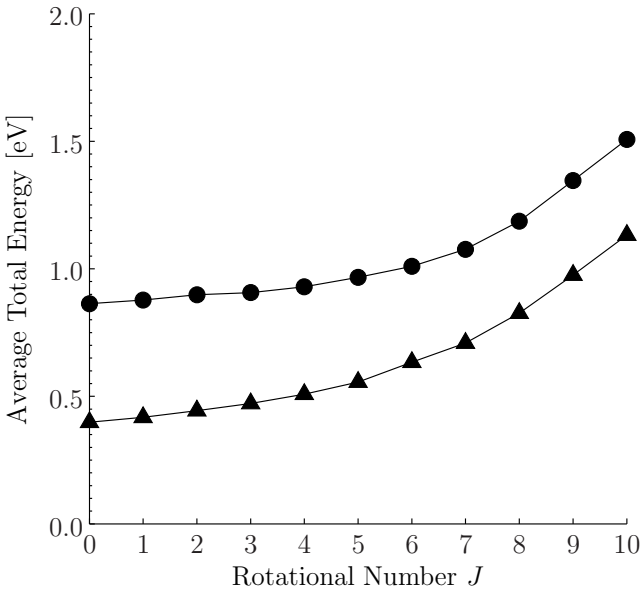

Figure 19. State-resolved total energy of desorbing H_2 from Cu(100) at $T_s = 1030$ K from simulations. The sampling is from 600k trajectories for $n_v = 0$ (●), and 213k trajectories for $n_v = 1$ (▲). Total number of trajectories for all vibrational numbers is 1M. Total energy increases for increasing J, but decreases for increasing n_v.

comparing Figures 18 and 20, the average translational energy of the distributions is seen to decrease as J increases for most of the rotational numbers. The only exception is from $J = 8$ to $J = 9$, where the average translational energy increases with increasing J.

3.9.3 Rotational Alignment.

The predicted average rotational alignment of the molecule as it desorbs is also compared with experiment. The average rotational quadrupole alignment parameter $A_0^{(2)}$ is calculated in reference to the surface normal. For a given rotational number J, $A_0^{(2)}$ is defined as [39; 131; 182:Chap. 5, Application 13],

$$A_0^{(2)}(J) = \left\langle 3\cos^2\Xi - 1 \right\rangle_J , \tag{155}$$

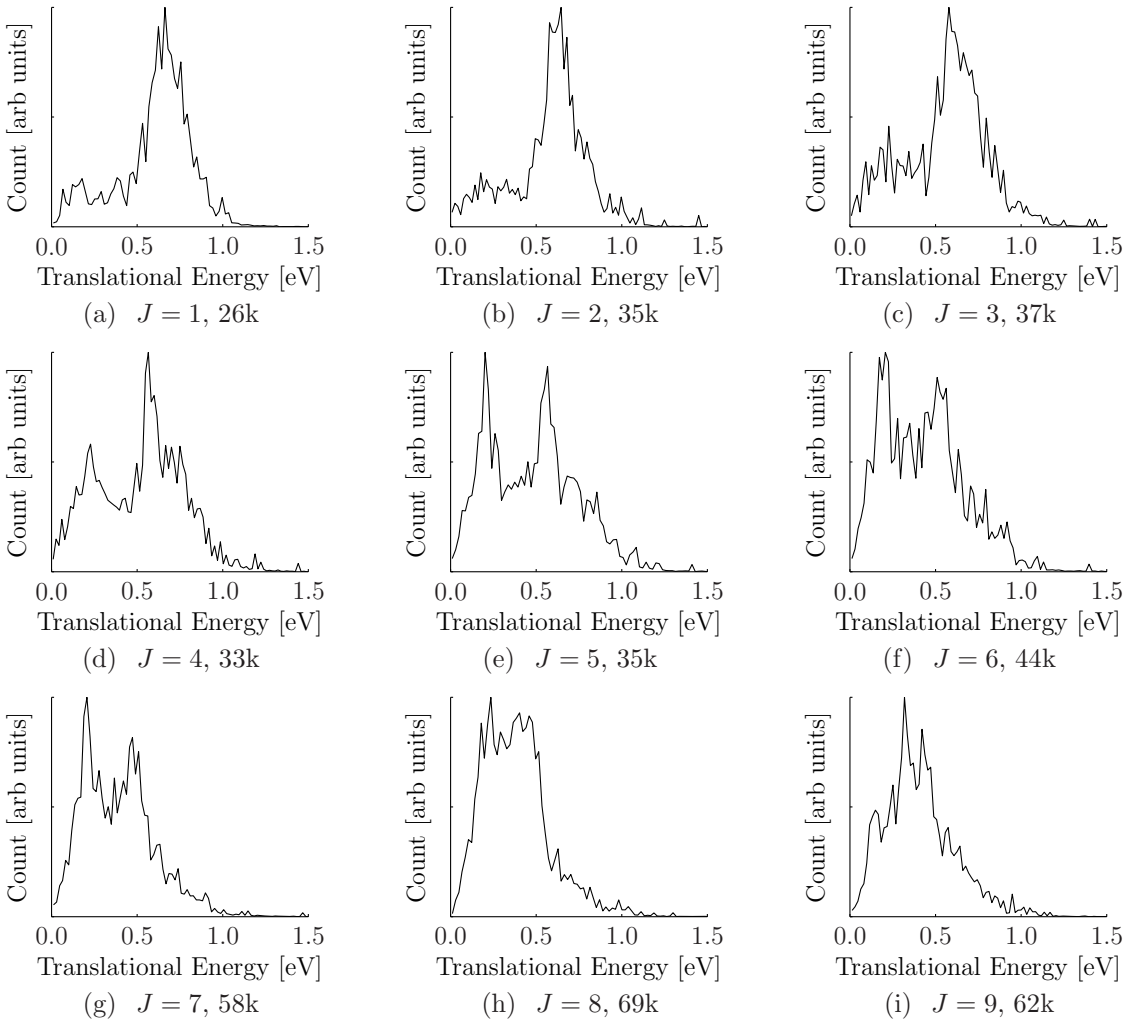

Figure 20. Translational energy distributions for states ($n_v = 0, J = 1 - 8$) of H_2 desorbing from Cu(100) at $T_s = 1030$ K from simulations. Taken from a sampling of 1M trajectories. The rotational number J and the number of trajectories at each state are listed in the subcaptions. The absorption barrier energy is not included in simulations. As the rotational number J increases, the distributions transition from unimodal ($J = 1 - 2$) to bimodal ($J = 3 - 7$) and then back to unimodal ($J = 8 - 9$).

where Ξ is the angle between the z-axis and the rotational angular momentum vector $\mathcal{J}$,

$$\cos \Xi = \frac{\mathcal{J}_z}{\mathcal{J}}, \tag{156}$$

$\mathcal{J}_z$ is the z-component of the angular momentum, and the brackets $\langle \cdot \rangle_J$ denote taking the average for all molecules that have that value for J once desorbed. $A_0^{(2)}$ is valid in the range $A_0^{(2)} \in [-1, 2]$, with -1 indicating that the molecules desorb in a completely cartwheel motion, 2 indicating that they desorb with a helicopter motion, and any other value indicating a combination of these two motions.

The z-component $\mathcal{J}_z$ is easily calculated in Cartesian coordinates. The angular momentum for a molecule is the sum of the cross-products of the radius vector $\boldsymbol{r}_i$ and the momentum vector $\boldsymbol{p}_i$ for each atom i,

$$\boldsymbol{\mathcal{J}} = \sum_{i=1}^{n} \boldsymbol{\mathcal{J}}_i \tag{157}$$

where n is the number of atoms in a molecule (2 in this case), and the angular momentum for the ith atom is

$$\boldsymbol{\mathcal{J}}_i = \boldsymbol{r}_i \times \boldsymbol{p}_i, \tag{158}$$

where $\boldsymbol{r}_i$ begins at the molecule's center of mass and terminates at atom i, and $\boldsymbol{p}_i$ is the linear momentum of the ith atom. The z-component of $\mathcal{J}$ is then

$$\mathcal{J}_z = \sum_{i=1}^{n} \mathcal{J}_{z,i}, \tag{159}$$

where the z-component of angular momentum for the ith atom $\mathcal{J}_{z,i}$ is

$$\mathcal{J}_{z,i} = r_{x_i} p_{y_i} - r_{y_i} p_{x_i}, \tag{160}$$

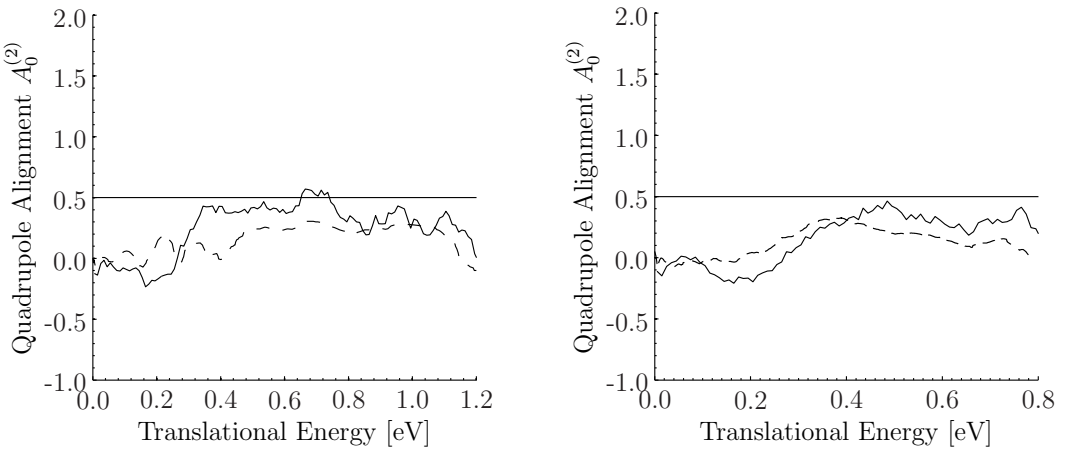

(a) $(n_v = 0, J = 4)$, 30k Trajectories (b) $(n_v = 1, J = 2 \text{ to } 4)$, 27k Trajectories

Figure 21. Quadrupole alignment parameter $A_0^{(2)}$ as a function of the translational energy of the desorbing gas H_2 from Cu(100) for states $(n_v = 0, J = 4)$ and $(n_v = 1, J = 2 - 4)$ at $T_s = 1030$ K. The sampling is from 1M total trajectories. The solid lines represent simulation results, while the dashed lines represent experimental values from Reference [158], Figure 6. The lines are both calculated with a ten-point moving average of the raw data. In (b), the average value of $A_0^{(2)}$ is given over the rotational numbers considered. Helicopter motion is indicated by $A_0^{(2)} = 2$, and cartwheel motion by $A_0^{(2)} = -1$. The horizontal solid line is for reference only. Simulation values match experiment fairly well.

where $r_{x_i} = x_i - x$ and $r_{y_i} = y_i - y$ [see Equations (87)-(88)], and p_{x_i} and p_{y_i} are the x- and y-components of momentum for the ith atom, respectively.

The quadrupole alignment parameter $A_0^{(2)}$ provides a measure of how well the physics are represented by the simulation. It indicates how the molecules are oriented as they rotate in space. Even though $A_0^{(2)}$ may not be beneficial in engineering codes, it is discussed here to validate the model. As shown in Figure 21, the model performs well when compared against experiment. The predicted curves follow experiment qualitatively, and are within 15% and 12% for $(n_v = 0, J = 4)$ and $(n_v = 1, J = 2 \text{ to } 4)$, respectively. The molecules tend to desorb with more of a cartwheel than helicopter motion.

Figure 22 shows the average quadrupole alignment parameter $A_0^{(2)}$ for the ground vibrational state $n_v = 0$ at various rotational numbers. Except for $J = 8$, predictions

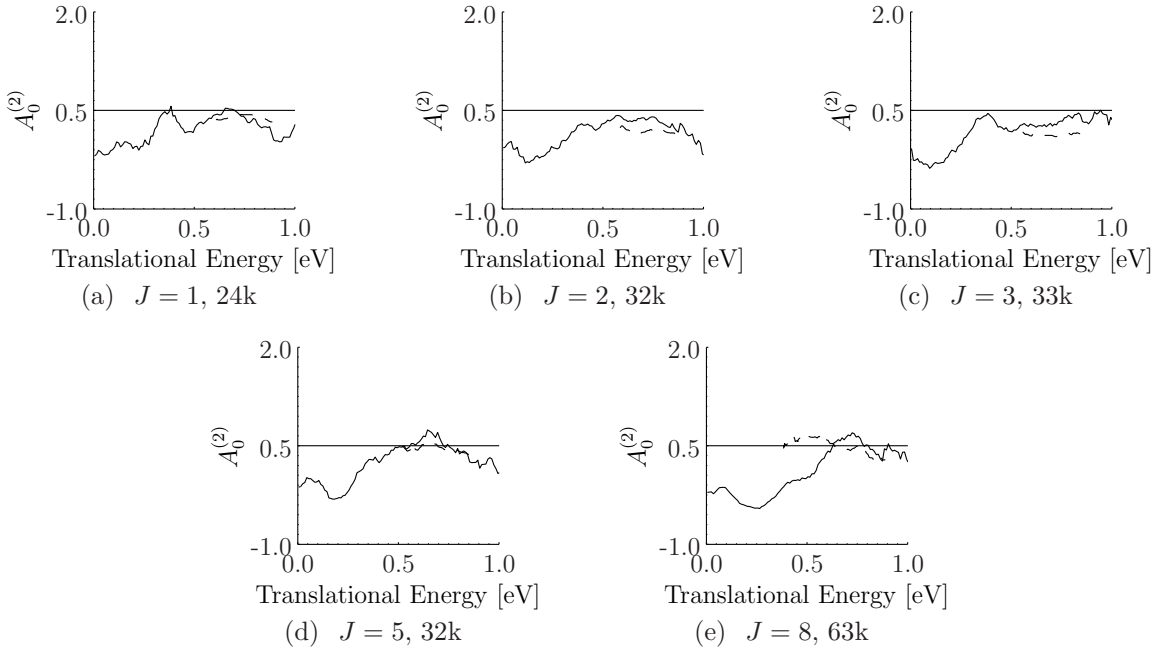

Figure 22. Quadrupole alignment parameter $A_0^{(2)}$ as a function of the translational energy of the desorbing gas H_2 from Cu(100) for states ($n_v = 0, J = 1, 2, 3, 5, 8$) at $T_s = 1030$ K. The sampling is from a total of 1M trajectories. The rotational number J and the number of trajectories are given in each subcaption. The solid lines represent simulation results, while the dashed lines represent experimental values from Reference [158], Figure 14. The lines are both calculated with a ten-point moving average of the raw data. Helicopter motion is indicated by $A_0^{(2)} = 2$, and cartwheel motion by $A_0^{(2)} = -1$. The horizontal solid line is for reference only. Simulation values match experiment very well, except for a portion of the plot from state ($n_v = 0, J = 8$).

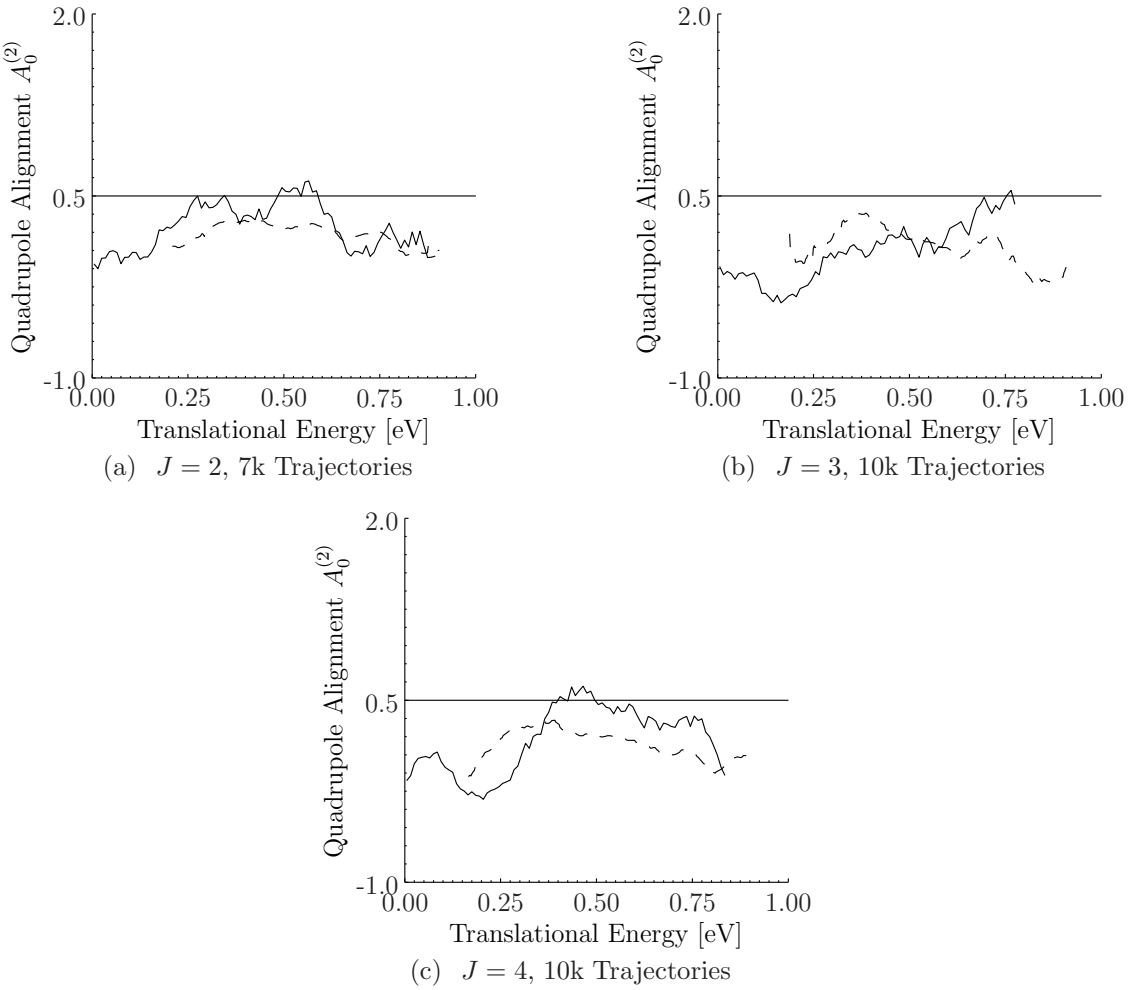

(a) $J = 2$, 7k Trajectories

(b) $J = 3$, 10k Trajectories

(c) $J = 4$, 10k Trajectories

Figure 23. Quadrupole alignment parameter $A_0^{(2)}$ as a function of the translational energy of the desorbing gas H_2 from Cu(100) for states ($n_v = 1, J = 2-4$) at $T_s = 1030$ K. The sampling is from a total of 1M trajectories. The rotational number J and the number of trajectories are given in each subcaption. The solid lines represent simulation results, while the dashed lines represent experimental values from Reference [158], Figure 15. The lines are both calculated with a ten-point moving average of the raw data. Helicopter motion is indicated by $A_0^{(2)} = 2$, and cartwheel motion by $A_0^{(2)} = -1$. The horizontal solid line is for reference only. There is a decent match between simulation values and experiment.

agree well with experimental values. The maximum difference between the two are 7% ($J = 1$), 8% ($J = 2$), 10% ($J = 3$), 7% ($J = 5$), and 22% ($J = 8$). Cartwheel motion is favored for the most part. For $J = 8$, the model predicts more pronounced cartwheel motion than experiment.

In general, the trend appears to favor cartwheel motion for low translational energy values. As the translational energy increases, the motion on average has an equal contribution of cartwheel and helicopter motion. An explanation for this may be that at low translational energies, the desorbing molecules are influenced much more by the PES than at high translational energies. As the molecule desorbs, it experiences a longer residence time on the surface for a low translational energy. Therefore, the PES has a greater influence on the molecule's orientation. On the other hand, a molecule with a high translational energy spends a shorter amount of time being influenced by the PES, and so its orientation is much more dependent on the molecule's initial conditions.

For $n_v = 1$, Figure 23 presents $A_0^{(2)}$ as a function of translational energy. This vibrational state is less populated than the ground state. Hence the statistics in Figure 23 have a higher variability than is seen in Figure 21. In spite of the fact that fewer trajectories are represented in Figure 23, general trends can still be assessed. Predictions follow experimental data well qualitatively, even though quantitatively there is some deviation. The model shows a maximum difference from experiment of 12% for $J = 2$, 19% for $J = 3$, and 14% for $J = 4$.

3.10 Chemisorption Summary

A new and successful model for thermal desorption was developed in this chapter. It can be directly incorporated into Direct Simulation Monte Carlo codes as a boundary condition. Appropriate timing has been introduced as well so that non-

equilibrium, temporally-accurate simulations can be conducted. A typical activated chemisorption system, H_2-Cu(100), was used to demonstrate the novel method. However, this work is not limited to hydrogen nor to copper. It is expected that thermal desorption due to the Langmuir-Hinshelwood reaction on any gas-surface system can be modeled with the same techniques.

At least seven significant contributions to the state-of-the-art have been developed in this research. Thermal desorption modeling is now available for engineering applications, to include desorption angle, internal energies, translational energy, and the molecular alignment. Accurate temporal modeling in Direct Simulation Monte Carlo has been introduced. The equations of motion have been presented in a non-dimensionalization scheme, something not found in the literature. The new model is not limited by the number of transition states it can consider. In fact, this research has shown that many transition states should be identified to provide accurate results. Initial conditions were determined from a truncated Maxwell-Boltzmann distribution, developed here with its accompanying accept-reject form. Gaussian weighting, a filtering scheme which greatly increases run times, has been shown here to be unnecessary under the proposed model. Finally, this research has clearly shown that the absorption barrier energy from permeation not only significantly contributes to the translational energy of desorbing molecules, but it also has little effect on their rotational and vibrational energies.

IV. Conclusions

Surface processes are varied and complex, and exhibit unique behaviors for different gas-surface systems. There is a need to be able to simulate these processes for a wide variety of systems with engineering methods. This work has sought to address that need by applying the Direct Simulation Monte Carlo framework to the areas of adsorption and desorption in physisorptive and chemisorptive systems, respectively, something that has not been accomplished until now.

For adsorption, the Xe-Pt(111) system was chosen as representative of a typical physisorptive system. Building on the Cercignani-Lampis-Lord scattering kernel and the Multi-Stage scattering model, a new method, the Modified Kisliuk with Scattering method, was successfully developed for calculating adsorption probabilities and scattering properties. The results show that, for the Xe-Pt(111) system, this method was able to accurately predict adsorption probabilities as a function of coverage, even for a gas-surface system where adsorption probabilities increase with increased coverage.

The Modified Kisliuk with Scattering method is applicable to any gas-surface physisorption system. Thus, even though the Xe-Pt(111) system was investigated here, any combination of a gas and surface can be applied, as long as the bond is physisorptive in nature.

One could also extend this method to include non-physisorptive systems by assuming that no chemical reactions occur. In other words, one could assume that gas molecules only scatter or adsorb in relation to a surface, without the presence of dissociation, recombination, or other chemical reactions. In engineering applications where quick calculations are required, this assumption could provide reasonable results. Or, a comparison with experimental results could illustrate the effects due to chemical reactions alone. In this manner, the contributions made by surface chemical effects could be uncoupled from those made by scattering and adsorption.

The Modified Kisliuk with Scattering method dramatically improves the scattered translational energy profile. Experimental data show that for some scattering angles, the incident molecules actually gain energy. The Cercignani-Lampis-Lord kernel alone cannot predict this behavior. However, with the new method, this super-elastic scattering behavior can be predicted.

The scattering angle distribution is also improved by the Modified Kisliuk with Scattering method over the traditional Cercignani-Lampis-Lord kernel. Experimental distributions of Xe-Pt(111) are tighter than the kernel can predict. The new method easily tightens the scattering distribution, providing more realistic predictions.

For the first time, the Cercignani-Lampis-Lord kernel was applied here to scattering off of an adlayer. This work has shown that precursor-mediated gas-adlayer interactions can be predicted by the kernel, as incorporated into the new method. Previously, work with the Cercignani-Lampis-Lord kernel has been confined to the gas scattering off of the primary surface.

Optimal values for the accommodation coefficients were found with the new method by comparing the predictions with experiment. The Modified Kisliuk with Scattering method thus provides an additional mean for determining these coefficients, for use both with the Cercignani-Lampis-Lord kernel, as well as other scattering models.

For thermal desorption, the H_2-Cu(100) system was chosen as the prototypical chemisorptive system with activated desorption. Classical trajectory methods on a six-dimensional potential energy surface were incorporated with Keck's method to efficiently calculate desorption parameters (desorption angle, molecular alignment, and translational, rotational, and vibrational energies). The equations were non-dimensionalized in order to reduce numerical error. Relevant transition states, found with the Chain algorithm, were weighted according to their relative contributions to the desorption angle. Initial conditions at the transition states were determined with

a truncated Maxwell-Boltzmann distribution. A method for conducting temporally-accurate simulations is developed, by taking into account appropriate event timing and permeation.

Many contributions to the state-of-the-art were developed in this work. First, non-dimensionalized classical trajectory equations were derived here. Nowhere in the literature were the equations of motion found to be non-dimensionalized. This fact is surprising since non-dimensionalization can greatly reduce numerical error.

Previous researchers have limited Keck's method to only one transition state. However, this work has shown that it is beneficial to consider all contributing transition states. Each location contributes in a different manner to the final results, with unique angular and energy distributions. This novel approach proved here to improve classical trajectory modeling.

The trunctated Maxwell-Boltzmann distribution was developed here, along with its accept-reject form. The final trajectories are heavily dependent upon initial conditions. Therefore, the truncated Maxwell-Boltzmann distribution is necessary for Keck's method.

Temporally-accurate desorption modeling also requires correct event timing. In the literature, it has been known for many years how to correctly time desorption events in Monte Carlo simulations. However, Direct Simulation Monte Carlo has never before incorporated this technique. With a few modifications, event timing has been developed as a part of this research for use with Direct Simulation Monte Carlo.

It is common in classical trajectory modeling to require Gaussian weighting, which weights results based on how closely their classical vibrational energies align with quantum values. Unfortunately, in Direct Simulation Monte Carlo applications, Gaussian weighting would dramatically increase simulation run times. This work has demonstrated that Gaussian weighting is not always necessary in classical trajectory

simulations. Perhaps Gaussian weighting is not required here because of the other significant contributions. In other words, it is possible that the physics are so well modeled in this research, that one does not need to take a quasi-classical trajectory approach here.

Finally, there has been some discussion in the literature as to how much, or in what manner, the absorption barrier energy contributes to thermal desorption. This debate is especially relevant since many desorption experiments rely on permeation to supply hydrogen to the surface. The research conducted here has shown that the absorption energy barrier contributes significantly to the translational energy of desorbing molecules. Predictions of desorption influenced by permeation and diffusion must therefore include the absorption energy barrier. In addition, it has been shown here that this barrier has little impact on the final rotational and vibrational energies of desorbing molecules.

Even though desorption results are discussed in reference to the H_2-Cu(100) gas-surface system, any chemisorptive system with a Langmuir-Hinshelwood mechanism could be applied to the thermal desorption model. Hence this work is universal in nature for all similar systems. The results, of course, will depend heavily on the accuracy of the potential energy surface chosen (or developed) to describe the gas-surface interactions. However, with an accurate potential energy surface, the physics of thermal desorption can be simulated for any similar system. Besides, other systems with different mechanisms can still utilize the novel non-dimensionalization scheme presented here, since the non-dimensionalization is universal for any classical or quasi-classical trajectory method.

There are many avenues one could take in furthering the thermal desorption research presented here. One path forward would be to include adsorption and scattering modeling for a chemisorptive system. Since desorption is the microscopically-

inverse process of adsorption, it would not be difficult to do so. Initial conditions for scattering and adsorption would actually be simpler to define than for desorption because in a Direct Simulation Monte Carlo simulation, one would know translational and internal energies of impinging molecules. One could then follow the molecule from the gas phase as it interacts with the solid via the potential energy surface. If the molecule reverses course and travels back to the gas domain, then it scatters. Otherwise, it adsorbs to the surface. In this manner, scattering distributions could be determined, to include angular, translational, rotational, and vibrational. In addition, adsorption probabilities could be calculated. Implementing adsorption and scattering into Direct Simulation Monte Carlo would then be straightforward and beneficial.

Besides directly modeling adsorption and scattering for a chemisorptive gas-surface system, this research could be extended by considering any of the other surface-effect mechanisms. These chemical pathways include Eley-Rideal, field-induced, ion-induced, photo-induced, and electron-stimulated desorption. An entire suite of relevant surface effects could be constructed over time to provide accurate modeling in Direct Simulation Monte Carlo applications. For example, in the field of laser-surface effects, photo-induced desorption and ablation is a field of considerable interest. Perhaps similar methods to those presented in this work could be developed to accurately model dynamic laser-surface interactions.

Eley-Rideal desorption is another promising mechanism that could be investigated. Instead of modeling two adsorbed atoms on the surface, one could model a single adatom and a gas-phase atom. Initial conditions for the adatom could be taken from a Maxwell-Boltzmann distribution at the surface temperature. For the gas-phase atom, its initial conditions would be known from its previous interactions and collisions within the Direct Simulation Monte Carlo program. One would need to

determine how Keck's method would apply under these conditions, if at all. Also, a different potential energy surface would need to be created, or found in the literature.

Electron-stimulated desorption would also be a fascinating topic to address. In high-power microwave applications, electron-stimulated desorption plays a role in contaminating the plasma and inducing pulse-shortening. One could model electron-stimulated desorption in the following manner. Take an impinging electron whose velocity is known. The electron excites a surface adatom (or admolecule) to some degree. Then that adatom travels under the influence of the potential energy surface to either desorb, or to remain on the surface, albeit at a new location. A challenge here would be to incorporate current electron-stimulated desorption theory into a Direct Simulation Monte Carlo framework, and then to efficiently model the desorption of the excited adatom.

Ablation is another natural extension of this work. Similar to activated desorption, ablation requires the overcoming of an energy barrier. Even though there would be imperfections in a real surface undergoing ablation (e.g. steps) one could begin modeling ablation by assuming that each ablation event occurs under the same conditions. For example, each ablation event could be assumed to result from a surface atom on a perfectly-clean surface with no imperfections. Ablation would be induced by energy deposition, originating from collisions with the surface or conductive heating. Ablation could therefore be considered, at least at first, as a temperature-dependent process. Initial conditions of an ablating atom would then come from a Maxwell-Boltzmann distribution at the (local) surface temperature.

In conclusion, this research both significantly contributes to the state-of-the-art, and lays a solid foundation for future developments in surface-effects modeling for Direct Simulation Monte Carlo applications. The effects investigated here (scattering, adsorption, and Langmuir-Hinshelwood thermal desorption) represent only a subset

of the many mechanisms by which a gas interacts with a solid. Other important mechanisms that could be investigated in future work are Eley-Rideal desorption, electron-stimulated desorption, and ablation. By modifying and building upon the approaches developed here, the successful modeling of other surface effects could also be accomplished and incorporated into Direct Simulation Monte Carlo applications.

Appendix A. List of Symbols

Symbol	*Definition*
a	Average equilibrium length of the unit cube [Å],
	Fitting coefficient for V_{rep} [eV]
	Variable in the generalized quadratic formula [$*$]
	Outer radius [m]
a_0	Bohr radius [0.529 Å]
a_1	Fitting coefficient for V_{att} [Å^{-1}]
a_2	Fitting coefficient for V_{att} [Å^{-2}]
a_3	Fitting coefficient for V_{att} [Å^{-3}]
a_4	Fitting coefficient for V_{att} [Å^{-1}]
a_l	Average equilibrium length of the unit cuboid [Å]
a_Q	Accommodation coefficient for property Q [$*$]
A	Area of the surface unit cell [Å^2]
$\boldsymbol{A}$	Unit vector of a link [$*$]
	Fluxal area [m^2]
$A_0^{(2)}$	Average quadrupole alignment parameter [$*$]
A_1	BR potential adjustable parameter [kJ mol^{-1}]
A_{band}	Surface area of a spherical, latitudinal band [m^2]
A_{cap}	Surface area of a spherical cap [m^2]
A_g	BR potential adjustable parameter [kJ mol^{-1}]

Symbol	*Definition*
b	Fitting coefficient for V_{rep} [Å^{-1}]
	Variable in the generalized quadratic formula [$*$]
	Inner radius [m]
b_j	α_j-intercept in the $\alpha_1\alpha_j$-plane [m]
c	Incident velocity [m s^{-1}]
	Variable in the generalized quadratic formula [$*$]
c_0	Fitting coefficient for the three-body potential [eV]
c_1	Fitting coefficient for the three-body potential [eV Å^{-1}]
c_{11}	Fitting coefficient for the three-body potential [eV Å^{-2}]
c_{111}	Fitting coefficient for the three-body potential [eV Å^{-3}]
c_{1111}	Fitting coefficient for the three-body potential [eV Å^{-4}]
c_{11111}	Fitting coefficient for the three-body potential [eV Å^{-5}]
c_{11112}	Fitting coefficient for the three-body potential [eV Å^{-5}]
c_{1112}	Fitting coefficient for the three-body potential [eV Å^{-4}]
c_{11122}	Fitting coefficient for the three-body potential [eV Å^{-5}]
c_{112}	Fitting coefficient for the three-body potential [eV Å^{-3}]
c_{1122}	Fitting coefficient for the three-body potential [eV Å^{-4}]
c_{11222}	Fitting coefficient for the three-body potential [eV Å^{-5}]
c_{12}	Fitting coefficient for the three-body potential [eV Å^{-2}]
c_{122}	Fitting coefficient for the three-body potential [eV Å^{-3}]
c_{1222}	Fitting coefficient for the three-body potential [eV Å^{-4}]

Symbol	*Definition*
c_{12222}	Fitting coefficient for the three-body potential [eV Å^{-5}]
c_2	Fitting coefficient for the three-body potential [eV Å^{-1}]
c_{22}	Fitting coefficient for the three-body potential [eV Å^{-2}]
c_{222}	Fitting coefficient for the three-body potential [eV Å^{-3}]
c_{2222}	Fitting coefficient for the three-body potential [eV Å^{-4}]
c_{22222}	Fitting coefficient for the three-body potential [eV Å^{-5}]
c_6	BR potential adjustable parameter [kJ Å^6 mol^{-1}]
c_n	Incident normal velocity [m s^{-1}]
c_n'	Post-collisional normal velocity [m s^{-1}]
c_t	Incident tangential velocity [m s^{-1}]
c_t'	Post-collisional tangential velocity [m s^{-1}]
$\langle c_t' \rangle$	Average post-collisional tangential velocity [m s^{-1}]
c_w	Wall velocity [m s^{-1}]
d	Membrane thickness [m]
	Exponent of curve fit, $\cos^d(\theta)$ [$*$]
d_0	Equilibrium distance between surface atoms [Å]
dA	Infinitesimal area in the geometric representation of CLL [$*$]
dE	Infinitessimal total energy [J]
dE^*	Infinitessimal (non-dimensionalized) total energy [$*$]
du'	Infinitessimal post-collisional tangential velocity component [m s^{-1}]
dv'	Infinitessimal post-collisional tangential velocity component [m s^{-1}]

Symbol	*Definition*
dw'	Infinitessimal post-collisional normal velocity component [m s^{-1}]
D	Diffusion coefficient [m^2 s^{-1}]
D_0	Maximum diffusion coefficient [m^2 s^{-1}]
$\boldsymbol{D}$	Step direction [$*$]
D_e	Fitting coefficient for V_{att} [eV]
E	Total energy [J]
E_{ads}	Energy of adsorption [kJ mol^{-1}]
E_D	Activation energy for diffusion [J]
E^*_{max}	Discrete approximation for $+\infty$ [$*$]
E_S	Activation energy for solubility [J]
E'_{tot}	Post-collisional total energy [kJ mol^{-1}]
E_{tr}	Incident translational energy [kJ mol^{-1}]
E'_{tr}	Post-collisional translational energy [kJ mol^{-1}]
$E'_{\text{tr},n}$	Post-collisional normal translational energy [kJ mol^{-1}]
$E'_{\text{tr},t}$	Post-collisional tangential translational energy [kJ mol^{-1}]
E_Φ	Activation energy for permeability [J]
f	Fugacity [Pa]
f_c	Switching function [$*$]
f_d	Switching function [$*$]
f_E	MB energy distribution [J^{-1}]
f_{E^*}	MB (non-dimensionalized) energy distribution [$*$]

Symbol	*Definition*
$f_{\max}$	Maximum value of f_{TS} [$*$]
f_t	Probability density of times between successive events [$*$]
f_{TS}	Truncated MB (non-dimensionalizd) energy distribution [$*$]
f'_{TS}	f_{TS} normalized by $f_{\max}$ [$*$]
$\boldsymbol{g_0}$	Gradient of V at $\boldsymbol{q_0}$ [J m^{-1}]
$\boldsymbol{g_0^i}$	$\boldsymbol{g_0}$ at step i [J m^{-1}]
g_0^k	k^{th} element of $\boldsymbol{g_0}$ [J m^{-1}]
g_1	Pre-convergence threshold parameter [J m^{-1}]
g_c	Threshold parameter [J m^{-1}]
G	Cyclic parameter [Å^{-1}]
$G(r)$	Damping function [$*$]
$\boldsymbol{G}$	Negative gradient of V at $\boldsymbol{p_H}$ [J m^{-1}]
$\boldsymbol{G}^*$	Projected gradient [J m^{-1}]
$\mathbf{G_0}$	Component of $\boldsymbol{g_0}$ along $\mathbf{U}$ [J m^{-1}]
h	Planck constant [6.626×10^{-34} J s]
	Height of cylinder [m]
h_s	BR potential adjustable height parameter [Å]
$\mathbf{H}$	Hessian matrix [J m^{-2}]
$\mathbf{H}_{\mathrm{new}}$	Current value of $\mathbf{H}$ [J m^{-2}]
$\mathbf{H}_{\mathrm{old}}$	Previous value of $\mathbf{H}$ [J m^{-2}]
$\mathbf{H}^*$	Non-dimensionalized Hessian matrix [$*$]

Symbol	*Definition*
$\mathbf{H'}$	Mass-weighted Hessian matrix [J kg^{-1} m^{-2}]
$\mathbf{H_0}$	$\mathbf{H}$ evaluated at $\boldsymbol{q_0}$ [J m^{-2}]
$\mathbf{H_0^i}$	$\mathbf{H_0}$ at step i [J m^{-2}]
$\mathcal{H}$	Hamiltonian [J]
$\mathcal{H}^*$	Non-dimensionalized Hamiltonian [$*$]
$H_0^{j,k}$	(j,k) element of $\mathbf{H_0}$ [J m^{-2}]
H_{00}	Plane-wave diffraction function [Å^{-1}]
H_{10}	Plane-wave diffraction function [Å^{-1}]
H_{11}	Plane-wave diffraction function [Å^{-1}]
$H_{B_1 10}$	Plane-wave diffraction function [Å^{-1}]
$H_{j,k}$	(j,k) element of $\mathbf{H}$ [J m^{-2}]
$H^*_{j,k}$	(j,k) element of $\mathbf{H^*}$ [$*$]
$H'_{j,k}$	(j,k) element of $\mathbf{H'}$ [J kg^{-1} m^{-2}]
H_v	Vibrational term of the Hamiltonian $\mathcal{H}$ [J]
$\hbar$	Reduced Planck constant [1.055×10^{-34} J s]
i	Imaginary number $\sqrt{-1}$ [$*$]
I	Reduced moment of inertia [kg m^2]
$\mathbf{I}$	Identity matrix [$*$]
I_0	Modified Bessel Function of the First Kind [$*$]
J	Rotational number [$*$]
$\boldsymbol{J}$	Flux of molecules [molecules s^{-1} m^{-2}]

Symbol	*Definition*
$\mathcal{J}$	Rotational angular momentum [kg m s^{-1}]
$\mathcal{J}^*$	Non-dimensionalized rotational angular momentum [$*$]
$\boldsymbol{\mathcal{J}}$	Rotational angular momentum vector [kg m s^{-1}]
$\boldsymbol{\mathcal{J}}_i$	Rotational angular momentum vector of atom i [kg m s^{-1}]
$\mathcal{J}_z$	z-component of $\mathcal{J}$ [kg m s^{-1}]
$\boldsymbol{\mathcal{J}}_{z,i}$	z-component of $\boldsymbol{\mathcal{J}}_i$ [kg m s^{-1}]
k	Boltzmann constant [8.315×10^{-3} kJ mol^{-1} K^{-1}],
	Boltzmann constant [1.381×10^{-23} J K^{-1}]
K	Factor in the Kisliuk adsorption model [$*$]
l_0	Threshold parameter [m]
l_1	Threshold parameter [m]
l_2	Threshold parameter [m]
$l_{2_{\text{new}}}$	Updated value of l_2 [m]
$l_{2_{\text{old}}}$	Previous value of l_2 [m]
$\mathcal{L}$	Lagrangian [J]
m	Molecular mass [Mg mol^{-1}],
	Mass of an atom [kg]
m_1	Mass of atom 1 [kg]
m_2	Mass of atom 2 [kg]
m_j	Slope of a line [$*$]
M	Total mass [kg]

Symbol	*Definition*
M_1	Starting configuration
M_2	Ending configuration
n_m	Exponent of the modified energy [$*$]
n_v	Vibrational number [$*$]
N	Number of atoms in the molecule [atoms]
	Number of adatoms [adatoms]
N_{colls}	Number of collisions [$*$]
$\boldsymbol{p^*}$	New point for replacing $\boldsymbol{p_H}$
$p'^*_{c,i}$	Non-dimensionalized MWC momenta [$*$]
$\boldsymbol{p_H}$	Approximate location of TS
$\boldsymbol{p_{H-1}}$	Path point adjacent to $\boldsymbol{p_H}$
$\boldsymbol{p_{H+1}}$	Path point adjacent to $\boldsymbol{p_H}$
$\boldsymbol{p_{H_{\text{new}}}}$	Current value of $\boldsymbol{p_H}$
$\boldsymbol{p_{H_{\text{old}}}}$	Previous value of $\boldsymbol{p_H}$
p_i	Generalized momentum [kg m s^{-1}]
$\dot{p}_i$	Generalized force [kg m s^{-2}]
$\boldsymbol{p}_i$	Momentum vector of atom i [kg m s^{-1}]
p_r	Momentum in the r-direction [kg m s^{-1}]
p_r^*	Non-dimensionalized momentum in the r-direction [$*$]
$\dot{p}_r$	Force in the r-direction [kg m s^{-2}]
$\dot{p}_r^*$	Non-dimensionalized force in the r-direction [$*$]

Symbol	*Definition*
$p'^{*}_{u,i}$	Non-dimensionalized momentum in the MWC Hessian eigenspace [$*$]
p_x	Momentum in the x-direction [kg m s^{-1}]
p^{*}_{x}	Non-dimensionalized momentum in the x-direction [$*$]
p_{x_1}	Momentum in the x_1-direction [kg m s^{-1}]
$p^{*}_{x_1}$	Non-dimensionalized momentum in the x_1-direction [$*$]
p'_{x_1}	Mass-weighted momentum in the x_1-direction [kg$^{1/2}$ m s^{-1}]
$p'^{*}_{x_1}$	Non-dimensionalized value of p'_{x_1} [$*$]
p_{x_2}	Momentum in the x_2-direction [kg m s^{-1}]
$p^{*}_{x_2}$	Non-dimensionalized momentum in the x_2-direction [$*$]
p'_{x_2}	Mass-weighted momentum in the x_2-direction [kg$^{1/2}$ m s^{-1}]
$p'^{*}_{x_2}$	Non-dimensionalized value of p'_{x_2} [$*$]
$\dot{p}_x$	Force in the x-direction [kg m s^{-2}]
$\dot{p}^{*}_{x}$	Non-dimensionalized force in the x-direction [$*$]
$p_{x,i}$	x-component of $\boldsymbol{p}_i$ [kg m s^{-1}]
p_y	Momentum in the y-direction [kg m s^{-1}]
p^{*}_{y}	Non-dimensionalized momentum in the y-direction [$*$]
p_{y_1}	Momentum in the y_1-direction [kg m s^{-1}]
$p^{*}_{y_1}$	Non-dimensionalized momentum in the y_1-direction [$*$]
p'_{y_1}	Mass-weighted momentum in the y_1-direction [kg$^{1/2}$ m s^{-1}]
$p'^{*}_{y_1}$	Non-dimensionalized value of p'_{y_1} [$*$]
p_{y_2}	Momentum in the y_2-direction [kg m s^{-1}]

Symbol	*Definition*
$p^*_{y_2}$	Non-dimensionalized momentum in the y_2-direction [$*$]
p'_{y_2}	Mass-weighted momentum in the y_2-direction [kg$^{1/2}$ m s^{-1}]
$p'^*_{y_2}$	Non-dimensionalized value of p'_{y_2} [$*$]
$\dot{p}_y$	Force in the y-direction [kg m s^{-2}]
$\dot{p}^*_y$	Non-dimensionalized force in the y-direction [$*$]
$p_{y,i}$	y-component of $\boldsymbol{p}_i$ [kg m s^{-1}]
p_z	Momentum in the z-direction [kg m s^{-1}]
p^*_z	Non-dimensionalized momentum in the z-direction [$*$]
p_{z_1}	Momentum in the z_1-direction [kg m s^{-1}]
$p^*_{z_1}$	Non-dimensionalized momentum in the z_1-direction [$*$]
p'_{z_1}	Mass-weighted momentum in the z_1-direction [kg$^{1/2}$ m s^{-1}]
$p'^*_{z_1}$	Non-dimensionalized value of p'_{z_1} [$*$]
p_{z_2}	Momentum in the z_2-direction [kg m s^{-1}]
$p^*_{z_2}$	Non-dimensionalized momentum in the z_2-direction [$*$]
p'_{z_2}	Mass-weighted momentum in the z_2-direction [kg$^{1/2}$ m s^{-1}]
$p'^*_{z_2}$	Non-dimensionalized value of p'_{z_2} [$*$]
$\dot{p}_z$	Force in the z-direction [kg m s^{-2}]
$\dot{p}^*_z$	Non-dimensionalized force in the z-direction [$*$]
p_θ	Momentum in the θ-direction [kg m s^{-1}]
p^*_θ	Non-dimensionalized momentum in the θ-direction [$*$]
$\dot{p}_\theta$	Force in the θ-direction [kg m s^{-2}]

Symbol	*Definition*
$\dot{p}^*_\theta$	Non-dimensionalized force in the θ-direction [$*$]
p_ϕ	Momentum in the ϕ-direction [kg m s^{-1}]
p^*_ϕ	Non-dimensionalized momentum in the ϕ-direction [$*$]
$\dot{p}_\phi$	Force in the ϕ-direction [kg m s^{-2}]
$\dot{p}^*_\phi$	Non-dimensionalized force in the ϕ-direction [$*$]
P	Gas partial pressure [Pa]
$P(s_1, s_2)$	Least-squares fit for the three-body potential [eV]
$P(u \to u')$	Scattering kernel [$*$]
$P(v \to v')$	Scattering kernel [$*$]
$P(w \to w')$	Scattering kernel [$*$]
$\boldsymbol{q_0}$	Initial configuration vector in Cartesian coordinates [m]
$\boldsymbol{q^i_0}$	$\boldsymbol{q_0}$ at step i [m]
q_i	Generalized coordinate [m]
$\dot{q}_i$	Generalized velocity [m s^{-1}]
$\ddot{q}_i$	Generalized acceleration [m s^{-2}]
q_m	Factor in the MK adsorption model [$*$]
Q	Molecular property in question
	Total permeation rate [molecules s^{-1}]
$\mathbf{Q}$	Component of the step $\boldsymbol{\Delta q}$ along $\mathbf{U}$ [m]

Symbol	*Definition*
r	Intermolecular distance [Å] [m]
	Desorption rate [molecules s^{-1}]
	Detector radius [m]
r^*	Non-dimensionalized r-coordinate [$*$]
$\hat{\boldsymbol{r}}$	Unit vector in the r-direction [$*$]
$\dot{r}$	Time-rate-of-change of the r-coordinate [m s^{-1}]
$\dot{r}^*$	Non-dimensionalized time-rate-of-change of the r-coordinate [$*$]
r_0	Equilibrium intermolecular distance [Å],
	Fitting coefficient for the three-body potential [Å]
r_1	BR potential adjustable parameter [Å]
r_{3b}	Fitting coefficient for the three-body potential [Å]
r_c	Distance in geometric representation of CLL [$*$]
r_e	Fitting parameter for V_{att} [Å]
r_{HS}	Radius of the hypersphere [m]
r_i	Distance between gas molecule and i^{th} bulk molecule [Å]
r_i'	Adjusted value of r_i [Å]
$\boldsymbol{r}_i$	Radius vector of atom i [m]
r_{ref}	Reaction zone parameter [Å]
$r_{\text{ref},2}$	Reaction zone parameter [Å]
$r_{x,i}$	x-component of $\boldsymbol{r}_i$ [m]
$r_{y,i}$	y-component of $\boldsymbol{r}_i$ [m]

Symbol	*Definition*
R	Uniform random number between 0 and 1 [$*$]
	Distance from the detector to the surface [m]
$\mathcal{R}$	Radius parameter [Å]
R_1	Uniform random number between 0 and 1 [$*$]
R_2	Uniform random number between 0 and 1 [$*$]
R_3	Uniform random number between 0 and 1 [$*$]
R_4	Uniform random number between 0 and 1 [$*$]
R_c	Critical effective interaction radius [Å]
R_{eff}	Effective interaction radius [Å]
R_i	Uniform random number between 0 and 1 [$*$]
R_{sp}	Specific gas constant [J kg^{-1} K^{-1}]
S	Solubility [molecules m^{-3} Pa$^{-1/2}$]
s_1	Variable for the three-body potential [Å]
s_2	Variable for the three-body potential [Å]
S_0	Initial adsorption probability [$*$]
	Maximum solubility [molecules m^{-3} Pa$^{-1/2}$]
S_0^*	Adsorption probability onto the adlayer [$*$]
$S(\theta)$	Adsorption probability [$*$]
t	Time [s]
$\langle t \rangle$	Average time between events [s]
t^*	Non-dimensionalized time [$*$]

Symbol	*Definition*
t_{mp}	Most-probable travel time [s]
$\boldsymbol{T}$	Pseudo-tangent to the path
$\mathcal{T}$	Kinetic energy [J]
$\mathcal{T}^*$	Non-dimensionalized kinetic energy [$*$]
T_c	Critical temperature [K]
T_s	Surface temperature [K]
T_{tr}	Triple-point temperature [K]
u	A tangential velocity component [m s^{-1}]
u'	A post-collisional tangential velocity component [m s^{-1}]
$\bar{u}_j$	j^{th} Hessian eigenvector [$*$]
u_{mp}	Most-probable speed [m s^{-1}]
$\boldsymbol{u}$	Vector in calculating the BFGS algorithm [m J^{-1}]
$\mathbf{U}$	Unitary matrix that diagonalizes $\mathbf{H}$ [$*$]
v	A tangential velocity component [m s^{-1}]
$\boldsymbol{v}$	Velocity [m s^{-1}]
v'	A post-collisional tangential velocity component [m s^{-1}]
V	Potential energy [J]
V^*	Non-dimensionalized potential energy [$*$]
V_0	Potential energy at some initial configuration [J]
V_{0000}	6D expansion coefficient [eV Å]
V_{0010}	6D expansion coefficient [eV Å]

Symbol	*Definition*
V_{0011}	6D expansion coefficient [eV Å]
V_{00b}	2D expansion coefficient [eV]
V_{00h}	2D expansion coefficient [eV]
V_{00t}	2D expansion coefficient [eV]
V_2	Two-body potential [eV]
V_2^A	Two-body potential for H_2 as it desorbs [eV]
V_2^B	Two-body potential for two H atoms [eV]
V_{2000}	6D expansion coefficient [eV Å]
V_{2010}	6D expansion coefficient [eV Å]
V_{2011}	6D expansion coefficient [eV Å]
V_{2e10}	6D expansion coefficient [eV Å]
V_{20b}	2D expansion coefficient [eV]
V_{20h}	2D expansion coefficient [eV]
V_{20t}	2D expansion coefficient [eV]
V_{2eb}	2D expansion coefficient [eV]
V_3	Three-body potential [eV]
V_3^A	Three-body potential for H_2 as it desorbs [eV]
V_3^B	Three-body potential for two H atoms [eV]
V_{6D}	Wiesenekker 6D PES [eV]
V_{att}	Two-body attractive potential [eV]
V_{bh140}	2D PES [eV]

Symbol	*Definition*
V_{bh90}	2D PES [eV]
V_{bt90}	2D PES [eV]
V_{bt140}	2D PES [eV]
V_{BR}	BR potential [kJ mol^{-1}]
V_{hb90}	2D PES [eV]
V_{hb140}	2D PES [eV]
V_{LJ}	LJ potential [kJ mol^{-1}]
V_{M}	Morse potential [kJ mol^{-1}]
V_{rep}	Two-body repulsive potential [eV]
V_{tb90}	2D PES [eV]
V_{tb140}	2D PES [eV]
$V(z_g^{\mathrm{ave}})$	BR potential term [kJ mol^{-1}]
w	Normal velocity component [m s^{-1}]
w'	Post-collisional normal velocity component [m s^{-1}]
W	BR potential adjustable parameter [kJ mol^{-1}]
x	x-coordinate (parallel to the surface) [m]
	Reaction order for desorption [$*$]
x^*	Non-dimensionalized x-coordinate [$*$]
$\dot{x}$	Time-rate-of-change of the x-coordinate [m s^{-1}]
$\dot{x}^*$	Non-dimensionalized time-rate-of-change of the x-coordinate [$*$]
x_1	x-coordinate of atom 1 [m]

Symbol	*Definition*
$\dot{x}_1$	Time-rate-of-change of the x-coordinate of atom 1 [m s^{-1}]
x_2	x-coordinate of atom 2 [m]
$\dot{x}_2$	Time-rate-of-change of the x-coordinate of atom 2 [m s^{-1}]
x_g	A coordinate of the gas molecule [Å]
x_i	A coordinate of the surface molecule [Å]
	x-coordinate of atom i [m]
y	y-coordinate (parallel to the surface) [m]
y^*	Non-dimensionalized y-coordinate [$*$]
$\dot{y}$	Time-rate-of-change of the y-coordinate [m s^{-1}]
$\dot{y}^*$	Non-dimensionalized time-rate-of-change of the y-coordinate [$*$]
y_1	y-coordinate of atom 1 [m]
$\dot{y}_1$	Time-rate-of-change of the y-coordinate of atom 1 [m s^{-1}]
y_2	y-coordinate of atom 2 [m]
$\dot{y}_2$	Time-rate-of-change of the y-coordinate of atom 2 [m s^{-1}]
y_g	A coordinate of the gas molecule [Å]
y_i	A coordinate of the surface molecule [Å]
	y-coordinate of atom i [m]
$Y_2^e(\theta, \phi)$	Modified spherical harmonic [$*$]
$Y_l^m(\theta, \phi)$	Spherical harmonics of degree l and order m [$*$]
z	Height above the surface [Å] [m]
z^*	Non-dimensionalized z-coordinate [$*$]

Symbol	*Definition*
$\dot{z}$	Time-rate-of-change of the z-coordinate [m s^{-1}]
$\dot{z}^*$	Non-dimensionalized time-rate-of-change of the z-coordinate [$*$]
z_0	Fitting coefficient for the three-body potential [Å]
z_1	Height of atom 1 relative to the surface [Å] [m]
$\dot{z}_1$	Time-rate-of-change of the z-coordinate of atom 1 [m s^{-1}]
z_2	Height of atom 2 relative to the surface [Å] [m]
$\dot{z}_2$	Time-rate-of-change of the z-coordinate of atom 2 [m s^{-1}]
z_{3b}	Fitting coefficient for the three-body potential [Å]
z_e	Fitting parameter for V_{att} [Å]
z_g	A coordinate of the gas molecule [Å]
z_g^{ave}	Height above the "local-average" surface [Å]
z_{gs}^{ave}	Height of the "local-average" surface [Å]
z_i	A coordinate of the surface molecule [Å]
z_{ref}	Reaction zone parameter [Å]
$z_{\text{ref},2}$	Reaction zone parameter [Å]

Greek Symbol	*Definition*
α	BR potential adjustable parameter [$Å^{-1}$]
α_1	BR potential adjustable parameter [$Å^{-1}$]
	A Cartesian coordinate [m]
α_{1c}	α_1-coordinate of the center of the hypersphere [m]

Greek Symbol	*Definition*
α_j	A Cartesian coordinate [m]
α_{jc}	α_j-coordinate of the center of the hypersphere [m]
$\alpha_{j,i}$	α_j taken from $\boldsymbol{p_i}$ [m]
$\alpha_{j,i+1}$	α_j taken from $\boldsymbol{p_{i+1}}$ [m]
α_n	Accommodation coefficient, normal kinetic energy [$*$]
$\alpha_{n,\mathrm{ad}}$	Adlayer accommodation coefficient, normal kinetic energy [$*$]
α_t	Accommodation coefficient, tangential kinetic energy [$*$]
$\alpha_{t,\mathrm{ad}}$	Adlayer accommodation coefficient, tangential kinetic energy [$*$]
β_i	Generalized mass-weighted coordinate [m $\mathrm{kg}^{1/2}$]
$\ddot{\beta}_i$	Generalized mass-weighted acceleration [m s^{-2} $\mathrm{kg}^{1/2}$]
γ_1	Fitting coefficient for the three-body potential [$\mathrm{\AA}^{-1}$]
γ_2	Fitting coefficient for the three-body potential [$\mathrm{\AA}^{-1}$]
δ	BR potential adjustable parameter [$\mathrm{\AA}^{-2}$]
$\boldsymbol{\Delta q}$	Configuration perturbation vector in Cartesian coordinates [m]
$\boldsymbol{\Delta q_j}$	$\boldsymbol{\Delta q}$ with all elements zero except for the j^{th} element [m]
Δq_j	j^{th} element of $\boldsymbol{\Delta q}$ [m]
Δt	Desorption event time step [s]
ΔV	Change in V between adsorbed and TS configurations [J]
ΔV^*	Non-dimensionalized value of ΔV [$*$]
Δx	Difference between x_1 (x_2) and x [m]
	Step taken in evaluating a central difference derivative [m]

Greek Symbol	*Definition*
Δy	Difference between y_1 (y_2) and y [m]
Δz	Difference between z_1 (z_2) and z [m]
$\Delta\zeta$	Reaction zone parameter [radians]
$\Delta\theta$	Angular sweep of A_{cap} [radians]
$\Delta\xi$	Reaction zone parameter [radians]
ε_{LJ}	LJ well-depth parameter [kJ mol^{-1}]
ε_{M}	Morse well-depth parameter [kJ mol^{-1}]
ϵ_1	Threshold parameter [m]
ϵ_2	Threshold parameter [$*$]
ζ	Reaction zone parameter [radians]
ζ_0	Reaction zone parameter [radians]
η	Threshold parameter [radians]
θ	Adlayer coverage [ML],
	Elevation angle [radians]
	Angle between $\boldsymbol{G}$ and $\boldsymbol{T}$ [radians]
	Desorption angle, measured from the surface normal [radians]
θ^*	Non-dimensionalized θ-coordinate [radians]
$\hat{\boldsymbol{\theta}}$	Unit vector in the θ-direction [$*$]
$\dot{\theta}$	Time-rate-of-change of the θ-coordinate [radians s^{-1}]
$\dot{\theta}^*$	Non-dimensionalized value of $\dot{\theta}$ [radians]
θ_c	Angle in geometric representation of CLL [$*$]

Greek Symbol	*Definition*
θ_f	In-plane scattering angle with respect to surface normal [$^\circ$]
θ_i	Angle of incidence with respect to the surface normal [$^\circ$]
λ	Optimal step length [m]
$\boldsymbol{\lambda_0}$	Diagonal matrix of the eigenvalues of $\mathbf{H_0}$ [$*$]
μ	Reduced mass [kg]
ν	Molecular vibrational frequency [cycles s^{-1}]
	Frequency factor [molecules$^{-(x-1)}$ s^{-1}]
ξ	Reaction zone parameter [radians]
Ξ	Angle between the z-axis and $\mathcal{J}$ [radians]
ξ_0	Reaction zone parameter [radians]
ρ_{att}	Variable for V_{att} [Å]
ρ_{rep}	Variable for V_{rep} [Å]
σ_{LJ}	LJ zero-potential intermolecular distance [Å]
σ_{M}	Morse potential parameter [Å^{-1}]
σ_n	Accommodation coefficient, normal momentum [$*$]
σ_t	Accommodation coefficient, tangential momentum [$*$]
ϕ	Azimuthal angle [radians]
	Concentration of molecules [molecules m^{-3}]
ϕ^*	Non-dimensionalized ϕ-coordinate [radians]
$\hat{\boldsymbol{\phi}}$	Unit vector in the ϕ-direction [$*$]
$\dot{\phi}$	Time-rate-of-change of the ϕ-coordinate [radians s^{-1}]

Greek Symbol	*Definition*
$\dot{\phi}^*$	Non-dimensionalized value of $\dot{\phi}$ [radians]
Φ	Permeability [molecules m^{-1} s^{-1} $Pa^{-1/2}$]
Φ_0	Maximum permeability [molecules m^{-1} s^{-1} $Pa^{-1/2}$]
$\phi(r)$	BR potential weighting function [$*$]
Φ_i^Q	Incident flux of Q [cm^{-2} s^{-1}]
Φ_r^Q	Reflected flux of Q [cm^{-2} s^{-1}]
Φ_w^Q	Fully-accommodated reflected flux of Q [cm^{-2} s^{-1}]
χ	Reaction zone parameter [radians]
χ_2	Reaction zone parameter [radians]
Ω	Solid angle [steradians]

Appendix B. List of Acronyms

Acronym	*Definition*
1D	One-Dimensional
2D	Two-Dimensional
3D	Three-Dimensional
6D	Six-Dimensional
AFOSR	Air Force Office of Scientific Research
AFRL	Air Force Research Laboratory
BFGS	Broyden-Fletcher-Goldfarb-Shanno
BR	Barker-Rettner
CDF	Cumulative Distribution Function
CFD	Computational Fluid Dynamics
CLL	Cercignani-Lampis-Lord
CT	Classical Trajectory
DFT	Density Functional Theory
DIET	Desorption Induced by Electronic Transitions
DSMC	Direct Simulation Monte Carlo
EM	Electromagnetic
ER	Eley-Rideal
ESD	Electron-Stimulated Desorption
FCC	Face-Centered Cubic
FID	Field-Induced Desorption

Acronym	*Definition*
GGA	Generalized Gradient Approximation
GW	Gaussian Weighting
HPM	High-Power Microwave
ICEPIC	Improved Concurrent Electromagnetic Particle-In-Cell
IID	Ion-Induced Desorption
LEPS	London-Eyring-Polyani-Sato
LH	Langmuir-Hinshelwood
LJ	Lennard-Jones
MB	Maxwell-Boltzmann
MC	Monte Carlo
MD	Molecular Dynamics
MEMS	Micro-Electro-Mechanical Systems
MK	Modified Kisliuk
MKS	Modified Kisliuk with Scattering
ML	Monolayer
MS	Multi-Stage
MWC	Mass-Weighted Cartesian
PES	Potential Energy Surface
PID	Photo-Induced Desorption
QCT	Quasi-Classical Trajectory
RS	Rigid Surface

Acronym	*Definition*
SEE	Secondary Electron Emission
SWS	Slow Wave Structure
TPD	Temperature-Programmed Desorption
TS	Transition State
TST	Transition State Theory
TTPD	Threshold Temperature-Programmed Desorption
UHV	Ultra-High Vacuum
XHV	Extreme-High Vacuum
ZPE	Zero-Point Energy

Bibliography

1. Abbott, H. L. and I. Harrison. "Seven-dimensional microcanonical treatment of hydrogen dissociation dynamics on Cu(111): Clarifying the essential role of surface phonons," *J. Chem. Phys.*, 125: 024704 (July 2006).

2. Adhikari, S. and G. D. Billing. "Four-dimensional quantum and two-dimensional classical mechanical study of molecule-surface interactions," *J. Chem. Phys.*, 112: 3884–3889 (February 2000).

3. Anderson, J. B. "Statistical theories of chemical reactions. Distributions in the transition region," *J. Chem. Phys.*, 58: 4684–4692 (May 1973).

4. Andersson, S. and K. Svensson. "Electron-Induced Desorption of Physisorbed H_2 via Resonance Vibrational Excitation," *Phys. Rev. Lett.*, 102: 156104 (April 2009).

5. Anger, G., A. Winkler, and K. Rendulic. "Adsorption and desorption kinetics in the systems H_2/Cu(111), H_2/Cu(110) and H_2/Cu(100)," *Surf. Sci.*, 220: 1–17 (October 1989).

6. Antoniewicz, P. R. "Model for electron- and photon-stimulated desorption," *Phys. Rev. B*, 21: 3811–3815 (May 1980).

7. Antonsen, T. M., A. A. Mondelli, B. Levush, J. P. Verboncoeur, and C. K. Birdsall. "Advances in modeling and simulation of vacuum electronic devices," *Proc. IEEE*, 87: 804–839 (May 1999).

8. Arumainayagam, C. R. and R. J. Madix. "Molecular beam studies of gas-surface collision dynamics," *Prog. Surf. Sci.*, 38: 1–102 (1991).

9. Arumainayagam, C. R., R. J. Madix, M. C. McMaster, V. M. Suzawa, and J. C. Tully. "Trapping dynamics of Xenon on Pt(111)," *Surf. Sci.*, 226: 180–190 (February 1990).

10. Arumainayagam, C. R., J. A. Stinnett, M. C. McMaster, and R. J. Madix. "Adsorbate-assisted adsorption: Trapping dynamics of Xe on Pt(111) at nonzero coverages," *J. Chem. Phys.*, 95: 5437–5443 (October 1991).

11. Balooch, M., M. Cardillo, D. Miller, and R. Stickney. "Molecular beam study of the apparent activation barrier associated with adsorption and desorption of hydrogen on copper," *Surf. Sci.*, 46: 358–392 (December 1974).

12. Balooch, M. and R. Stickney. "Angular distributions of H_2 desorbed from the (100), (110), and (111) faces of copper crystals," *Surf. Sci.*, 44: 310–320 (August 1974).

13. Barker, J. A. and C. T. Rettner. "Accurate potential energy surface for Xe/Pt(111): A benchmark gas/surface interaction potential," *J. Chem. Phys.*, 97: 5844–5850 (October 1992).

14. Barker, J. A. and C. T. Rettner. "Erratum: Accurate potential energy surface for Xe/Pt(111): A benchmark gas/surface interaction potential [J. Chem. Phys. 97, 5844 (1992)]," *J. Chem. Phys.*, 101: 9202 (November 1994).

15. Bendow, B. and S.-C. Ying. "Phonon-Induced Desorption of Adatoms from Crystal Surfaces. I. Formal Theory," *Phys. Rev. B*, 7: 622 (January 1973).

16. Benford, J. and G. Benford. "Survey of pulse shortening in high-power microwave sources," *IEEE Trans. Plasma Sci.*, 25: 311–317 (April 1997).

17. Bengtsson, L., K. Svensson, M. Hassel, J. Bellman, M. Persson, and S. Andersson. "H_2 adsorbed in a two-dimensional quantum rotor state on a stepped copper surface," *Phys. Rev. B*, 61: 16921–16932 (June 2000).

18. Bennett, C. H. "Molecular Dynamics and Transition State Theory: The Simulation of Infrequent Events," in *Algorithms for Chemical Computations*. Ed. R. E. Christoffersen. Washington, D. C.: American Chemical Society, 1977.

19. Bergeron, H., N. Rougeau, V. Sidis, M. Sizun, D. Teillet-Billy, and F. Aguillon. "OH Formation from O and H Atoms Physisorbed on a Graphitic Surface through the Langmuir-Hinshelwood Mechanism: A Quasi-Classical Approach," *J. Phys. Chem. A*, 112: 11921–11930 (November 2008).

20. Bird, G. A. *Molecular Gas Dynamics and the Direct Simulation of Gas Flows*. New York: Oxford University Press, 1994.

21. Bitensky, I., E. Parilis, S. Della-Negra, and Y. Beyec. "Emission of hydrogen ions under multiply charged ion bombardment," *Nucl. Instrum. Methods Phys. Res., Sect. B*, 72: 380–386 (December 1992).

22. Bonfanti, M., C. Díaz, M. F. Somers, and G.-J. Kroes. "Hydrogen dissociation on Cu(111): the influence of lattice motion. Part I," *Phys. Chem. Chem. Phys.*, 13: 4552–4561 (February 2011).

23. Bonnet, L. and J.-C. Rayez. "Quasiclassical trajectory method for molecular scattering processes: necessity of a weighted binning approach," *Chem. Phys. Lett.*, 277: 183–190 (October 1997).

24. Bonnet, L. and J.-C. Rayez. "Gaussian weighting in the quasiclassical trajectory method," *Chem. Phys. Lett.*, 397: 106–109 (October 2004).

25. Bradley, T. and R. Stickney. "Spatial distributions of H_2 desorbed from Fe, Pt, Cu, Nb, and stainless steel surfaces," *Surf. Sci.*, 38: 313–326 (July 1973).

26. Braun, J., K. L. Kostov, G. Witte, and C. Wöll. "CO overlayers on Ru(0001) studied by helium atom scattering: Structure, dynamics, and the influence of coadsorbed H and O," *J. Chem. Phys.*, 106: 8262–8273 (May 1997).

27. Cacciatore, M. and M. Rutigliano. "Dynamics of plasma-surface processes: E-R and L-H atom recombination reactions," *Plasma Sources Sci. Technol.*, 18: 023002 (May 2009).

28. Caratzoulas, S., B. Jackson, and M. Persson. "Eley-Rideal and hot-atom reaction dynamics of H(g) with H adsorbed on Cu(111)," *J. Chem. Phys.*, 107: 6420–6431 (1997).

29. Cardillo, M., M. Balooch, and R. Stickney. "Detailed balancing and quasi-equilibrium in the adsorption of hydrogen on copper," *Surf. Sci.*, 50: 263–278 (June 1975).

30. Chen, C., Y. Huang, X. Ji, and Y. Xiao. "Efficiently finding the minimum free energy path from steepest descent path," *J. Chem. Phys.*, 138: 164122 (April 2013).

31. Chorkendorff, I. and P. Rasmussen. "Reconstruction of Cu(100) by adsorption of atomic hydrogen," *Surf. Sci.*, 248: 35–44 (May 1991).

32. Cilpa, G., J. Colin, F. Labat, C. Adamo, and G. Chambaud. "Adsorption of successive layers of H_2 molecules on a model copper surface: performances of second- to fifth-rung exchange-correlation functionals," *Theor. Chem. Acc.*, 131: 1–9 (2012).

33. Comsa, G. and R. David. "The purely "fast" distribution of H_2 and D_2 molecules desorbing from Cu(100) and Cu(111) surfaces," *Surf. Sci.*, 117: 77–84 (May 1982).

34. Dai, J. and J. C. Light. "Six dimensional quantum dynamics study for dissociative adsorption of H_2 on Cu(111) surface," *J. Chem. Phys.*, 107: 1676–1679 (August 1997).

35. Dewar, M. J., A. J. Holder, R. D. Dennington, D. A. Liotard, D. G. Truhlar, T. A. Keith, J. M. Millam, and C. D. Harris. *AMPAC 8 User Manual*. 2004.

36. Díaz, C., R. A. Olsen, D. J. Auerbach, and G. J. Kroes. "Six-dimensional dynamics study of reactive and non reactive scattering of H_2 from Cu(111) using a chemically accurate potential energy surface," *Phys. Chem. Chem. Phys.*, 12: 6499–6519 (June 2010).

37. Díaz, C., R. A. Olsen, H. F. Busnengo, and G. J. Kroes. "Dynamics on Six-Dimensional Potential Energy Surfaces for H_2/Cu(111): Corrugation Reducing Procedure versus Modified Shepard Interpolation Method and PW91 versus

RPBE," *J. Phys. Chem. C*, 114: 11192–11201 (July 2010).

38. Díaz, C., E. Pijper, R. A. Olsen, H. F. Busnengo, D. J. Auerbach, and G. J. Kroes. "Chemically Accurate Simulation of a Prototypical Surface Reaction: H_2 Dissociation on Cu(111)," *Science*, 326: 832–834 (November 2009).

39. Diño, W. A., H. Kasai, and A. Okiji. "Orientational effects in dissociative adsorption/associative desorption dynamics of $H_2(D_2)$ on Cu and Pd," *Prog. Surf. Sci.*, 63: 63–134 (February 2000).

40. Dong, C., P. Mehrotra, and G. R. Myneni. "Methods for Reducing Hydrogen Outgassing," *AIP Conf. Proc.*, 671: 307–312 (July 2003).

41. Drinkwine, M. J. and D. Lichtman. "Electron stimulated desorption: A critical review," *Prog. Surf. Sci.*, 8: 123–142 (1977).

42. Dylla, H. F. "A review of the wall problem and conditioning techniques for tokamaks," *J. Nucl. Mater.*, 93-94: 61–74 (October 1980).

43. Dylla, H. F., D. M. Manos, and P. H. LaMarche. "Correlation of outgassing of stainless steel and aluminum with various surface treatments," *J. Vac. Sci. Technol. A*, 11: 2623–2636 (1993).

44. Engdahl, C., B. I. Lundqvist, U. Nielsen, and J. K. Nørskov. "Multidimensional effects in dissociative chemisorption: H_2 on Cu and Ni surfaces," *Phys. Rev. B*, 45: 11362–11365 (May 1992).

45. Engdahl, C. and U. Nielsen. "Hydrogen dissociation on copper: Importance of dimensionality in calculations of the sticking coefficient," *J. Chem. Phys.*, 98: 4223–4233 (March 1993).

46. Fichthorn, K. A. and W. H. Weinberg. "Theoretical foundations of dynamical Monte Carlo simulations," *J. Chem. Phys.*, 95: 1090–1096 (July 1991).

47. Frankcombe, T. and S. Smith. "Numerical solution methods for large, difficult kinetic master equations," *Theor. Chem. Acc.*, 124: 303–317 (2009).

48. Frankcombe, T. J., M. A. Collins, and D. H. Zhang. "Modified Shepard interpolation of gas-surface potential energy surfaces with strict plane group symmetry and translational periodicity," *J. Chem. Phys.*, 137: 144701 (October 2012).

49. Frezzotti, A., S. V. Nedea, A. J. Markvoort, P. Spijker, and L. Gibelli. "Comparison of Molecular Dynamics and Kinetic Modeling of Gas-Surface Interaction," *AIP Conf. Proc.*, 1084: 635–640 (December 2008).

50. Gelten, R., R. van Santen, and A. Jansen. "Dynamic Monte Carlo simulations of oscillatory heterogeneous catalytic reactions," in *Molecular Dynamics: From*

Classical to Quantum Methods. Eds. P. B. Balbuena and J. M. Seminario. New York: Elsevier, 1999.

51. Genger, T., O. Hinrichsen, and M. Muhler. "The temperature-programmed desorption of hydrogen from copper surfaces," *Catal. Lett.*, 59: 137–141 (June 1999).

52. Goodman, F. O. "Thermal Accommodation Coefficients," 84: 1431–1445 (June 1980).

53. Goodman, F. O. and H. Y. Wachman. *Dynamics of Gas-Surface Scattering*. New York: Academic Press, 1976.

54. Gorman, J. and W. Nardella. "Hydrogen Permeation through Metals," *Vacuum*, 12: 19–24 (1962).

55. Grabke, H. J. and E. Riecke. "Absorption and Diffusion of Hydrogen in Steels," *Mater. Tehnol.*, 34: 331–342 (2000).

56. Gross, A., B. Hammer, M. Scheffler, and W. Brenig. "High-Dimensional Quantum Dynamics of Adsorption and Desorption of H_2 at Cu(111)," *Phys. Rev. Lett.*, 73: 3121–3124 (December 1994).

57. Habenschaden, E. and J. Kppers. "Evaluation of flash desorption spectra," *Surf. Sci.*, 138: L147–L150 (March 1984).

58. van Harrevelt, R. and U. Manthe. "Off-normal incidence dissociative sticking of H_2 on Cu(100) studied using six-dimensional quantum calculations," *J. Chem. Phys.*, 123: 124706 (September 2005).

59. Haworth, M. D. Researcher, Air Force Research Laboratory, Kirtland Air Force Base NM. Personal Correspondence. 21 June 2012.

60. Hodgson, A. "State resolved desorption measurements as a probe of surface reactions," *Prog. Surf. Sci.*, 63: 1–61 (January 2000).

61. Houle, F. and W. Hinsberg. "Stochastic simulations of temperature programmed desorption kinetics," *Surf. Sci.*, 338: 329–346 (September 1995).

62. Hudson, J. B. *Surface Science: An Introduction*. New York: John Wiley, 1998.

63. Ikeda, A., M. Matsumoto, S. Ogura, T. Okano, and K. Fukutani. "Knudsen layer formation in laser induced thermal desorption," *J. Chem. Phys.*, 138: 124705 (March 2013).

64. Jabri, Y. *The Mountain Pass Theorem: Variants, Generalizations and Some Applications*. New York: Cambridge University Press, September 2003.

65. Jackson, B. and S. Nave. "The dissociative chemisorption of methane on Ni(111): The effects of molecular vibration and lattice motion," *J. Chem. Phys.*, 138: 174705 (May 2013).

66. Jakob, P. "Fermi resonance distortion of the Ru-CO stretching mode of CO adsorbed on Ru(001)," *J. Chem. Phys.*, 108: 5035–5043 (March 1998).

67. Jansen, A. "Monte Carlo simulations of chemical reactions on a surface with time-dependent reaction-rate constants," *Comput. Phys. Commun.*, 86: 1–12 (April 1995).

68. Jansen, A. and J. Lukkien. "Dynamic Monte-Carlo simulations of reactions in heterogeneous catalysis," *Catal. Today*, 53: 259–271 (October 1999).

69. Juaristi, J. I., M. Alducin, R. D. Muio, H. F. Busnengo, and A. Salin. "Role of Electron-Hole Pair Excitations in the Dissociative Adsorption of Diatomic Molecules on Metal Surfaces," *Phys. Rev. Lett.*, 100: 116102 (March 2008).

70. Juaristi, J. I., M. Alducin, R. D. Muio, H. F. Busnengo, and A. Salin. "Juaristi et al. Reply: Role of Electron-Hole Pair Excitations in the Dissociative Adsorption of Diatomic Molecules," *Phys. Rev. Lett.*, 102: 109602 (March 2009).

71. Kammler, T. and J. Küppers. "Interaction of H atoms with Cu(111) surfaces: Adsorption, absorption, and abstraction," *J. Chem. Phys.*, 111: 8115–8123 (November 1999).

72. Keck, J. "Statistical investigation of dissociation cross-sections for diatoms," *Discuss. Faraday Soc.*, 33: 173–182 (January 1962).

73. Keck, J. C. "Variational Theory of Chemical Reaction Rates Applied to Three-Body Recombinations," *J. Chem. Phys.*, 32: 1035–1050 (April 1960).

74. Kern, K. "Symmetry and rotational epitaxy of incommensurate Xe layers on Pt(111)," *Phys. Rev. B*, 35: 8265–8268 (May 1987).

75. Kern, K. and G. Comsa. "Modulated Structures of Adsorbed Rare Gas Monolayers," in *Phase Transitions in Surface Films 2*. Eds. H. Taub, G. Torzo, H. J. Lauter, and S. C. Fain. New York: Springer, 1991.

76. Kim, J. and G. O. Sitz. "The sticking of H_2(v=1, J=1) on Cu(100) measured using laser-induced thermal desorption," *Mol. Phys.*, 108: 1027–1032 (2010).

77. King, D. A. "Thermal desorption from metal surfaces: A review," *Surf. Sci.*, 47: 384–402 (January 1975).

78. Kolasinski, K. W. *Surface Science: Foundations of Catalysis and Nanoscience*. Wiltshire, United Kingdom: John Wiley & Sons, 2008.

79. Kreuzer, H. "Theory of surface processes," *Surf. Sci.*, 231: 213–226 (May 1990).

80. Kreuzer, H. J. "Diffusion, adsorption and desorption at surfaces," *J. Chem. Soc., Faraday Trans.*, 86: 1299–1305 (January 1990).

81. Kreuzer, H. J. "Kinetic lattice-gas model: Time-dependent generalization of the grand-canonical ensemble," *Phys. Rev. B*, 44: 1232–1239 (July 1991).

82. Kreuzer, H. J. "Thermal desorption kinetics," *Langmuir*, 8: 774–781 (1992).

83. Kroes, G. J., E. J. Baerends, and R. C. Mowrey. "Six-Dimensional Quantum Dynamics of Dissociative Chemisorption of (v=0, j=0) H_2 on Cu(100)," *Phys. Rev. Lett.*, 78: 3583–3586 (May 1997).

84. Kroes, G. J., E. J. Baerends, and R. C. Mowrey. "Erratum: Six-Dimensional Quantum Dynamics of Dissociative Chemisorption of (v=0, j=0) H_2 on Cu(100) [Phys. Rev. Lett. 78, 3583 (1997)]," *Phys. Rev. Lett.*, 81: 4781–4781 (November 1998).

85. Kroes, G. J., E. Pijper, and A. Salin. "Dissociative chemisorption of H_2 on the Cu(110) surface: A quantum and quasiclassical dynamical study," *J. Chem. Phys.*, 127: 164722–164722–12 (October 2007).

86. Kroes, G. J., J. G. Snijders, and R. C. Mowrey. "Performance of a fully closecoupled wave packet method for the H_2+LiF(001) model problem," *J. Chem. Phys.*, 102: 5512–5524 (April 1995).

87. Kubiak, G. D., G. O. Sitz, and R. N. Zare. "Recombinative desorption dynamics: Molecular hydrogen from Cu(110) and Cu(111)," *J. Chem. Phys.*, 83: 2538–2551 (1985).

88. Küchenhoff, S., W. Brenig, and Y. Chiba. "Vibrationally assisted sticking, tunneling and isotope effect for hydrogen on Cu surfaces," *Surf. Sci.*, 245: 389–400 (April 1991).

89. Larrégaray, P., L. Bonnet, and J. C. Rayez. "On product state distributions in triatomic unimolecular reactions: Beyond phase space theory and the adiabatic assumption," *J. Chem. Phys.*, 114: 3349–3364 (February 2001).

90. Laurent, G., C. Díaz, H. F. Busnengo, and F. Martn. "Nonmonotonic dissociative adsorption of vibrationally excited H_2 on metal surfaces," *Phys. Rev. B*, 81: 161404 (April 2010).

91. Lehner, B., M. Hohage, and P. Zeppenfeld. "Kinetic Monte Carlo simulation scheme for studying desorption processes," *Surf. Sci.*, 454-456: 251–255 (May 2000).

92. Lehner, B., M. Hohage, and P. Zeppenfeld. "Novel Monte Carlo scheme for the simulation of adsorption and desorption processes," *Chem. Phys. Lett.*, 336: 123–128 (March 2001).

93. Lehner, B., M. Hohage, and P. Zeppenfeld. "Kinetic Monte Carlo investigation of Xe adsorption and desorption on Pt(111) and Pt(997)," *Phys. Rev. B*, 65: 165407 (April 2002).

94. Liotard, D. and J.-P. Penot. "Critical Paths and Passes: Application to Quantum Chemistry," in *Numerical Methods in the Study of Critical Phenomena: Proceedings of a Colloquium, Carry-le-Rouet, France, June 2-4, 1980*. Eds. J. D. Dora, J. Demongeot, and B. Lacolle. New York: Springer-Verlag, 1981.

95. Liotard, D. A. "Algorithmic tools in the study of semiempirical potential surfaces," *Int. J. Quant. Chem.*, 44: 723–741 (November 1992).

96. Liou, W. and Y. Fang. *Microfluid Mechanics: Principles and Modeling*. New York: McGraw-Hill, 2006.

97. Lord, R. G. "Application of the Cercignani-Lampis Scattering Kernel to Direct Simulation Monte Carlo Calculations," *Proceedings of the 17th International Symposium on Rarefied Gas Dynamics*. 1427–1433. Germany: VCH Publishers, July 1990.

98. Lord, R. G. "Some extensions to the Cercignani-Lampis gas-surface scattering kernel," *Phys. Fluids*, 3: 706–710 (April 1991).

99. Lord, R. G. "Some further extensions of the Cercignani-Lampis gas-surface interaction model," *Phys. Fluids*, 7: 1159–1161 (May 1995).

100. Lukkien, J. J., J. P. L. Segers, P. A. J. Hilbers, R. J. Gelten, and A. P. J. Jansen. "Efficient Monte Carlo methods for the simulation of catalytic surface reactions," *Phys. Rev. E*, 58: 2598–2610 (August 1998).

101. Luntz, A. C., M. Persson, and G. O. Sitz. "Theoretical evidence for nonadiabatic vibrational deexcitation in $H_2(D_2)$ state-to-state scattering from Cu(100)," *J. Chem. Phys.*, 124: 091101 (March 2006).

102. Luo, M., D. MacLaren, I. Shuttleworth, and W. Allison. "Preferential subsurface occupation of atomic hydrogen on Cu(111)," *Chem. Phys. Lett.*, 381: 654–659 (November 2003).

103. MacLean, M., J. Marschall, and D. Driver. "Finite-Rate Surface Chemistry Model, II: Coupling to Viscous Navier-Stokes Code," *42nd AIAA Thermophysics Conference*. American Institute of Aeronautics and Astronautics, June 2011.

104. Manzi, S. J., R. E. Belardinelli, G. Costanza, and V. D. Pereyra. "Additional

constraints in adsorption-desorption kinetics," *Phys. Rev. E*, 79: 021103 (February 2009).

105. Marschall, J. and M. MacLean. "Finite-Rate Surface Chemistry Model, I: Formulation and Reaction System Examples," in *42nd AIAA Thermophysics Conference*. Ed., American Institute of Aeronautics and Astronautics, June 2011.

106. Masel, R. *Principles of adsorption and reaction on solid surfaces*. New York: John Wiley, 1996.

107. Matsushima, T. and K. Shobatake. "Surface reaction dynamics and energy partitioning," *J. Mol. Catal. A: Chem.*, 315: 135–147 (January 2010).

108. McCormack, D. A. and G.-J. Kroes. "Accuracy of trajectory methods for activated adsorption of H_2 on Cu(100)," *Chem. Phys. Lett.*, 296: 515–520 (November 1998).

109. McCreery, J. H. and G. Wolken. "A model potential for chemisorption: H_2+W(001)," *J. Chem. Phys.*, 63: 2340–2349 (September 1975).

110. McEwen, J.-S., S. Payne, H. Kreuzer, M. Kinne, R. Denecke, and H.-P. Steinrück. "Adsorption and desorption of CO on Pt(111): a comprehensive analysis," *Surf. Sci.*, 545: 47–69 (November 2003).

111. Mehta, D., J. D. Hauenstein, and D. J. Wales. "Communication: Certifying the potential energy landscape," *J. Chem. Phys.*, 138: 171101 (May 2013).

112. Menzel, D. "Desorption Phenomena," in *Interactions on Metal Surfaces*. Ed. R. Gomer. New York: Springer-Verlag, 1975.

113. Menzel, D. "Thirty years of MGR: How it came about, and what came of it," *Nucl. Instrum. Methods Phys. Res., Sect. B*, 101: 1–10 (June 1995).

114. Michelsen, H. A. and D. J. Auerbach. "A critical examination of data on the dissociative adsorption and associative desorption of hydrogen at copper surfaces," *J. Chem. Phys.*, 94: 7502–7520 (June 1991).

115. Michelsen, H. A., C. T. Rettner, and D. J. Auerbach. "State-specific dynamics of D_2 desorption from Cu(111): The role of molecular rotational motion in activated adsorption-desorption dynamics," *Phys. Rev. Lett.*, 69: 2678–2681 (November 1992).

116. Michelsen, H. A., C. T. Rettner, D. J. Auerbach, and R. N. Zare. "Effect of rotation on the translational and vibrational energy dependence of the dissociative adsorption of D_2 on Cu(111)," *J. Chem. Phys.*, 98: 8294–8307 (May 1993).

117. Miller, J. B., H. R. Siddiqui, S. M. Gates, J. N. Russell, J. T. Yates, J. C.

Tully, and M. J. Cardillo. "Extraction of kinetic parameters in temperature programmed desorption: A comparison of methods," *J. Chem. Phys.*, 87: 6725–6732 (December 1987).

118. Mills, G., H. Jnsson, and G. K. Schenter. "Reversible work transition state theory: application to dissociative adsorption of hydrogen," *Surf. Sci.*, 324: 305–337 (February 1995).

119. Monnai, T. "Microscopic reversibility and heat for thermostatted systems," *Phys. Rev. E*, 87: 042107 (April 2013).

120. Murphy, M. J. and A. Hodgson. "Adsorption and desorption dynamics of H_2 and D_2 on Cu(111): The role of surface temperature and evidence for corrugation of the dissociation barrier," *J. Chem. Phys.*, 108: 4199–4211 (March 1998).

121. Muzas, A. S., J. I. Juaristi, M. Alducin, R. D. Muiño, G. J. Kroes, and C. Díaz. "Vibrational deexcitation and rotational excitation of H_2 and D_2 scattered from Cu(111): Adiabatic versus non-adiabatic dynamics," *J. Chem. Phys.*, 137: 064707 (August 2012).

122. Nattino, F., C. Díaz, B. Jackson, and G.-J. Kroes. "Effect of Surface Motion on the Rotational Quadrupole Alignment Parameter of D_2 Reacting on Cu(111)," *Phys. Rev. Lett.*, 108: 236104 (June 2012).

123. Nave, S., D. Lemoine, M. F. Somers, S. M. Kingma, and G.-J. Kroes. "Six-dimensional quantum dynamics of (v=0, j=0)D_2 and of (v=1, j=0)H_2 scattering from Cu(111)," *J. Chem. Phys.*, 122: 214709 (June 2005).

124. Nie, J. L., H. Y. Xiao, and X. T. Zu. "First-principles study of H adsorption on and absorption in Cu(111) surface," *Chem. Phys.*, 321: 48–54 (January 2006).

125. Nieminen, R. and A. Jansen. "Monte Carlo simulations of surface reactions," *Appl. Catal., A*, 160: 99–123 (October 1997).

126. Olsen, R. A., H. F. Busnengo, A. Salin, M. F. Somers, G. J. Kroes, and E. J. Baerends. "Constructing accurate potential energy surfaces for a diatomic molecule interacting with a solid surface: H_2+Pt(111) and H_2+Cu(100)," *J. Chem. Phys.*, 116: 3841–3855 (March 2002).

127. Padilla, J. and I. Boyd. "Assessment of Gas-Surface Interaction Models in DSMC Analysis of Rarefied Hypersonic Flow," *39th AIAA Thermophysics Conference*. Miami: AIAA, June 2007.

128. Payne, S. and H. Kreuzer. "Multilayer adsorption and desorption," *Surf. Sci.*, 338: 261–278 (September 1995).

129. Payne, S., J.-S. McEwen, H. Kreuzer, and D. Menzel. "Adsorption and desorp-

tion of CO on Ru(0001): A comprehensive analysis," *Surf. Sci.*, 594: 240–262 (December 2005).

130. Perkins, W. G. "Permeation and Outgassing of Vacuum Materials," *J. Vac. Sci. Technol.*, 10: 543–556 (July 1973).

131. Perrier, A., L. Bonnet, and J.-C. Rayez. "Dynamical Study of H_2 and D_2 Desorbing from a Cu(111) Surface," *J. Phys. Chem. A*, 110: 1608–1617 (February 2006).

132. Perrier, A., L. Bonnet, and J.-C. Rayez. "Statisticodynamical approach of final state distributions in associative desorptions," *J. Chem. Phys.*, 124: 194701 (May 2006).

133. Persson, M., J. Strömquist, L. Bengtsson, B. Jackson, D. V. Shalashilin, and B. Hammer. "A first-principles potential energy surface for Eley-Rideal reaction dynamics of H atoms on Cu(111)," *J. Chem. Phys.*, 110: 2240–2249 (January 1999).

134. Poelsema, B., L. K. Verheij, and G. Comsa. "Adsorption, 2D phase transition and commensurate 2D phase of Xe on Pt(111)," 152/153: 851–858 (April 1985).

135. Powell, M. "A FORTRAN Subroutine for Solving Systems of Nonlinear Algebraic Equations," in *Numerical Methods for Nonlinear Algebraic Equations*. Ed. P. Rabinowitz. New York: Gordon and Breach Science Publishers, 1970.

136. Press, W. H., S. A. Teukolsky, W. T. Vetterling, and B. P. Flannery. *Numerical Recipes: The Art of Scientific Computing*. New York: Cambridge University Press, September 2007.

137. Quintas-Sánchez, E., C. Crespos, P. Larrégaray, J.-C. Rayez, L. Martin-Gondre, and J. Rubayo-Soneira. "Surface temperature effects on the dynamics of N2 Eley-Rideal recombination on W(100)," *J. Chem. Phys.*, 138: 024706 (January 2013).

138. Rasmussen, P., P. Holmblad, H. Christoffersen, P. Taylor, and I. Chorkendorff. "Dissociative adsorption of hydrogen on Cu(100) at low temperatures," *Surf. Sci.*, 287-288, Part 1: 79–83 (May 1993).

139. Rayez, J.-C., L. Bonnet, P. Larrégaray, and A. Perrier. "Transition State Theory: A Reaction Dynamics Tool Applied to Gas-Surface Reactions," *Mol. Sci.*, 3: A0029 (2009).

140. Redhead, P. "The first 50 years of electron stimulated desorption (1918-1968)," *Vacuum*, 48: 585–596 (June 1997).

141. Redhead, P. A. "Hydrogen in Vacuum Systems: An Overview," *AIP Conf.*

Proc., 671: 243–254 (July 2003).

142. Ren, W. and E. Vanden-Eijnden. "A climbing string method for saddle point search," *J. Chem. Phys.*, 138: 134105 (April 2013).

143. Rettner, C. T., L. A. DeLouise, and D. J. Auerbach. "Effect of incidence kinetic energy and surface coverage on the dissociative chemisorption of oxygen on W(110)," *J. Chem. Phys.*, 85: 1131–1149 (July 1986).

144. Rettner, C. T., H. A. Michelsen, and D. J. Auerbach. "Dynamics of the desorption of D_2 and H_2 from Cu(111)," *J. Vac. Sci. Technol. A*, 11: 1901–1906 (July 1993).

145. Rettner, C. T., H. A. Michelsen, and D. J. Auerbach. "Quantum-state-specific dynamics of the dissociative adsorption and associative desorption of H_2 at a Cu(111) surface," *J. Chem. Phys.*, 102: 4625–4641 (March 1995).

146. Rettner, C. T., H. A. Michelsen, D. J. Auerbach, and C. B. Mullins. "Dynamics of recombinative desorption: Angular distributions of H_2, HD, and D_2 desorbing from Cu(111)," *J. Chem. Phys.*, 94: 7499–7501 (June 1991).

147. Rettner, C. T., E. K. Schweizer, and H. Stein. "Dynamics of the chemisorption of N_2 on W(100): Precursor-mediated and activated dissociation," *J. Chem. Phys.*, 93: 1442–1454 (July 1990).

148. Rettner, C. T., H. Stein, and E. K. Schweizer. "Effect of collision energy and incidence angle on the precursor-mediated dissociative chemisorption of N_2 on W(100)," 89: 3337–3341 (September 1988).

149. Sahoo, T., S. Mukherjee, and S. Adhikari. "Surface temperature effect on the scattering of D_2(v=0, j=0)-Cu(111) system," *J. Chem. Phys.*, 136: 084306 (February 2012).

150. Sahoo, T., S. Sardar, and S. Adhikari. "The effect of phonon modes on the D_2(v=0, j=0)Cu(111) scattering processes," *Phys. Scripta*, 84: 028105 (August 2011).

151. Sahoo, T., S. Sardar, and S. Adhikari. "The effect of phonon modes on the H_2(v, j)/D_2(v, j)Cu(1nn) scattering processes," *Phys. Chem. Chem. Phys.*, 13: 10100–10110 (May 2011).

152. Salin, A. "Theoretical study of hydrogen dissociative adsorption on the Cu(110) surface," *J. Chem. Phys.*, 124: 104704 (March 2006).

153. San Marchi, C. and B. P. Somerday. *Technical Reference for Hydrogen Compatibility of Materials*. Sandia Report $SAND_2$012-7321, Sandia National Laboratories, September 2012.

154. Sato, S. "On a New Method of Drawing the Potential Energy Surface," *J. Chem. Phys.*, 23: 592–593 (March 1955).

155. Schaefer, C. and A. P. J. Jansen. "Coupling of kinetic Monte Carlo simulations of surface reactions to transport in a fluid for heterogeneous catalytic reactor modeling," *J. Chem. Phys.*, 138: 054102 (February 2013).

156. Schneider, R. "Plasmawall interaction: a multiscale problem," *Phys. Scr.*, T124: 76–79 (May 2006).

157. Schröter, L., C. Trame, J. Gauer, H. Zacharias, R. David, and W. Brenig. "State-selective studies of the associative desorption of hydrogen from Pd(100) and Cu(100)," *Farad. Discuss.*, 96: 55–65 (January 1993).

158. Sementa, L., M. Wijzenbroek, B. J. van Kolck, M. F. Somers, A. Al-Halabi, H. F. Busnengo, R. A. Olsen, G. J. Kroes, M. Rutkowski, C. Thewes, N. F. Kleimeier, and H. Zacharias. "Reactive scattering of H_2 from Cu(100): Comparison of dynamics calculations based on the specific reaction parameter approach to density functional theory with experiment," *J. Chem. Phys.*, 138: 044708 (January 2013).

159. Sheng, J. and J. Z. H. Zhang. "Quantum dynamics studies of adsorption and desorption of hydrogen at a Cu(111) surface," *J. Chem. Phys.*, 99: 1373–1381 (1993).

160. Simons, J. *An Introduction to Theoretical Chemistry.* Cambridge University Press, April 2003.

161. Somers, M., S. Kingma, E. Pijper, G. Kroes, and D. Lemoine. "Six-dimensional quantum dynamics of scattering of (v=0, j=0) H_2 and D_2 from Cu(111): test of two LEPS potential energy surfaces," *Chem. Phys. Lett.*, 360: 390–399 (July 2002).

162. Somers, M. F., R. A. Olsen, H. F. Busnengo, E. J. Baerends, and G. J. Kroes. "Reactive scattering of H_2 from Cu(100): Six-dimensional quantum dynamics results for reaction and scattering obtained with a new, accurately fitted potential-energy surface," *J. Chem. Phys.*, 121: 11379–11387 (December 2004).

163. Sorensen, C., P. Valentini, and T. E. Schwartzentruber. "Uncertainty Analysis of Reaction Rates in a Finite-Rate Surface-Catalysis Model," *J. Thermophys Heat Transfer*, 26: 407–416 (July 2012).

164. Spiegel, M. R. *Schaum's Outline of Theory and Problems of Theoretical Mechanics: With an Introduction to Lagrange's Equations and Hamiltonian Theory.* New York: McGraw-Hill, 1967.

165. Stotler, D. P. "Towards a revised Monte Carlo neutral particle surface interaction

model," *Phys. Scr.*, T124: 23–26 (May 2006).

166. Tabatabaei, J., B. Sakakini, M. Watson, and K. Waugh. "The detailed kinetics of the desorption of hydrogen from polycrystalline copper catalysts," *Catal. Lett.*, 59: 143–149 (June 1999).

167. Vach, H. and M. Châtelet. "Classical versus quantum mechanical desorption kinetics in molecule/surface scattering: The NO/diamond case," *J. Chem. Phys.*, 98: 8271–8276 (May 1993).

168. Vietzke, E. "Surface Effects on Hydrogen Release in the Plasma Edge," *Contrib. Plasma Phys.*, 42: 590–595 (November 2002).

169. Watts, E. and G. O. Sitz. "State-to-state scattering in a reactive system: H_2(v=1, J=1) from Cu(100)," *J. Chem. Phys.*, 114: 4171–4179 (March 2001).

170. Watts, E., G. O. Sitz, D. A. McCormack, G. J. Kroes, R. A. Olsen, J. A. Groeneveld, J. N. P. Van Stralen, E. J. Baerends, and R. C. Mowrey. "Rovibrationally inelastic scattering of (v=1,j=1) H_2 from Cu(100): Experiment and theory," *J. Chem. Phys.*, 114: 495–503 (January 2001).

171. Waugh, K. "The absorption and locking-in of hydrogen in copper," *Solid State Ionics*, 168: 327–342 (March 2004).

172. Weaver, J. F., J. A. Stinnett, and R. J. Madix. "Molecular dynamics simulations for xenon adsorption on Pt(111): dynamical differences in the effects produced by the Barker-Rettner and Morse potentials," *Surf. Sci.*, 391: 150–160 (November 1997).

173. Widdra, W., P. Trischberger, W. Friess, D. Menzel, S. H. Payne, and H. J. Kreuzer. "Rare-gas thermal desorption from flat and stepped platinum surfaces: Lateral interactions and the influence of dimensionality," *Phys. Rev. B*, 57: 4111–4126 (February 1998).

174. Wiesenekker, G., G. J. Kroes, and E. J. Baerends. "An analytical six-dimensional potential energy surface for dissociation of molecular hydrogen on Cu(100)," *J. Chem. Phys.*, 104: 7344–7358 (May 1996).

175. Wiesenekker, G., G. J. Kroes, E. J. Baerends, and R. C. Mowrey. "Dissociation of H_2 on Cu(100): Dynamics on a new two-dimensional potential energy surface," *J. Chem. Phys.*, 102: 3873–3883 (March 1995).

176. Wiesenekker, G., G. J. Kroes, E. J. Baerends, and R. C. Mowrey. "Erratum: Dissociation of H_2 on Cu(100): Dynamics on a new two-dimensional potential energy surface [J. Chem. Phys. 102, 3873 (1995)]," *J. Chem. Phys.*, 103: 5168–5169 (September 1995).

177. Wijzenbroek, M. and M. F. Somers. "Static surface temperature effects on the dissociation of H_2 and D_2 on Cu(111)," *J. Chem. Phys.*, 137: 054703 (August 2012).

178. Wu, K. J. and S. D. Kevan. "Isothermal measurements of NH_3 and ND_3 desorption from Cu(001)," *J. Chem. Phys.*, 94: 7494–7498 (June 1991).

179. Yamamoto, K., H. Takeuchi, and T. Hyakutake. "Scattering properties and scattering kernel based on the molecular dynamics analysis of gas-wall interaction," *Phys. Fluids*, 19: 087102 (August 2007).

180. Yamanishi, N., Y. Matsumoto, and K. Shobatake. "Multistage gas-surface interaction model for the direct simulation Monte Carlo method," *Phys. Fluids*, 11: 3540–3552 (November 1999).

181. Załuska-Kotur, M. A. "The kinetic Potts model in the description of surface dynamics," *Surf. Sci.*, 265: 196–208 (April 1992).

182. Zare, R. N. *Angular Momentum: Understanding Spatial Aspects in Chemistry and Physics*. New York: Wiley, July 1988.

183. Zhdanov, V. and B. Kasemo. "Simulation of oxygen desorption from Pt(111)," *Surf. Sci.*, 415: 403–410 (October 1998).

REPORT DOCUMENTATION PAGE

Form Approved
OMB No. 0704-0188

PLEASE DO NOT RETURN YOUR FORM TO THE ABOVE ADDRESS.

1. REPORT DATE *(DD-MM-YYYY)*	2. REPORT TYPE	3. DATES COVERED *(From - To)*
15-09-2013	Dissertation	Sep 2010 - Sep 2013

4. TITLE AND SUBTITLE

Scattering, Adsorption, and Langmuir-Hinshelwood Desorption Models for Physisorptive and Chemisorptive Gas-Surface Systems

5a. CONTRACT NUMBER

5b. GRANT NUMBER

5c. PROGRAM ELEMENT NUMBER

6. AUTHOR(S)

Bentley, Brook I., Captain, USAF

5d. PROJECT NUMBER

5e. TASK NUMBER

5f. WORK UNIT NUMBER

7. PERFORMING ORGANIZATION NAME(S) AND ADDRESS(ES)

Air Force Institute of Technology
Graduate School of Engineering and Management (AFIT/EN)
2950 Hobson Way
Wright-Patterson AFB OH 45433-7765

8. PERFORMING ORGANIZATION REPORT NUMBER

AFIT-ENY-DS-13-S-01

9. SPONSORING/MONITORING AGENCY NAME(S) AND ADDRESS(ES)

Air Force Research Laboratory, Directed Energy Directorate, HPM Division
Dr. Nathaniel Lockwood
3550 Aberdeen Ave SE, Building 909 Room 216
Kirtland AFB, NM 87117
Nathaniel.Lockwood@Kirtland.af.mil

10. SPONSOR/MONITOR'S ACRONYM(S)

AFRL/RDHEC

11. SPONSOR/MONITOR'S REPORT NUMBER(S)

12. DISTRIBUTION/AVAILABILITY STATEMENT

Distribution A. Approved for Public Release; Distribution Unlimited

13. SUPPLEMENTARY NOTES

14. ABSTRACT

Surface effects limit the performance of hypersonic vehicles, micro-electro-mechanical devices, and directed energy systems. This research develops methods to predict adsorption, scattering, and thermal desorption of molecules on a surface. These methods apply to physisorptive (adsorption and scattering) and chemisorptive (thermal desorption) gas-surface systems, and are developed under the Direct Simulation Monte Carlo construct. The novel adsorption and scattering contribution, the Modified Kisliuk with Scattering method, predicts angular and energy distributions, and adsorption probabilities. These results agree more closely with experiment than the state-of-the-art Cercignani-Lampis-Lord scattering kernel. Super-elastic scattering is predicted. Gas-adlayer interactions are included for the first time. The new thermal desorption model accurately predicts angular and energy distributions. The equations of motion are non-dimensionalized. Accurate timing is included. Initial conditions are chosen from a new truncated Maxwell-Boltzmann distribution. The absorption energy barrier is shown to significantly contribute only to translational energy.

15. SUBJECT TERMS

Hypersonics, Direct Simulation Monte Carlo, DSMC, Surface Effects, Desorption, Adsorption, Scattering, Rarefied Flow, High-Power Microwaves, Microflow, MEMS

16. SECURITY CLASSIFICATION OF:			17. LIMITATION OF ABSTRACT	18. NUMBER OF PAGES	19a. NAME OF RESPONSIBLE PERSON
a. REPORT	b. ABSTRACT	c. THIS PAGE			Dr. Robert B. Greendyke, AFIT/ENY
U	U	U	UU	168	19b. TELEPHONE NUMBER *(Include area code)* (937) 255-3636 x4567 Robert.Greendyke@afit.edu